Validation of a wind tunnel testing facility for blade surface pressure measurements

Fuglsang, Peter; Antoniou, Ioannis; Sørensen, Niels N.; Aagaard Madsen , Helge

Publication date:
1998

Document Version
Publisher's PDF, also known as Version of record

Risø-R-981(EN)

Validation of a Wind Tunnel Testing Facility for Blade Surface Pressure Measurements

Peter Fuglsang, Ioannis Antoniou, Niels N. Sørensen, Helge Aa. Madsen

Risø National Laboratory, Roskilde
April 1998

Abstract
This report concerns development and validation of a 2d testing facility for airfoil pressure measurements. The VELUX open jet wind tunnel was used with a test stand inserted. Reynolds Numbers until 1.3 million were achieved with an airfoil chord of 0.45 m. The aerodynamic load coefficients were found from pressure distribution measurements and the total drag coefficient was calculated from wake rake measurements. Stationary inflow as well as dynamic inflow through pitching motion was possible. Wind tunnel corrections were applied for streamline curvature and down-wash. Even though the wind tunnel is not ideal for 2d testing, the overall quality of the flow was acceptable with a uniform flow field at the test stand position and a turbulence intensity of 1% at the inlet of the test section. Reference values for free stream static and total pressure were found upstream of the test stand. The NACA 63-215 airfoil was tested and the results were compared with measurements from FFA and NACA. The measurements agreed well except for lift coefficient values at high angles of attack and the drag coefficient values at low angles of attack, that were slightly high. Comparisons of the measured results with numerical predictions from the XFOIL code and the EllipSys2D code showed good agreement. Measurements with the airfoil in pitching motion were carried out to study the dynamic aerodynamic coefficients. Steady inflow measurements at high angles of attack were used to investigate the double stall phenomenon.

The Danish Energy Agency funded the present work in the contracts,
ENS-1363/94-0001, ENS-1363/95-0001 and ENS-1363/97-0002.

ISBN 87-550-2300-2
ISSN 0106-2840

Information Service Department, Risø, 1998

Contents

1 Introduction

The development of modern airfoils for use on wind turbines was initiated in the 1980's. The requirements for such airfoils differ from standard aviation airfoils, because of structural reasons and extensive aerodynamic off-design operation conditions. Wind turbine airfoils operate frequently under fully separated flow when stall is used for power regulation at high wind speeds. Even in the case where traditional aviation airfoils are used on wind turbines, their performance needs to be verified in the entire operational range and at suitable Reynolds numbers. Eventually these airfoils are modified for improved performance by aerodynamic devices, such as vortex generators and gurney flaps. Thus there is a need for continuos testing of new airfoil configurations.

Modern airfoils are to a large extent developed from numerical calculations and optimization studies. Flow conditions such as separation at high angles of attack, laminar separation bubbles and transition from laminar to turbulent flow are difficult to predict accurately. Hence, testing of airfoils is an important issue in airfoil design. Tests of subsonic airfoils for wind turbines are carried out by a number of different research institutes, among these National Renewable Energy Laboratory, NREL, USA [2], Delft University, NL [3] FFA, S [4] and The University of Southampton, UK [6]. Such tests demand the availability of suitable wind tunnels that are often available from the general aviation industry and research. So far, testing of airfoils under typical wind turbine operation conditions was not possible in Denmark and was instead carried out by foreign cooperation partners, such as [4], [5] and [6].

In the autumn of 1993, a newly build wind tunnel became available in Denmark. The tunnel is of the closed return type with a 3.4x3.4 m open jet blowing into a test section with a cross section of 7.5x7.5 m, which is 10.5 m long. The tunnel was in 1994 used for 3d tests of a full-scale non-rotating LM 8.2 blade [14]. These tests show promising results, and confirm that the flow quality allows the use of the tunnel for tests of 2d airfoil sections, though it is obvious, that the tunnel test section is not ideal for obtaining 2d flows.

This report presents the developed facility for the experimental testing of 2d airfoil sections for use on wind turbine blades. The aim is to document the testing facility by reporting both static and dynamic pressure distribution measurements for the well known, NACA 63-215 airfoil [1]. The measurements include static and dynamic measurements up to angles of attack around 30°. The airfoil section was mounted horizontally in a test stand with endplates to ensure 2d flow conditions. The flow was free to expand in the vertical direction, but bound by the test section floor at a distance of 3.5 chords below the airfoil.

Overall requirements to the test method were:

- To become able to carry out both static measurements and dynamic measurements with the airfoil in pitching motion.
- To allow testing of Reynolds numbers until 1.5×10^6, achieved by a flow velocity of 40 m/s and airfoil chord up to 0.60 m.
- To limit the period from airfoil design to airfoil test, involving molding of the airfoil section, mounting of the pressure tubes, testing and evaluation of results.
- To accomplish a cost effective testing by intensive use of the tunnel time, which is rented on an hourly basis. The intensive use of the tunnel is also dictated from geographic reasons, since the tunnel is located away from Risø.

The report was structured in the following chapters:

Chapter 2 describes the experimental setup, the wind tunnel and the data acquisition system.

Chapter 3 describes the implementation of wind tunnel corrections to measured raw data.

Chapter 4 evaluates the wind tunnel flow conditions for calibration of static pressure and velocity and a proper wind tunnel reference is established for the non-dimensional reporting of airfoil aerodynamic forces.

Chapter 5 describes the methods used to calculate velocities, pressures and airfoil lift, drag and moment coefficients, including the total drag coefficient from the wake rake.

Chapter 6 contains the measured static and dynamic results together with an analysis of ‘double stall’ measurements.

Chapter 7 is the report conclusions

Appendix 1 is a more detailed description of the performed measurements for use in future exploitation of the results.

2 Experimental set-up

The present chapter describes the experimental setup. The description includes the wind tunnel test section, the test stand, the airfoil section, the wake rake and the data acquisition system.

2.1 The wind tunnel

The VELUX wind tunnel is of the closed return type with a practically open test section. The test section has a cross section of 7.5x7.5 m and a length of 10.5 m and the dimensions of the 'active' test section are determined by a jet nozzle of adjustable dimensions (maximum 4.0x4.0 m, minimum 3.4x.3.4 m). For the needs of the present tests the small jet nozzle of 3.4x3.4 m is used. The jet nozzle protrudes 1.75 m into the test section and blows the air towards the exit, which is a nozzle of dimensions 4.0x4.0 m. The maximum flow velocity achieved in the tunnel depends on the nozzle dimensions and when the small nozzle is used the maximum velocity is around 45 m/s. A perspective drawing of the tunnel test section is shown in Figure 2-1. In Figure 2-2 and Figure 2-3 the tunnel test section is shown with the test stand installed from different view angles, in order to give the reader a feeling of the tunnel's size relative to the test stand and the airfoil section. The test section floor is equipped with a turntable of 2 m in diameter on which the test stand is fastened. The test stand and the airfoil section are assumed perpendicular to the tunnel flow once the leading edge of the airfoil section is adjusted parallel to the nozzle exit.

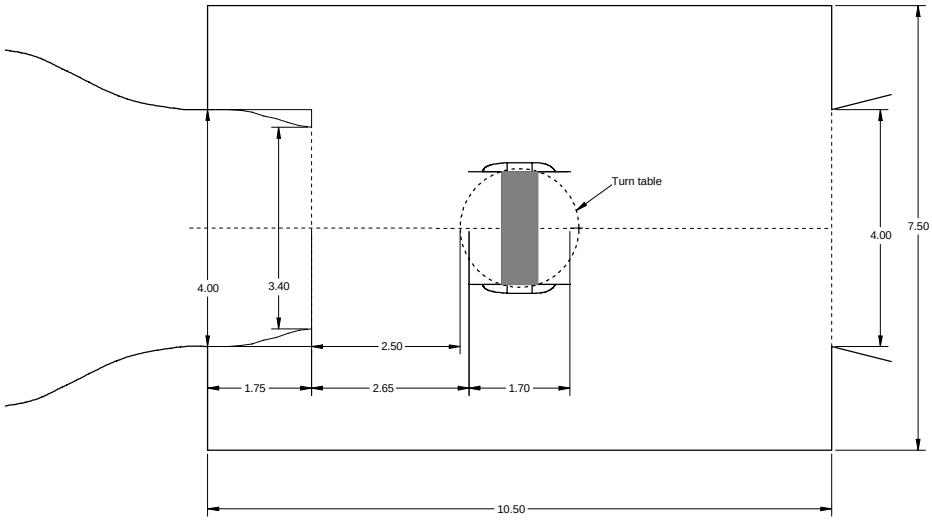

Figure 2-1 A schematic drawing of the wind tunnel test section with the test stand.

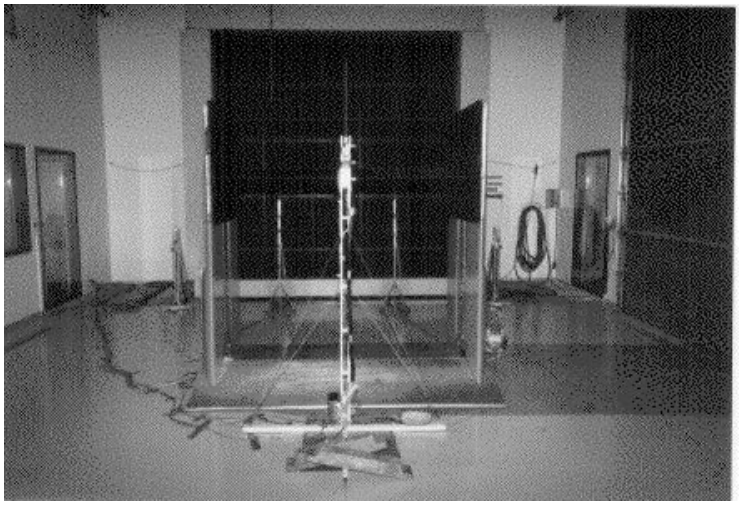

Figure 2-2 The test section when looking upwind. The adjustable jet nozzle can be seen behind the test stand

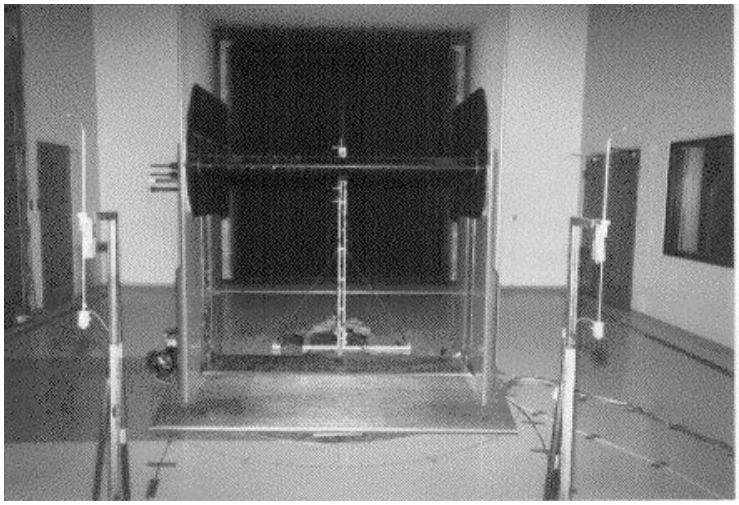

Figure 2-3 The test section when looking downwind.

2.2 The test stand

The tunnel in itself is not well suited for 2d airfoil section testing, and a test stand was built for that purpose. It consists of three metal U-profiles assembled together to form an inverse Π. To reduce flow disturbances, the stand is given a smooth aerodynamic shape, achieved by the use of ferrying surfaces with gentle slopes around the metal profiles. Airfoil sections of approximately 1.9 m width, mounted approximately at 1.7 m from the tunnel floor and 2.8 m from the nozzle inlet, can be tested with this stand. The airfoil section used in the present tests has a chord of 0.45 m, which means that the aspect ration of the airfoil section is 4.25.

The airfoil section must either span the width of the test section or be confined between vertical walls placed inside the tunnel. In the absence of end walls 3d flow effects will occur. A consequence of this would be a non-uniform distribution of the circulation along the airfoil and because of this a non-uniform distribution of the angle of attack. To avoid end effects in the present tests, endplates are used. The endplates are fixed to the test stand and do not

turn with the angle of attack. The endplates have to be placed as close to the airfoil as possible, to limit 3d effects. At the same time they should not come in contact with the airfoil and influence its motion during operation. In order to minimize the clearance between the endplates and the airfoil section, the horizontal position of the endplates is adjustable by a few millimeters with the help of a set of bolts. The combination of these adjustments with the use of fillers between the airfoil and the endplates during mounting ensures that the clearance during operation does not exceed one millimeter in the worst case. To allow quick interchange of airfoils during the tests each endplate is split into an upper and a lower part.

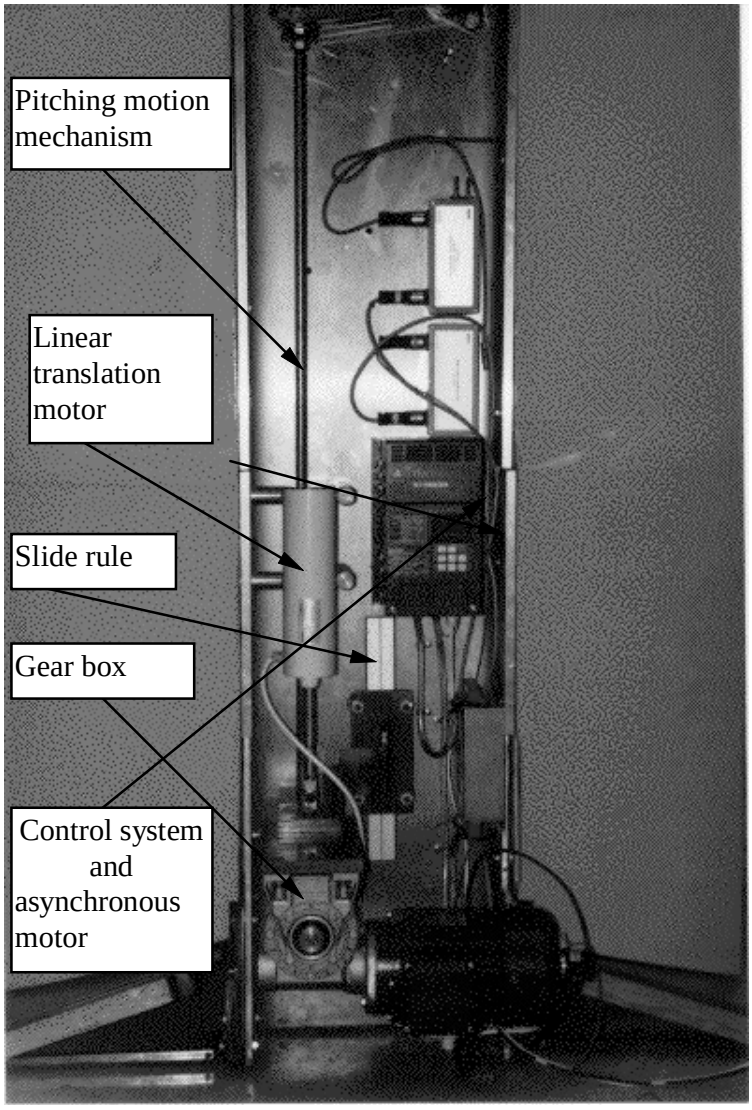

Figure 2-4 The mechanism that allows static and dynamic measurements to be made.

Figure 2-4 shows the instruments embedded to the side of the test stand. Both static and dynamic measurements are possible with this stand. Static tests comprise measurements at different angles of attack that can be adjusted continuously. They take place with the help of a linear translation motor that moves a steel rod in the vertical direction. The dynamic measurements involve pitching of the airfoil section at different amplitudes and different reduced frequencies. A pitching motion mechanism, driven by an asynchronous motor, can pitch the airfoil section at pre-defined amplitudes and frequencies. This is achieved by introducing a perforated circular plate between the steel rod and

the gearbox. The plate has holes at different radial positions that correspond to amplitudes from 2° to 5°. Different amplitudes can be achieved by selecting the proper radial distance. A control and feed back electronic system together with a suitable gearbox (gear ratio) makes possible a wide range of reduced frequencies. If different frequencies are wanted then the gearbox is interchanged. The pitching mechanism is suspended from the linear translation motor, which slides the mechanism in the vertical direction. Thereby it is used to control the angle of attack during static tests. To achieve a continuous slow pitching of the blade, a regulating power supply unit is used.

2.3 The airfoil section

The airfoil section model tested is the NACA 63-215. The span of the model is 1.9 m and the chord is 0.45 m. Originally it was manufactured and tested by FFA in a Danish funded project [4]. FFA borrowed the model to Risø and provided both the airfoil cross section coordinates and the locations of the taps.

The airfoil section is equipped with 64 pressure taps. Of these taps 57 are situated along the chord at the centerline. The location of the pressure tabs can be seen in Figure 2-5 where the FFA model is compared with the theoretical coordinates from [1]. The distribution of the tubes in the chordwise direction is non uniform, with more tubes situated around the leading edge where the flow is accelerated. The overall agreement between the actual FFA model and the theoretical coordinates is good in the leading edge region. However at the trailing edge, due to manufacturing reasons, the FFA model thickness is increased compared to the theoretical coordinates.

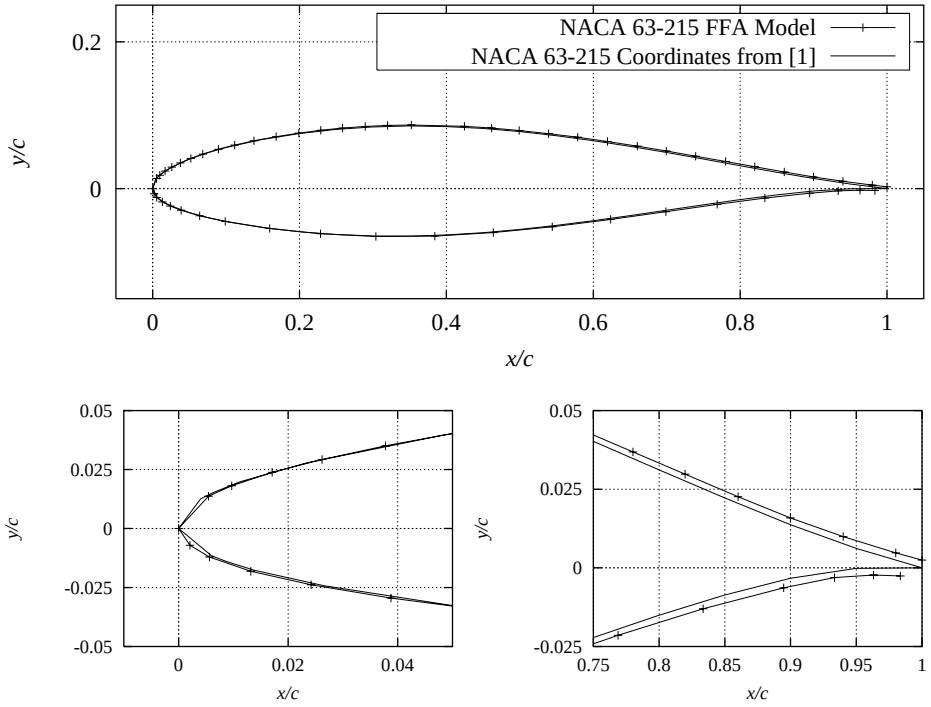

Figure 2-5 NACA 63-215 airfoil section where each symbol is a pressure tab. The FFA model is compared with the theoretical coordinates from [1]. The leading edge and the trailing edge regions are shown enlarged.

Holes are drilled on the surface and metal tubes are fitted to the holes and mounted flash with the surface. Flexible plastic tubes are mounted at the ends of the metal tubes. The tubes exit assembled from the airfoil section through a hollow suspension axis, Figure 2-6. To minimize flow disturbances, which may influence the flow and lead to premature transition, the holes are in a staggered arrangement along the span of the airfoil section.

Figure 2-6 The pneumatic plastic tubes exit from the suspension axis of the airfoil section.

The airfoil section is suspended on two vertical metal profiles of the test stand by two metal axis fitted on two bearings, Figure 2-6 and Figure 2-7. A wind direction resolver is fastened on the opposite side axis to measure the changes of the angle of attack, Figure 2-7.

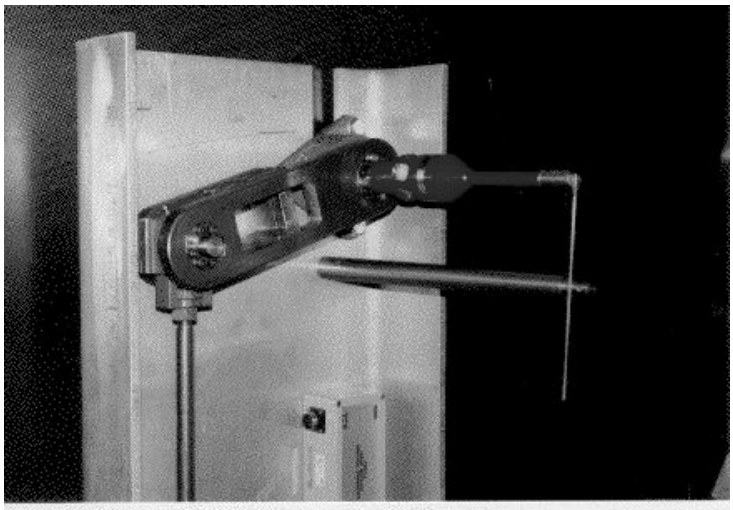

Figure 2-7 The wind direction resolver used for measurement of the airfoil section angle of attack.

2.4 The wake rake

The wake rake can be seen in Figure 2-8 and Figure 2-9. It consists of 54 total pressure probes of 1 mm inner diameter and five 4 mm inner diameter static tubes. The span width covered by the static tubes is 0.456 m. The distribution

of the total pressure tubes in the rake is non uniform and towards the middle of the rake, see Figure 2-9, the tube spacing is more dense compared to the rake ends. The five static tubes are spaced equidistant.

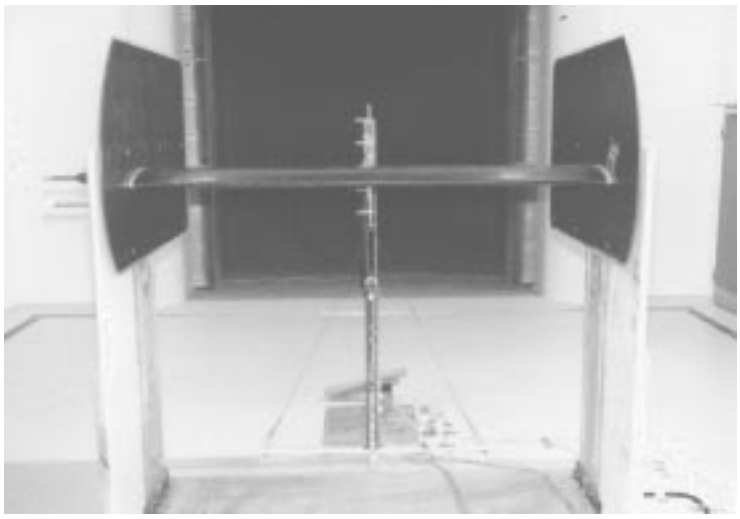

Figure 2-8 The wake rake behind the test stand.

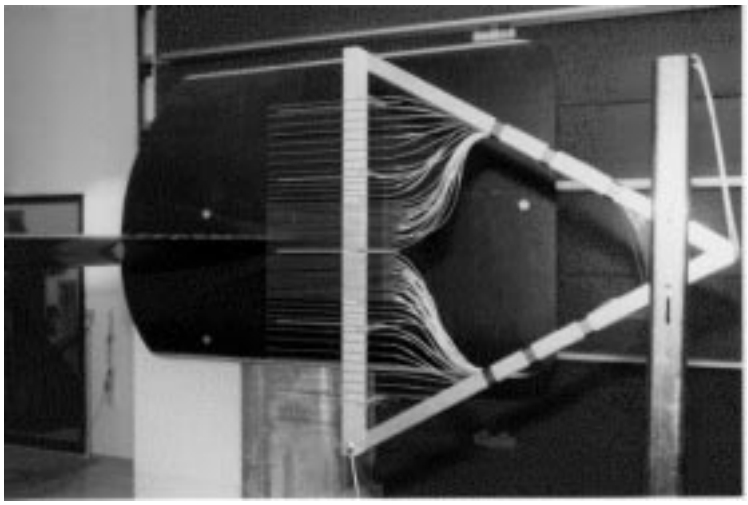

Figure 2-9 The wake rake seen from the side.

The rake is rigidly mounted on a metal mast behind the airfoil section, Figure 2-9. The metal mast is fastened both to the test stand and on a rectangular base by four supporting wires to avoid vibrations due to excitation of the construction. During the tests the distance from the head of the static tubes to the airfoil section trailing edge is 0.7 chords and the middle of the wake rake is placed at the height of the trailing edge at 0° inclination. The rake cannot be traversed in either the horizontal or the vertical direction. Hence, its center does not follow the translation of the minimum of the pressure deficit due to the change in the angle of attack and the streamline curvature. At higher angles of attack the deficit is not as accurately described as in the case of the smaller angles due to the larger distance between the total pressure holes. Another reason for the failure of the wake rake at higher angles of attack is that the flow around the airfoil separates and becomes highly unstable and the measured wake drag cannot be considered as representative of the airfoil drag.

The measurement of both the total and static pressures takes place by using a 10´´ H_20 pressure module. When the static pressure is needed between the static pressure tubes at the location of the corresponding total pressure holes, the static pressure is found by linear interpolation.

2.5 The data acquisition system

The data acquisition system used in the present tests is the HyScan 2000 system of Scanivalve Corp. It is a combination of both hardware and software and consists of two ZOC33 pressure-scanning modules used to record the pressure signals and a ZOCEIM16 module used for the rest of the electrical signals.

The ZOC33 consists of an electronic pressure scanner that accepts 64 pneumatic inputs that are directed to 64 silicon pressure sensors. The sensors convert the pressure signals to electrical output that can be read by a computer. Each module is equipped with a calibration valve, a high speed (50 kHz) multiplexer and an instrumentation amplifier. By multiplexing the inputs of the three modules, the total sampling speed can thus reach 100 kHz. The pressure sensors are collected in groups of eight, which allows incorporation of various pressure ranges within the same module.

The calibration valve can be operated in four different modes:

- operate
- calibrate
- purge
- leak test.

Applying the appropriate pneumatic control activates these modes. As a result the pressure modules can be calibrated/checked during a measurement session. The architecture of the pressure scanner is seen in Figure 2-10. As the silicon pressure sensors are known to be temperature dependent, the modules are placed inside thermal control units (TCU). The TCU is designed to provide a constant temperature environment for the pressure scanners while being equipped with electrical and pneumatic connections, thus functioning as an intermediate between the ZOC and the rest of the system.

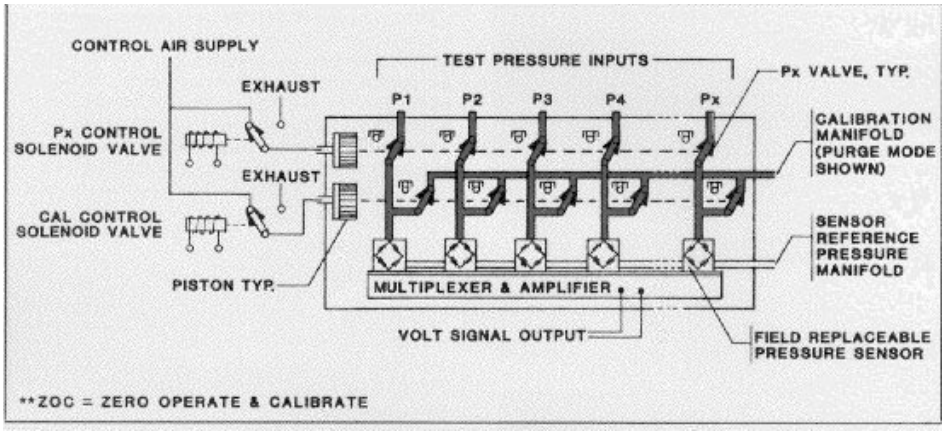

Figure 2-10 The architecture of the pressure module.

In the present tests the module used to record the blade pressures consists of 40 1 psi and 24 2.5 psi sensors. The latter ones are used to record the pressures

around the leading edge. The module used for the measurement of the wake rake pressures is a 10´´ H_20.

Besides the ZOC modules, the HyScan 2000 system comprises the following:

- The IFM 2000 ZOC module, interface to the module units containing line drivers and addressing circuitry.
- The CSM 2000 unit (cable service module) used to service the ZOC modules. It can support up to eight ZOC modules. Its function is to provide the modules with DC power. It receives address information from the IFM 2000 and sends the analogue signals from the ZOC modules to the IFM2000.
- The CPM 3000 (control pressure module) which contains the valves necessary to switch the ZOC calibration valves in one four modes of operation.
- The SPC 3000 (secondary pressure standard) which is used to calibrate the pressure modules since it can provide known calibration pressures.
- A data acquisition board plugged inside the computer, which can sample up to 100 kHz.

At normal operation, a total of 134 signals are measured by the data acquisition system:

- 64 Airfoil surface static pressures
- 5 wake rake static pressures
- 53 wake rake total pressures
- 3 Pitot tube static pressures
- 3 Pitot tube total pressures
- Angle of attack
- Air temperature
- Air density
- 2 strain gauges for recording shaft bending
- Electric motor frequency

The latter six signals are those sampled via the ZOEIM16.

2.6 Aerodynamic devices

In some of the measurements, leading edge roughness was simulated by sandpaper mounted on the airfoil suction side from the leading edge to 5% chord. The type NAXOS, grain size 120, width 32 mm was used. Leading edge roughness was not applied to the pressure side.

3 Wind tunnel boundary corrections

The flow conditions in the wind tunnel test section are not the same as those in free flow. Both closed jet as well as open jet boundaries produces extraneous forces, that must be taken into account. Additionally a longitudinal static pressure gradient is also present in the test section. There is a large amount of literature available on closed jets and ventilated wall wind tunnels, as, e.g., [7]. However, open jet test sections are rarely used for 2d testing, and only a few references were available to the present study, [6 - 8], [15].

Because the cross section of the test section is larger than the inlet nozzle cross section, the jet flow is free to expand and the tunnel is an open jet tunnel. Since the airfoil section does not span the width of the jet, endplates have to be mounted to the ends of the airfoil section to approximate 2d flow. The small clearances between the airfoil section and the endplates, the finite size of the endplates and the presence of the floor and the ceiling introduce uncertainties on the wind tunnel corrections.

The wind tunnel corrections do not take into account additional effects from customary failings of the wind tunnel, such as non-horizontal flow in the test section, local variations in velocity and pressure and interference and disturbances. The variation in velocity and pressure will be dealt with in chapter 4. The remaining effects are assumed to be negligible.

The following wind tunnel corrections were considered:

- Solid and wake blockage
- Horizontal buoyancy
- Down-wash
- Streamline curvature

Solid and wake blockages are constraints to the flow pattern that increase with wake size and blocking of the tunnel cross section. These are important for a closed jet tunnel, but are usually negligible for open jet flows, since the flow is free to expand [7].

In the case of tunnels with closed test sections horizontal buoyancy results from the thickening of the boundary layer as it develops in the downstream direction within the test section. The free flow area is reduced, the flow accelerates and as a result the density of the streamlines is increased and there is a drop in the static pressure along the test section. This pressure-drop results in a drag force on the airfoil section. In the case of tunnels with open test sections, the pressure drop is very limited and so is the influence of horizontal buoyancy [7].

For an open jet flow, the remaining two corrections, down-wash and streamline curvature, are significant and they are explained in the following. These corrections are applied directly on the lift coefficient, C_L, the drag coefficient, C_D and the moment coefficient, C_M, but not on the airfoil pressure distribution.

3.1 Down-wash

Two-dimensional testing is usually carried out with an airfoil section that spans the tunnel dimensions, or an airfoil section confined between 'infinite' walls of large dimensions compared to the dimensions of the airfoil section. However, in the present case the width of the open jet exceeds the span of the airfoil.

The airfoil section is a finite wing and according to Prandtl's theory, the flow past a finite wing can be represented by the flow past a vortex system formed of a vortex sheet bound to the airfoil and a free vortex sheet which represents the flow in the wake.

For such an airfoil of large aspect ratio a single vortex line of varying strength (lifting line) can approximate the bound vortex. Then the velocity at any point of the lifting line is the resultant of the free stream velocity and an induced velocity (down-wash velocity) normal to the free flow direction. The down-wash velocity is the result of the vortex system. For a positive C_L with the airfoil suction side pointing upward the down-wash velocity points in the downward direction. The down-wash velocity reduces the angle of attack, α, and the slope of C_L and at the same time increases C_D.

To limit 3d effects in the present case, endplates have been used. Their efficiency depends on their size and on their proximity to the ends of the airfoil section to limit the formation of tip vortices and subsequent trailing vorticity. In the present case a trade-off was decided so that the size of the endplates was increased while a clearance of the order of one mm between them and the airfoil was allowed by keeping them mounted on the test stand instead of mounting them directly on the blade. However, manufacture and transportation reasons prevented very large endplates.

Numerical Navier-Stokes calculations of the down-wash from the clearances and from the limited size of the endplates were not possible. Instead, the actual size of the endplates was taken into account by application of the simple analytical method of Mangler [15].

For an airfoil span with endplates Mangler [15] established the following expressions for α and C_D:

$$\alpha = \alpha_t - \kappa \frac{1}{2\pi A} C_{Lt} \left[rad \right]$$

(3-1)

$$C_D = C_{Dt} - \kappa \frac{1}{2\pi A} C_{Lt}^2$$

Where α_t is the measured angle of attack, C_{Lt} is the measured lift coefficient, $A = b/c$ is the aspect ratio, b is the span, c is the chord, C_{Dt} is the measured drag coefficient, κ is a function of endplate height and span width and estimated to 0.55 based on Figure 11 in [15].

In the present case, the dimensions were, b = 1.90 m and c = 0.45 m. Taking C_{Lt} = 1.0 as example this results in a change in angle of attack of, $\Delta\alpha$ = 1.2°, and an

induced drag of, ΔC_D = -0.021. Compared to an airfoil section without endplates, down-wash was reduced by 45%.

3.2 Streamline curvature

Streamline curvature is introduced to the jet flow when the flow is free to diverge from its original direction downstream of the airfoil section. In open jets, this effect is usually large because the tunnel walls do not bound the jet flow. The curvature of the tunnel flow induces both drag and changes of the effective angle of attack. As a result the measured C_D is too large and the slope of the C_L curve is too small.

In the following, the results of two analytical correction methods from Garner et al. [8] and Brooks et al. [9] are compared to results of numerical Navier-Stokes calculations of the flow field. It is assumed that in this flow field the airfoil is placed in an open jet flow with open top and bottom boundaries. Solid walls or large endplates are present to preserve the two-dimensionality of the flow. It is also assumed that the airfoil is placed in the middle of the open jet at $h/2$, where h is the jet height.

Both analytical methods use the method of images where the airfoil is replaced either by a single vortex or a distribution of vortices along the chord and the flow field is approximated by a series of image vortices with respect to the vertical dimensions of the jet. Figure 3-1 shows the model of the 2d tunnel flow, where the airfoil chord, c, the upstream distance to the nozzle, d, and h are the important dimensions. The airfoil is replaced by a single vortex while the flow is approximated by the image system seen in Figure 3-1. This corresponds to a cascade flow.

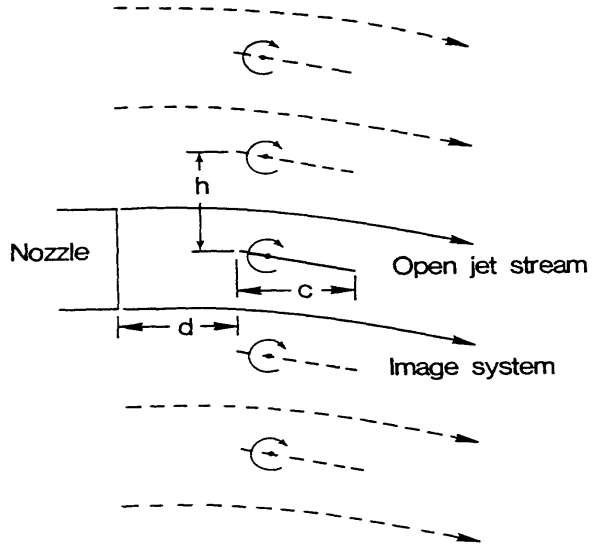

Figure 3-1 Airfoil and image system employed for derivation of 2d open jet wind tunnel correction (ref. [9]).

Method of Garner et al.

The method of Garner et al. [8] is first order accurate. A balance of momentum is used together with the vortex image system. The results are obtained by using a flat plate of chord, *c*, placed midway between the boundaries of the simulated open test section of a wind tunnel and at an angle of, $\alpha_t = 10°$. To simulate the circulation around the plate, a single vortex at $x = ¼\ c$ is used. It is assumed, that the interference down-wash at the plate is half that in the distant wake.

The free flow angle of attack, α, is found from:

$$\alpha = \alpha_t - \frac{1}{2\pi}\left(\frac{L_o}{L} - 1\right) C_{Lt}\,[rad] \qquad (3\text{-}2)$$

Where C_{Lt} is the measured lift coefficient and α_t is the measured angle of attack. The 2d lift divided by the total lift, L_0 / L, is found from Figure 3-2. (c/h = $0.4/3.4 \approx 0.11 \Rightarrow L/L_0 \approx 0.88$).

The free flow drag, C_D, is found from:

$$C_D = C_{Dt} - \frac{1}{2\pi}\left(\frac{L_o}{L} - 1\right) C_{Lt}^{\ 2} \qquad (3\text{-}3)$$

Where C_{Dt} is the measured drag.

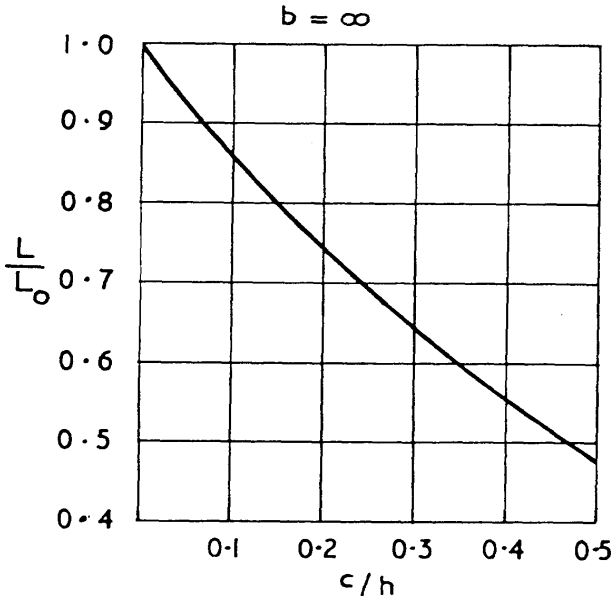

Figure 3-2 L/L_0 shown as function of chord to tunnel height ratio, c/h (ref. [8]).

Method of Brooks et al.

The method of Brooks et al. [9] is of higher order accuracy compared to Garner et al. [8]. It involves additional terms on the correction of the angle of attack and a correction of the moment coefficient. Compared to Garner et al. [8], the circulation around the airfoil is not replaced by a single vortex, but by vortices distributed along the airfoil chord.

The free flow moment coefficient, C_M, is obtained:

$$C_M = C_{Mt} - \frac{\sigma}{2} C_{Lt} \qquad (3\text{-}4)$$

Where C_{Mt} is the measured moment coefficient, C_{Lt} is the measured lift coefficient and σ is defined as:

$$\sigma = \frac{\pi^2}{48} \cdot \left(\frac{c}{h} \right)^2 \qquad (3\text{-}5)$$

The free flow angle of attack, α, is found from:

$$\alpha = \alpha_t - \frac{\sqrt{3\sigma}}{\pi} C_{Lt} - \frac{2\sigma}{\pi} C_{Lt} - \frac{\sigma}{\pi} (4 C_{Mt}) [rad] \qquad (3\text{-}6)$$

The drag, C_D, is calculated from the correction due to the induced down-wash:

$$C_D = C_{Dt} + \left[- \frac{\sqrt{3\sigma}}{\pi} C_{Lt} \right] C_{Lt} \qquad (3\text{-}7)$$

Where C_{Dt} is the measured drag coefficient.

Navier-Stokes calculation

To confirm the results of the analytical methods, Navier-Stokes calculations were performed with the EllipSys2D code [12] on a cascade type flow, similar to the arrangement shown in Figure 3-1. The chord was in this case, c = 0.60 and the jet height, h = 3.4. The airfoil was the NACA 63-215 airfoil.

The cascade flow was compared to 2d free flow calculations to reveal the difference in α and C_D for equal C_L. Figure 3-3 shows the C_L curve for the free flow and for the cascade flow. The C_L curve slope was clearly lower for the cascade flow due to a change in angle of attack. A correction to the cascade flow was applied on basis of eq. (3-2) by adjusting the cascade flow angle of attack so that the corrected cascade flow C_L was in agreement with C_L at 8^o for the free flow:

$$\alpha = \alpha_t - 2.7 \cdot C_{Lt} \qquad (3\text{-}8)$$

Where α and α_t are given in degrees.

It appears from the corrected cascade flow C_L curve in Figure 3-3, that there is good agreement between the corrected cascade flow C_L curve and the free flow C_L. This is further supported by comparing the pressure distributions for the free flow at $\alpha = 7.5^o$ with results from the cascade flow at $\alpha = 10.0^o$ shown in Figure 3-4. It can be seen that the two pressure distributions coincide, which confirms the results of the lift distribution and the validity of the analytical calculation.

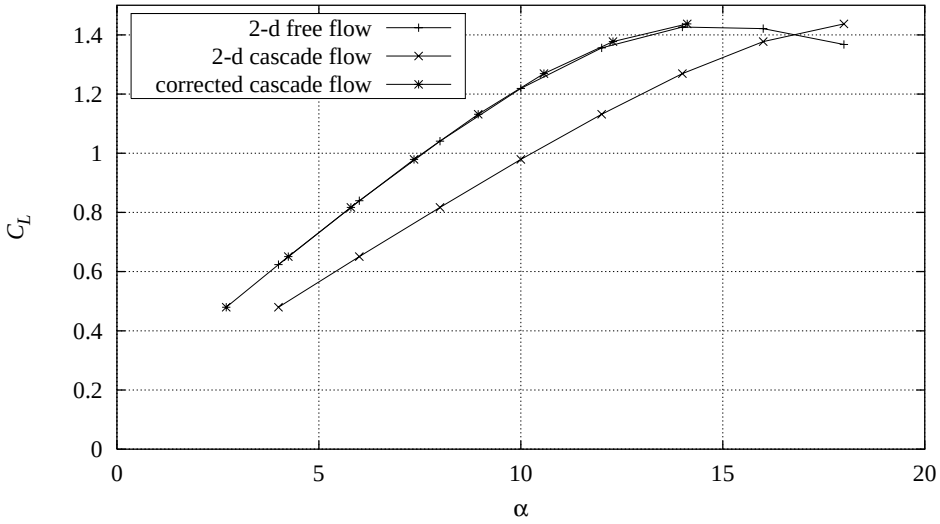

Figure 3-3 Calculated C_L curves for 2d free flow and 2d cascade flow compared to corrected cascade flow, EllipSys2D, NACA 63-215, Re = 1.3×10^6.

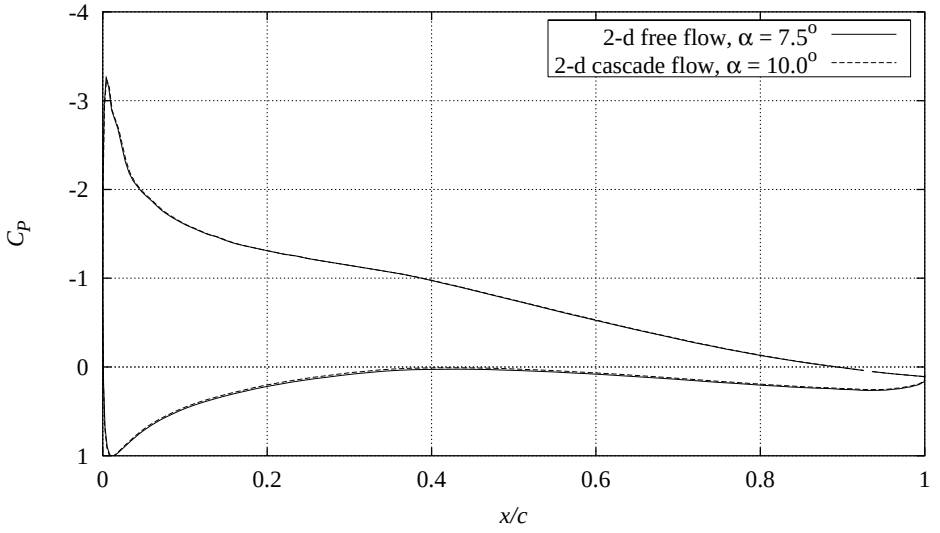

Figure 3-4 Calculated C_P curves for 2d free flow at 7.5° compared with 2d cascade flow at 10.0°, EllipSys2D, NACA 63-215, Re = 1.3×10^6.

The difference in C_D is shown in Figure 3-5. A correction to the cascade flow was applied on basis of eq. (3-3) by adjusting the induced drag so that the corrected cascade flow C_D was in agreement with C_D at 8^o for the free flow:

$$C_D = C_{Dt} - 0.045 \cdot C_{Lt}^{\ 2} \qquad (3\text{-}9)$$

The corrected cascade flow C_D is seen to fit the free flow C_D well.

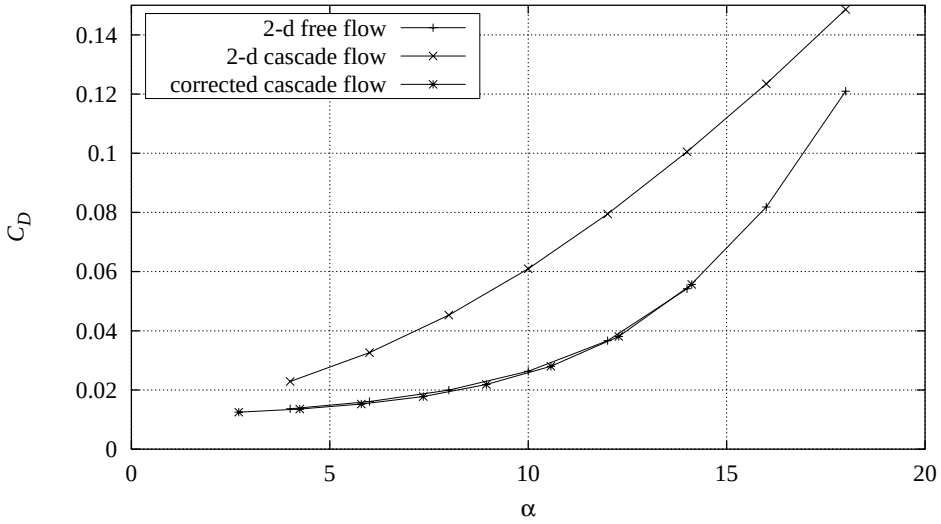

Figure 3-5 Calculated C_D curves for 2d free flow and 2d cascade flow compared to corrected cascade flow, EllipSys2D, NACA 63-215, Re = 1.3×10^6.

Comparison

The Navier-Stokes calculations have been compared with the results of two analytical methods. The dimensions are in this case, c = 0.45 and h = 3.4 corresponding to the wind tunnel and the actual airfoil section. The three methods are compared in Table 3-1 with C_{Lt} = 1.0 and C_{Mt} = 0.0. C_M is of minor importance to the correction.

We find L/L_0 = 0.82 in Figure 3-2 and $\sigma = 3.6 \cdot 10^{-3}$ from eq. (3-3). The resulting corrections are in very good agreement and either of the methods can be chosen. In the following the method of Brooks et al. [9] is applied.

Table 3-1 Comparison of the different analytic correction methods from [8] and [9] with Navier-Stokes calculations at c = 0.45m, h = 3.4m, C_L = 1.0.

	$\Delta\alpha$ (^{o})	ΔC_D	ΔC_M
Method of Garner et al. [8]	-2.00	-0.036	-
Method of Brooks et al. [9]	-2.04	-0.033	0.0018
CFD Calculations	-2.0	-0.03	-

3.3 Comparison and practical use

Both down-wash and streamline curvature result in a change in the angle of attack due to the appearance of an induced velocity normal to the flow direction and the airfoil section.

The combination of corrections for down-wash and streamline curvature is problematic. Because of different assumptions the corrections can not directly

be combined. Comparing the example calculation in Chapter 3.1 with Table 3-1 it can be seen that streamline curvature is more important than down-wash.

The streamline curvature correction assumes 2d flow with absent boundaries in the vertical direction, where the flow is free to expand. The floor is near to the jet in the present case and this will reduce the deviation of the flow. It is therefore chosen to apply the streamline curvature correction of Brooks et al. [9] and to neglect down-wash. The results in Chapter 6 support the validity of this.

4 Wind tunnel flow conditions

This chapter concerns measurements of the wind tunnel flow conditions. We investigate the quality of the undisturbed flow and establish the proper tunnel reference velocity and static pressure at the test stand. The wind tunnel reference is important for the proper normalization of the aerodynamic forces. Possible reference measurement positions are the Pitot tubes 1-3, see Figure 4-1. Pitot 1 and 2 are located near to the nozzle outlet at airfoil section height whereas Pitot 3 is placed above the wake rake. The reference measurements should be independent of the airfoil section flow field.

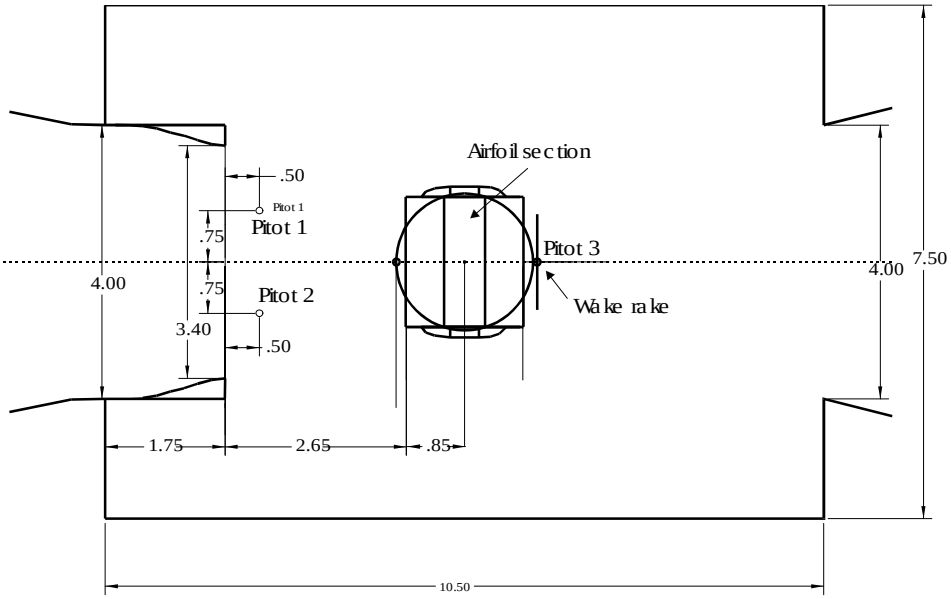

Figure 4-1 Sketch of the wind tunnel with Pitot 1-3 together with the test stand with the airfoil section and the wake rake behind the airfoil section.

To overall evaluate the quality of the flow field, the following investigations were carried out:

- To determine the mean velocity and the turbulence intensity at different locations long time series were measured at the different Pitot tube positions.
- To investigate the vibration of the test stand from the interaction with the flow field long time series were measured at the test stand with the airfoil section present.
- To determine the uniformity of the flow field at the nozzle outlet, measurements were taken on a line perpendicular to the flow direction at the airfoil section height.
- To take into account speed up effects and the static pressure loss, the development of the flow downstream towards the test stand was measured at several positions between the nozzle outlet and the test stand.
- To investigate the uniformity of the flow at the airfoil section, the flow at the test stand was measured in the cross-flow plane in the downstream direction at the airfoil section position in the test stand.

- To calculate total drag and to investigate the uniformity of the flow field at the wake rake, possible disturbances from the test stand and the blocking from the airfoil section wake rake measurements were taken with and without the airfoil section.
- Based on the different measurements reference values for velocity and static pressure were found from the pitot tubes 1-3.

The measurements refer to the coordinate system defined in Figure 4-2. The origin is on the centerline of the airfoil section at the position of the shaft, which is at 40% chord. The positive x-axis direction is downstream and the positive z-axis is toward the tunnel ceiling.

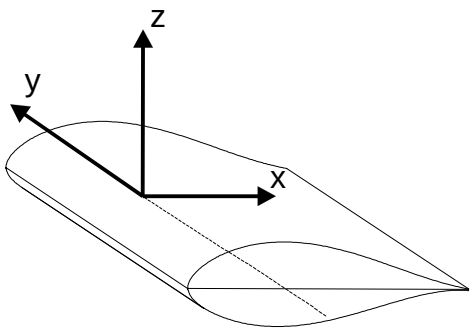

Figure 4-2 Coordinate system definition for the flow measurements in this chapter.

All measurements were taken at flow velocities of around 40 m/s. The results were compiled from different measurement runs and there were small differences in the velocities due to the starting and stopping of the wind tunnel and to the change in temperature. All measurements were corrected to standard temperature and pressure conditions. To be able to compare measurements from different runs, the measured velocities were given relative to the Pitot 1 velocity. Correspondingly, the static pressures were shown as the differential pressure relative to Pitot 1. Each measurement is explained in Appendix A1.

4.1 Mean velocity and turbulence

To determine the mean velocity and the turbulence intensity at different locations long time series were measured at the Pitot tube positions.

Figure 4-3 shows a part of a time series of the velocity at the Pitot 1 position from a 180 s record, sampled at 100 Hz. The airfoil section was mounted on the test stand. The mean velocity and turbulence intensity were found at different tunnel locations, Table 4-1. The turbulence intensity at the inlet was 1.0%. This was increased to 1.1% downstream at the Pitot 3 position. Comparisons of measurements with and without the airfoil section present showed that the turbulence intensity was not affected by its presence, Table 4-1.

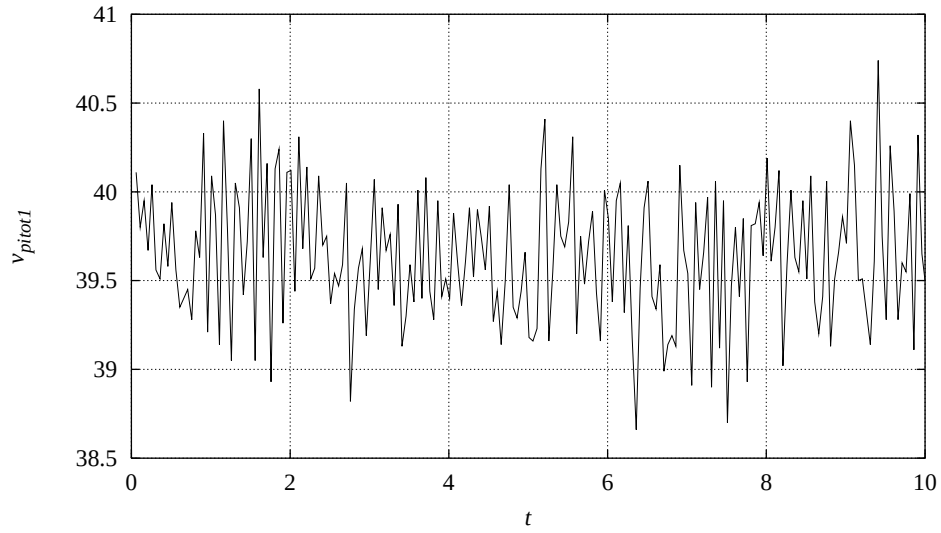

Figure 4-3 The velocity measured by Pitot 1 with the airfoil section mounted. Part of a time series from a 180 s record (NA63215STAT221196V1).

Table 4-1 Mean velocity and turbulence intensity at different wind tunnel locations. Values in brackets correspond to measurements without the airfoil section mounted. (NA63215STAT221196V2)

	Velocity (m/s)	**Velocity relative to Pitot 1**	**Turbulence intensity, I, (%)**
Pitot 1	39.65	-	1.0
Pitot 2	40.00	1.0088	0.85
Pitot 3	42.18	1.064	1.1 (1.2)
Wake rake	41.75	1.053	0.77 (0.73)

The Pitot tubes can not resolve the presence of high frequencies correctly because the pressures are measured through long tubes. Figure 4-4 shows the PSD spectrum corresponding to the time series in Figure 4-3.

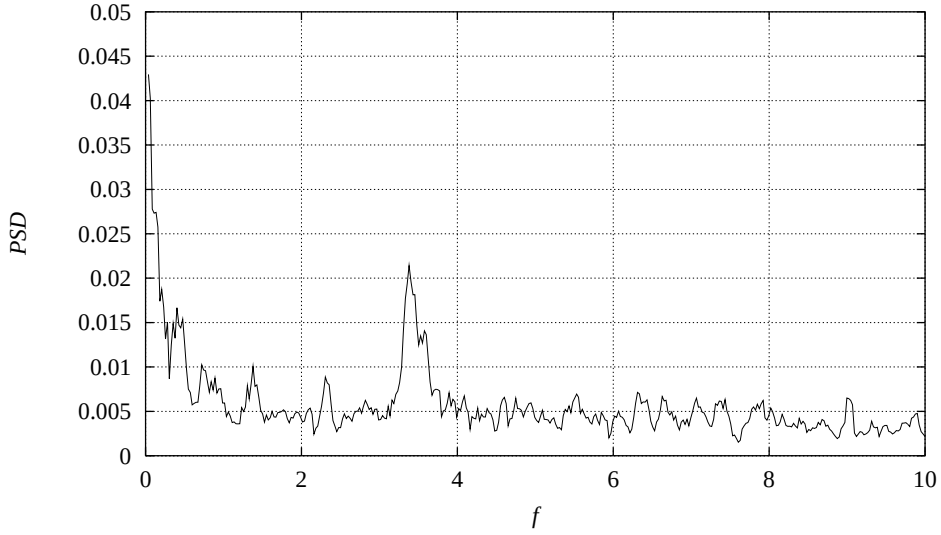

Figure 4-4 PSD spectrum of a velocity time series measured by Pitot 1 shown in Figure 4-3 (NA63215STAT221196V1).

There was a peak of energy at 3.4 Hz. This peak was also found for Pitot 2. It could not be determined whether this peak came from the jet itself, the inlet geometry or from vibrations of the Pitot stands. We did not find peaks at higher frequencies.

Figure 4-5 shows the PSD spectrum for a velocity time series from a 180 s record measured by Pitot 3. The 3.4 Hz peak was present, but was reduced in magnitude, while a harmonic at 6.6 Hz appeared.

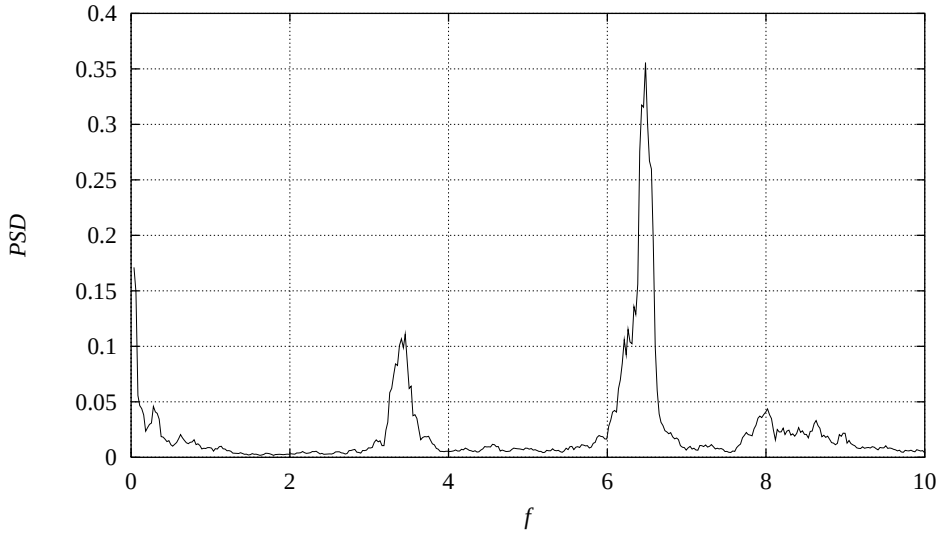

Figure 4-5 PSD spectrum of a velocity time series from a 180 s record measured by Pitot 3 (NA63215STAT221196V1).

4.2 Test stand vibration

To investigate the he vibration of the test stand from the interaction with the flow field long time series were measured at the test stand with the airfoil section present. Time series of the angle of attack, α, and the corresponding calculated lift coefficient, C_L, were analyzed.

Figure 4-6 shows a part of a 30 s long time series, sampled at 100 Hz. The angle of attack around $\alpha = 12.8^o$ and was not changed.

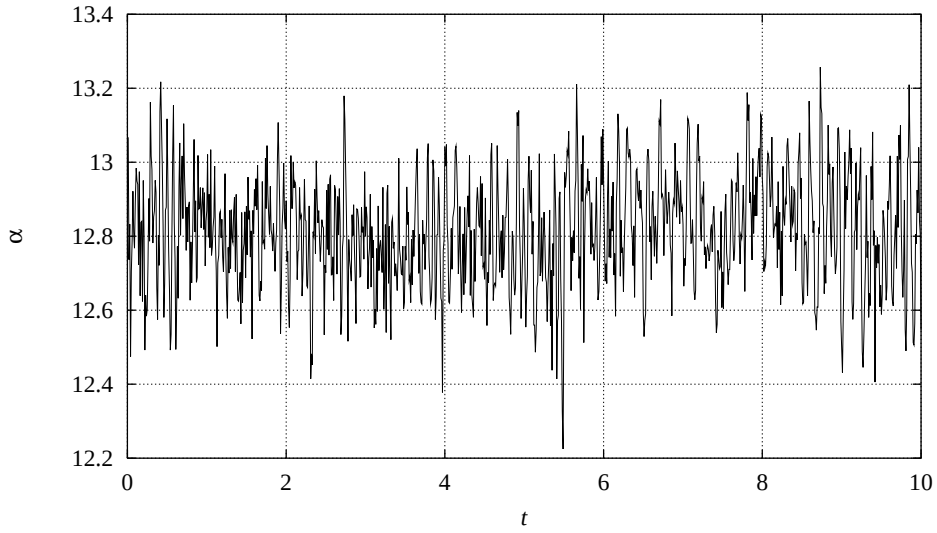

Figure 4-6 Part of a 30 s long time series, sampled with 100 Hz, of the angle of attack with the airfoil section mounted (NA63215STAT221196V1).

The corresponding PSD spectrum is shown in Figure 4-7. There were frequency peaks at 3.4, 6.6, 7.8, 13.9 and 15 Hz. The peaks at 3.4 and 6.6 Hz were also present in the flow, Figure 4-4 and Figure 4-5, whereas the higher frequencies originated from resonance from the test stand itself or from noise.

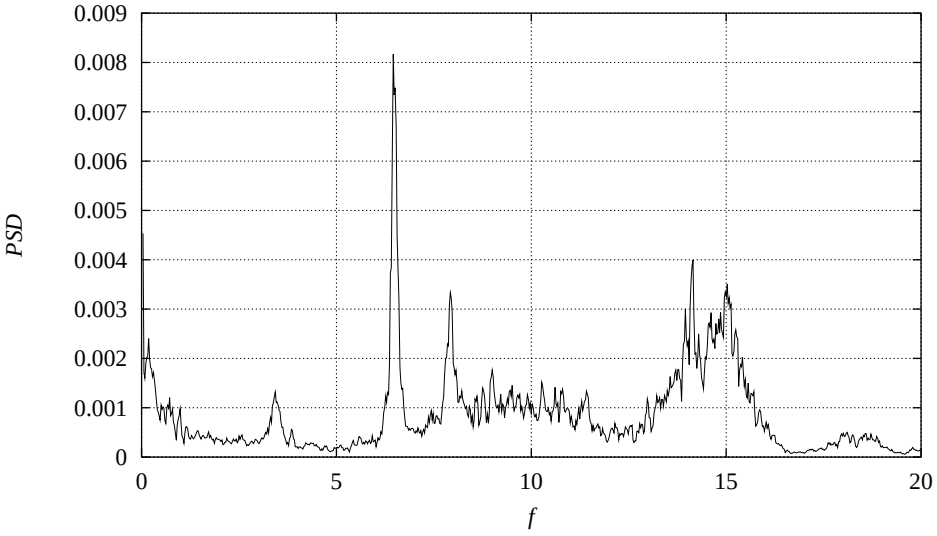

Figure 4-7 PSD spectrum of the angle of attack time series from Figure 4-6.

Figure 4-8 shows the PSD of C_L corresponding to the time series of α in Figure 4-6. The peak at 6.6 Hz was also present in the flow. Except for low frequencies there were no significant frequency peaks.

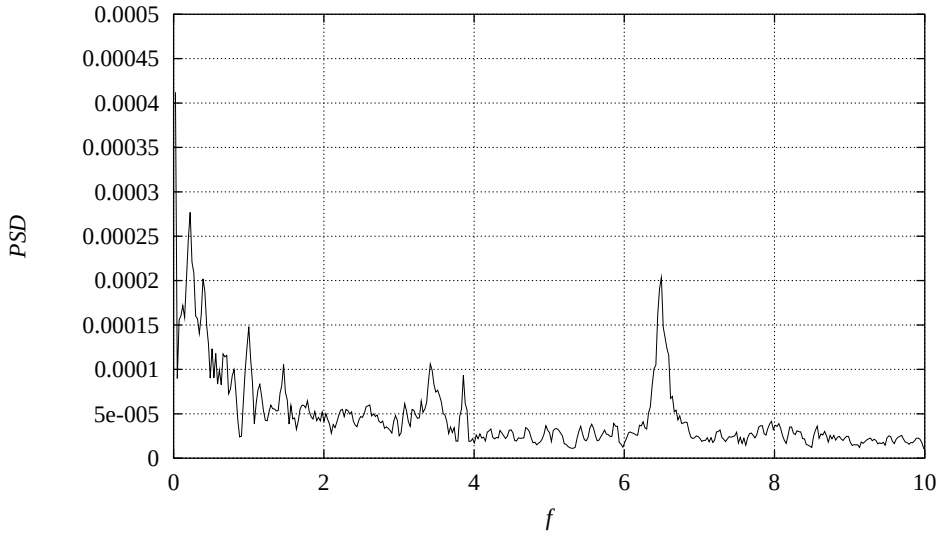

Figure 4-8 PSD spectrum of the C_L time series corresponding to the angle of attack from Figure 4-6.

From both Figure 4-7 and Figure 4-8, it is obvious that the energy contents of the spectra were limited and there were no severe resonance related to the test stand and the airfoil static pressure distribution measurements.

4.3 Nozzle outlet flow

To determine the uniformity of the flow field at the nozzle outlet, measurements were taken on a line perpendicular to the flow direction at the airfoil section height without the presence of the airfoil section.

Figure 4-9 shows the horizontal velocity profile at the inlet at the airfoil section height where, $z = 0$.

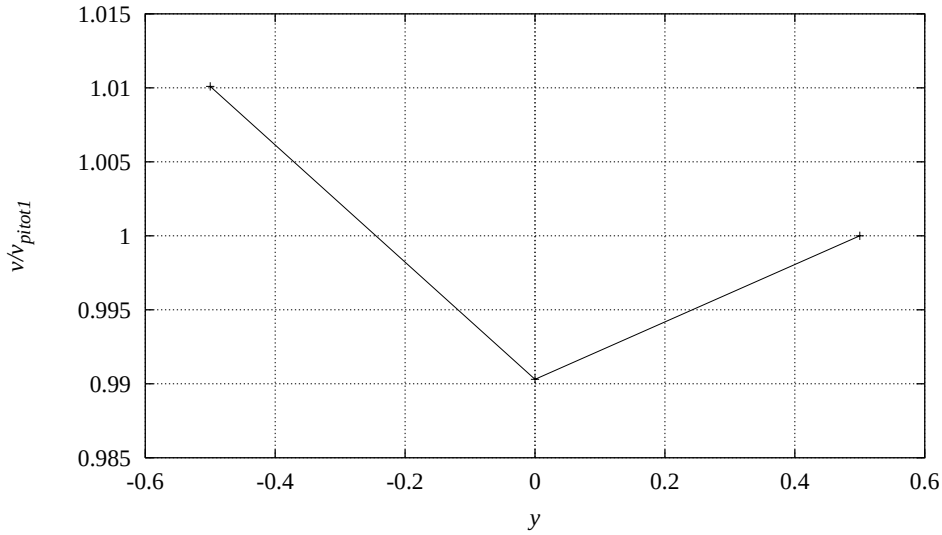

Figure 4-9 The horizontal velocity profile at the inlet at x = -3.00 m, z = 0.0.

Only three measurement points were available. The velocity profile presented a minimum at the tunnel centerline, while it was increased away from the

centerline toward the nozzle walls. The velocity profile was asymmetric and higher velocities were observed towards negative y-values. This was caused by the jet inlet geometry, where the flow was bend before the jet inlet.

The velocity can be expected to increase towards the nozzle walls because of the contraction of the jet. This is also found at lower velocities in earlier investigations by VELUX [10] and Risø [11]. The latter based on both Navier-Stokes calculations and measurements in the tunnel. The overall difference between the velocities was however small.

The velocity profile at the nozzle outlet vertical centerline can be seen in Figure 4-10, Section 4.4. At the inlet where, x = -3.0, the flow was accelerated toward the tunnel floor because of the jet contraction. The minimum velocity was observed at the airfoil section height at z = 0. Above z = 0 the velocity was again increased. Even though the horizontal centerline of the jet was located at z = 0.3, and minimum velocity could be expected here, the minimum velocity appears at z = 0.0 This was reproduced in several measurements. The variation was small and of minor importance.

4.4 Tunnel centerline flow

To take into account speed up effects and the static pressure loss, the development of the flow downstream towards the test stand was measured at several positions between the nozzle outlet and the test stand. Together with the Pitot tube measurements, this enables the establishment of the wind tunnel reference for velocity and static pressure.

Velocity

The vertical velocity profiles at the tunnel centerline are shown at different downstream positions in Figure 4-10. The airfoil section was not mounted in the test stand. The measurements at the test stand and downstream of the test stand were taken off the centerline, because of practical reasons.

Downstream from the inlet at, x = -1.15, the velocity profile was more uniform compared to the inlet at x = -3.0.

At the test stand position, the flow at the floor was accelerated because of the presence of the wooden ramp of height 0.30 m, that covers cabling and an iron I-beam. Except for the point nearest to the floor, the velocity profile was smooth. This indicated that the disturbances from the test stand were in general small, and this was important for the establishment of the proper reference, since the flow remained nearly constant at a large area around the airfoil.

Downstream of the test stand, the flow was almost entirely uniform and the velocity at the airfoil section was around 1.06% compared to the inlet Pitot 1. The flow towards the floor has passed the test stand and was decelerated to a smaller value compared to the test stand.

Figure 4-10 shows, that the velocity at the airfoil section height, z = 0, was increased in the downstream direction. This is also the case for the flow above the airfoil section. Figure 4-10 also shows that the vertical velocity profile at the test stand was almost uniform, except for near the floor.

As a general conclusion the flow accelerates as it proceeds downstream while at the same time becoming more uniform.

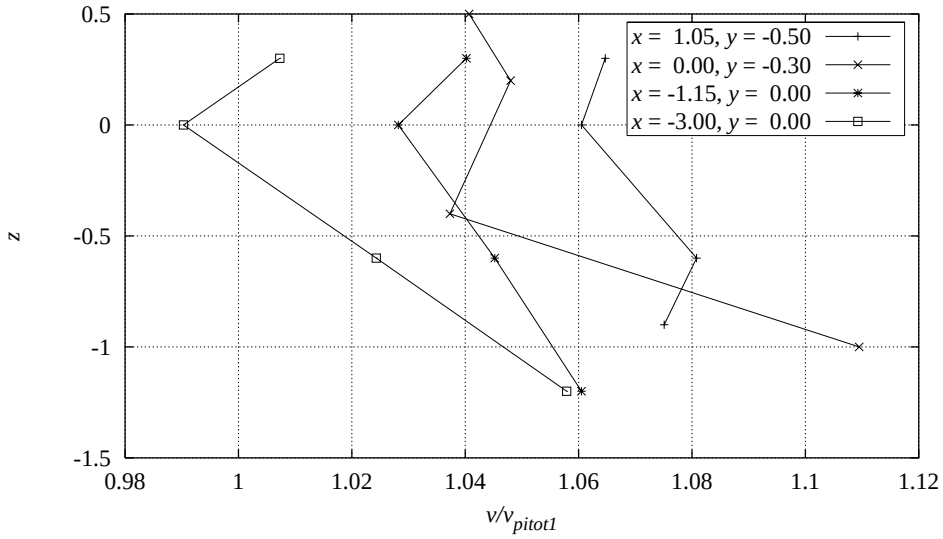

Figure 4-10 The vertical velocity profile in the tunnel centerline, without the airfoil section mounted, measured at different downstream positions.

The velocity along a streamline in the tunnel center plane at the airfoil section height is shown as function of the downstream tunnel distance in Figure 4-11. The measurement points upstream of the test stand were taken from Figure 4-10 whereas the point at the test stand was taken from Figure 4-14, Section 4.5. The point downstream of the test stand was taken from the wake rake. The three measurement points that are available upstream of the test stand showed a linear acceleration of the flow of 6.9%, from 99% at the inlet to 105.9% at the airfoil section. The reference flow velocity at the test stand could then be determined to 105.9% relative to the Pitot 1 velocity.

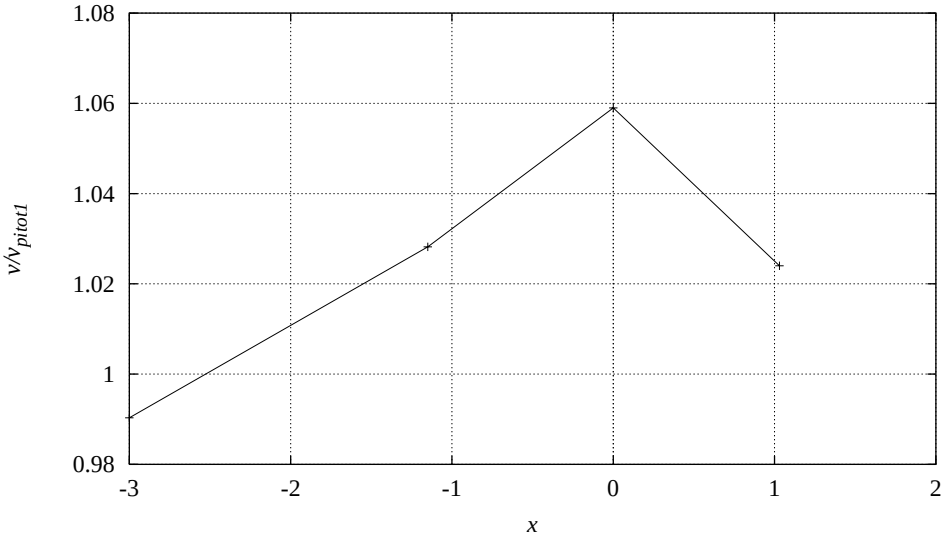

Figure 4-11 The velocity along a streamline in the tunnel centerline at the airfoil section height, z = 0, without the presence of the airfoil section.

Static pressure

The vertical variation of the static pressure at the tunnel centerline is shown in Figure 4-12. The static pressure was reduced in the downstream direction and this corresponded to the increase in velocity, Figure 4-10.

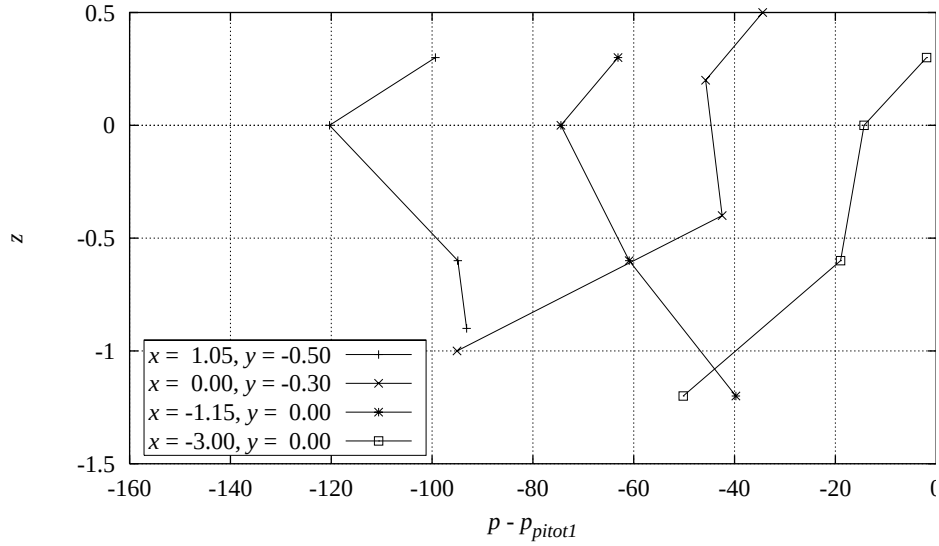

Figure 4-12 The vertical variation in static pressure at the tunnel centerline, measured at different downstream positions without the presence of the airfoil section.

The static pressure along a streamline in the tunnel center plane at the airfoil section height, $z = 0$, is shown in Figure 4-13.

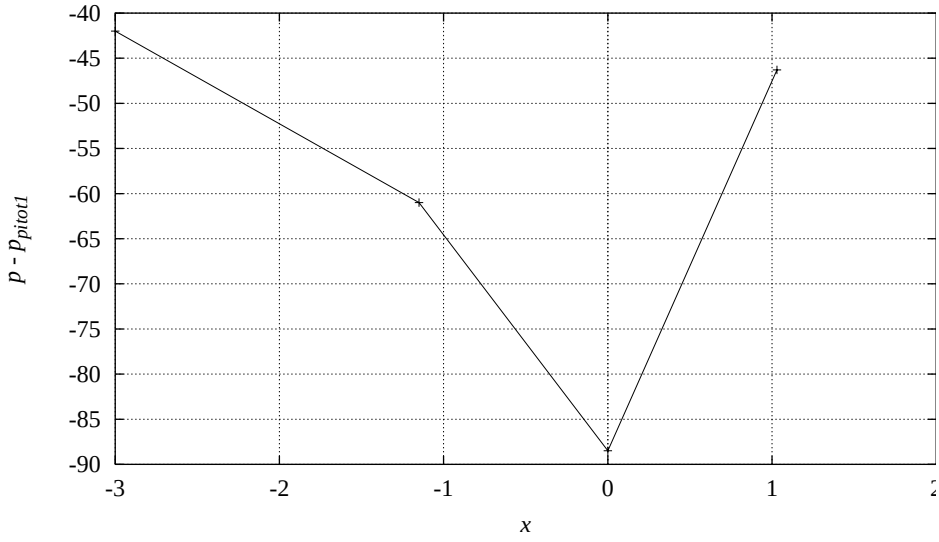

Figure 4-13 The static pressure along a streamline in the tunnel center plane at the airfoil section height without the airfoil section mounted.

The measurement points were compiled in the same way as in Figure 4-11. There was nearly a linear relation between downstream distance and static pressure until the test stand. Behind the test stand, there was a pressure recovery due to flow deceleration and disturbances from the test stand. This linear drop in pressure downstream towards the test stand could be used to

establish the proper static pressure for the tunnel reference that should be a differential pressure of -45 Pa compared to Pitot 1.

4.5 Test stand

To investigate the uniformity of the flow at the airfoil section, the flow at the test stand was measured in the cross-flow plane, *yz*-plane, in the downstream direction at the airfoil section position in the test stand, $x = 0$.

Velocity profile

Figure 4-14 shows the horizontal velocity profiles at different heights, measured without the airfoil section mounted. The position of the airfoil section corresponded to, $z = 0$. The velocity near to the floor at $z = -0.25$ was strongly accelerated due to the presence of the test stand, which has a horizontal spar on the floor with a height of about 0.30 m. The velocity at the airfoil section height was more moderately accelerated. At $z = 0.25$, the speed up was again increased, as it was found in Section 4.3.

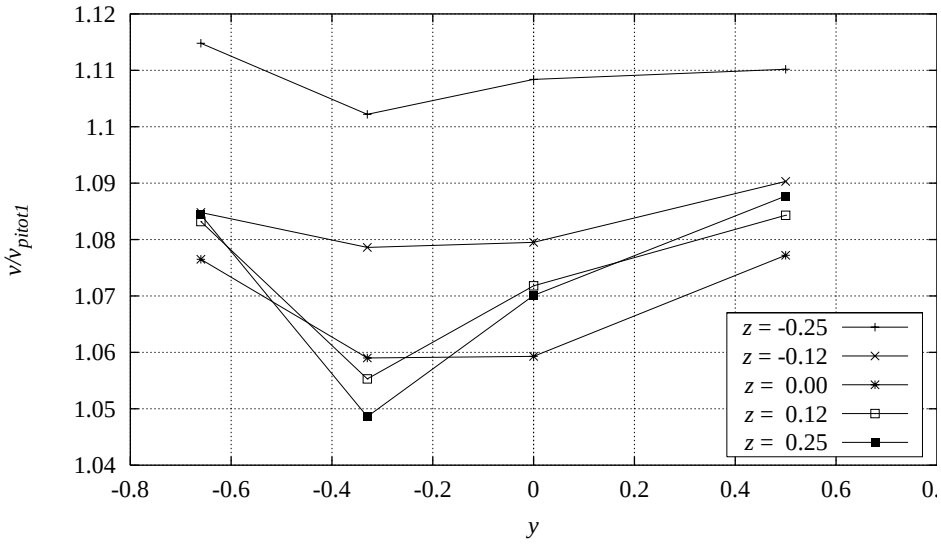

Figure 4-14 Horizontal velocity profiles at different heights at the airfoil position, (x = 0), with no airfoil section mounted.

Above $z = 0$, the velocity profile was asymmetric. At negative *y*-values, there was a drop in velocity at $y = -0.30$ m. This was in contrast to the jet inlet, where the velocity was increased to this side, and apparently the flow was developed differently at both sides of the tunnel. This was not significant except for the flow above the airfoil section, which was of less interest for the tunnel flow reference estimation.

Figure 4-15 shows the 3d velocity profile, based on Figure 4-14. The large variation towards the floor appeared consistent for the different measurements, as well as the more moderate speed up at the airfoil section center both in the vertical and the horizontal direction.

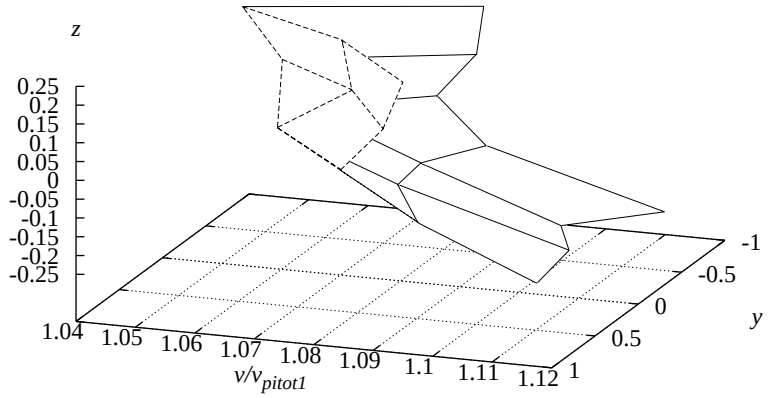

Figure 4-15 3d velocity profile at the airfoil position (x = 0), with no airfoil section mounted.

Static pressure

The variation in static pressure corresponding to Figure 4-14 is shown in Figure 4-16. For all measurement heights there was a horizontal variation. The static pressure towards negative *y*-values was lower than the static pressure at positive *y*-values.

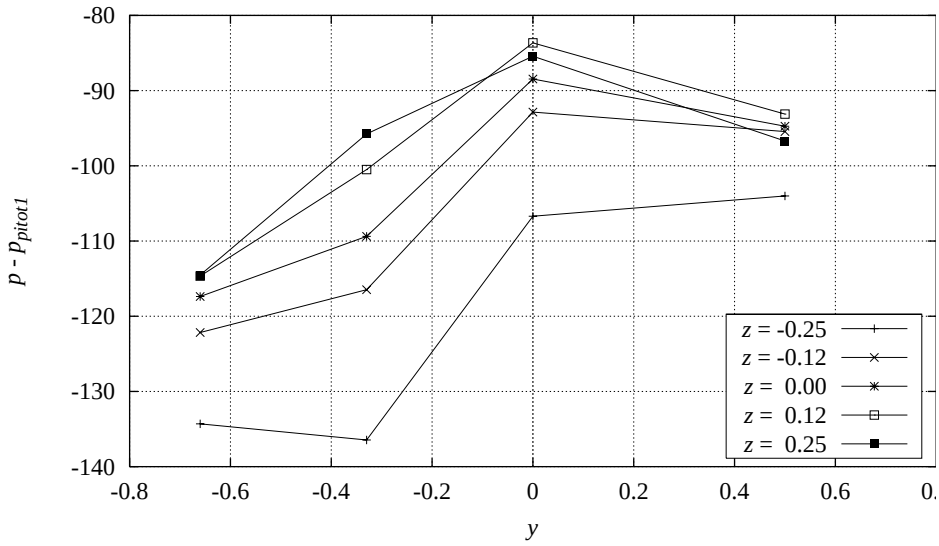

Figure 4-16 Horizontal variation of static pressure at different heights at the airfoil position, (x = 0), with no airfoil section mounted.

4.6 Wake rake

To calculate the total drag coefficient and to investigate the uniformity of the flow field at the wake rake, possible disturbances from the test stand and the blocking from the airfoil section wake rake measurements were taken with and without the airfoil section.

Velocity profile

Figure 4-17 shows two measurements of the wake rake velocity profile at different temperatures. The measurements were taken without the airfoil section mounted in the test stand.

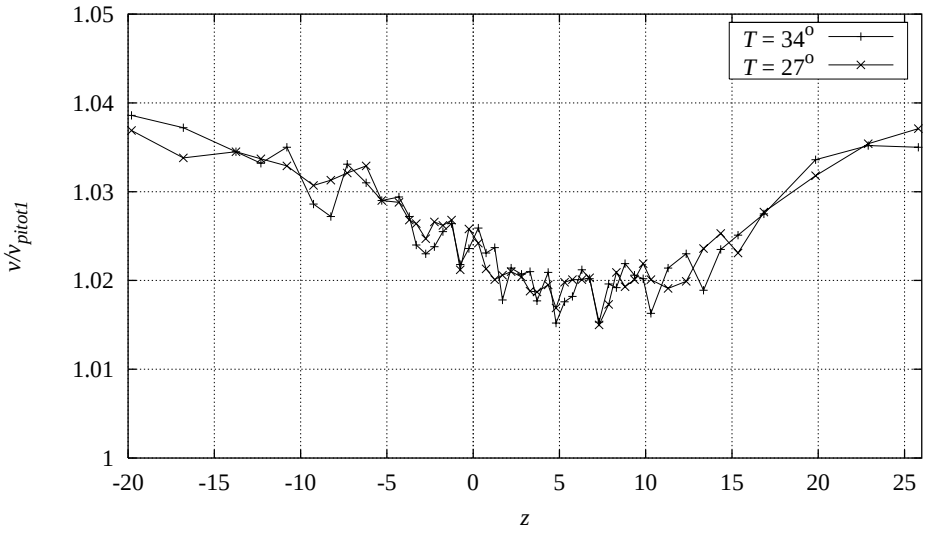

Figure 4-17 Vertical velocity profiles at the wake rake, with no airfoil section mounted.

Earlier sections showed a coarse picture of the vertical velocity variation at the tunnel centerline. This picture was reproduced with higher resolution by the wake rake. The velocity was minimum at the airfoil section height, $z = 0$, and increased toward both floor and ceiling. The increase towards the floor was due to the acceleration from the presence of the test stand and the floor, whereas the increase toward the ceiling was also found in Section 4.3 and Section 4.4 and was due to the variation in the jet inlet velocity profile.

There was some scatter in the measurements and a minor variation existed for the same points of the two measurement series. Since the shape of the velocity profile was confirmed by several other measurements, the overall shape of the velocity profile was not a result of the wake rake geometry. However, disturbances from blocking from the individual tubes could not be excluded.

Static pressure

The static pressures at the wake rake for two measurements with different tunnel temperatures are shown in Figure 4-18. Except for the measurement point nearest to the floor, the agreement was good. The pressure drops towards the ceiling, however the total pressure variation was small.

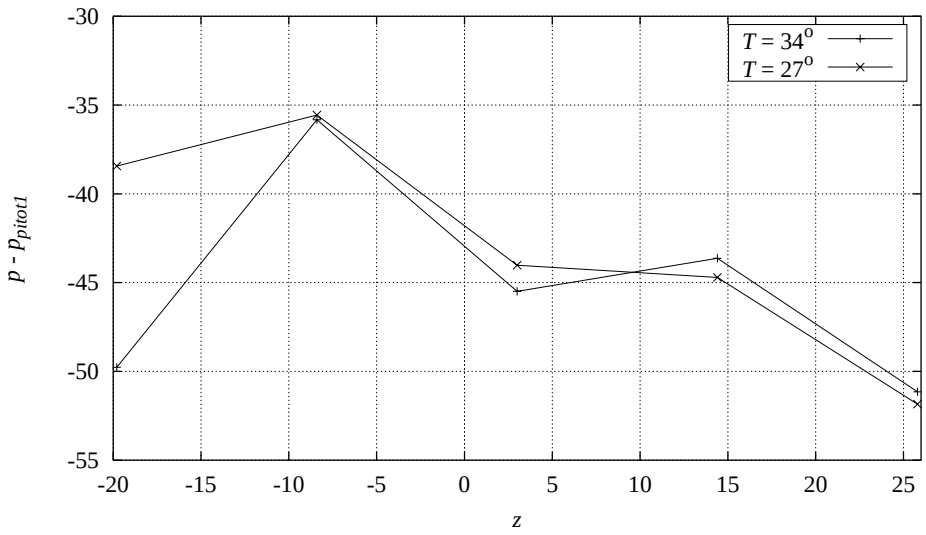

Figure 4-18 Vertical variations in static pressure at the wake rake, with no airfoil section mounted.

Angle of attack dependency

The velocity profile in the absence of the airfoil section should be used to determine the undisturbed velocity profile that is necessary for the momentum balance and the drag calculation. The variation of the wake rake velocity profile with the angle of attack of the airfoil section is therefore very important to the calculation of total airfoil drag. From an ideal point of view, the velocity profile outside of the airfoil wake should not depend on the angle of attack. However, the interaction between the airfoil section, the test stand and the endplates caused a variation in the velocity at the wake rake regions outside of the airfoil wake, Figure 4-19.

Figure 4-19 shows the wake rake velocity profile without an airfoil section mounted and with the airfoil section at different angles of attack. When the angle of attack was increased, the airfoil wake was shifted towards negative *z*. The wake was partially outside of the wake rake span at 15° and calculation of total drag was no longer possible. However, here, the flow was partially separated and unsteady and the wake rake could no longer be used.

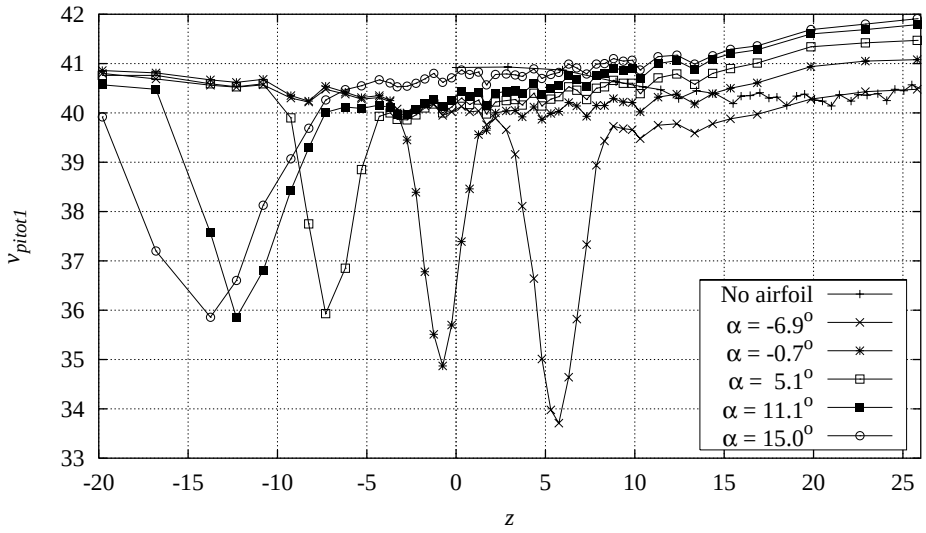

Figure 4-19 Vertical velocity profiles for the wake rake without airfoil and with an airfoil at different angles of attack (NA63215STEP221196V1).

From Figure 4-17 and Figure 4-19 it can be seen that the velocity profile measured by the wake rake without the airfoil section mounted was not flat and uniform as expected. Instead it shows a deficit in the middle relative to the end rake values which were on both sides at approximately the same level. This deficit had to be taken into account in the calculation of total drag.

Another observation from Figure 4-19 is that in the presence of an airfoil section and depending on the angle of attack the measured pressures by the end tubes of the rake, varied more relative to the values without the airfoil section. This variation was larger at the upper part of the wake rake relative to the lower one. The acceleration of the flow at the upper part occurred due to the fact that at positive angles of attack the streamlines become denser.

It was not possible to use the measured undisturbed wake rake velocity profile directly for the calculation of total drag because of the non-uniform variation of the velocity profile with both height and angle of attack.

For the angles where the wake was within the rake, the following procedure was instead used for the calculation of the total drag:

1. The end points of the airfoil wake region at the wake rake were determined.
2. The velocities of the undisturbed part of the wake rake were used to construct an undisturbed velocity profile where the airfoil wake region was replaced by a straight line.
3. The velocity deficit was estimated from the difference in velocity between the wake region velocities and the constructed undisturbed velocities.
4. The total drag was calculated from the loss in momentum, see Chapter 5.

The method is illustrated in Figure 4-20, where the wake deficit for the NACA 63-215 airfoil is shown at $\alpha = 9.4°$ together with the constructed undisturbed velocity profile. The airfoil wake is contained in the interval from $z = -12$ to $z = -3$.

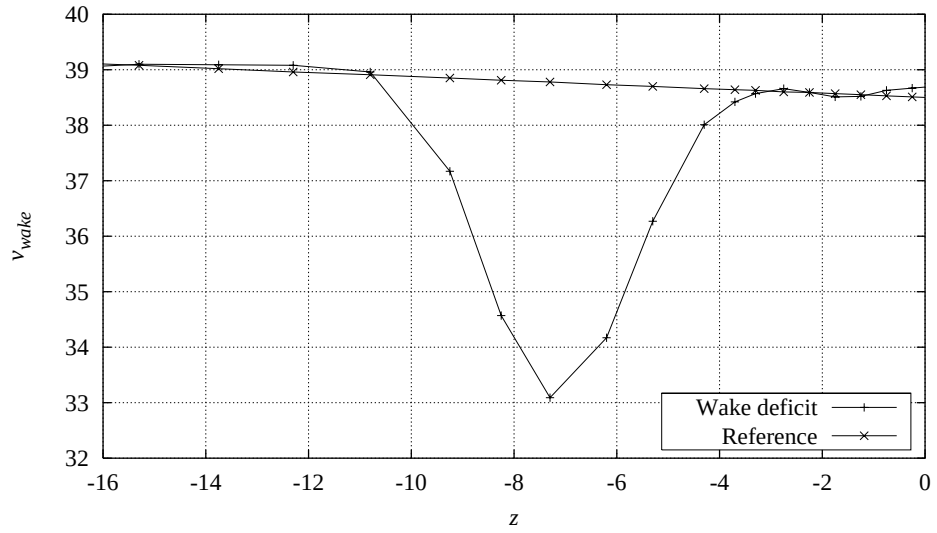

Figure 4-20 Illustration of the calculation of total drag from the wake rake measurement. The undisturbed velocity profile in the wake rake region is assumed to be a straight line, $\alpha = 9.4°$.

4.7 Wind tunnel reference

Based on the different measurements reference values for velocity and static pressure were found from the pitot tubes 1-3.

The corrections on the velocity and static pressure to obtain the proper values for the airfoil section are shown in Table 4-2. Comparison of the stability of Pitot 1-3 showed that Pitot 3 was nearly independent on temperature and time from calibration. This was also the case for Pitot 1 and 2, if measurements with large temperature increases or long measurement time were discarded. Hence, it could be concluded that all Pitot tubes could be used as reference for normalization of the aerodynamic loads and Pitot 1 was chosen on this background.

Table 4-2 The percentage difference in velocity and the pressure difference for Pitot 1, 2 and 3 velocity and static pressure for use at correction of the Pitot measurements to the wind tunnel reference.

	Velocity speed up factor, ε_{pitot} **(%)**	**Static pressure differential,** $\Delta p_{stat,dif}$ **(Pa)**
Pitot 1	1.059	-45
Pitot 2	1.046	-13
Pitot 3	0.0065%	+31

5 Calculation methods

This chapter presents the methods used to obtain velocities and pressures from raw data. Furthermore the calculation of the airfoil pressure distribution and lift-, C_L, pressure drag-, C_{Dp}, and moment-, C_M, coefficients from the pressure distribution is explained together with the calculation of total drag, C_{Dw}, from the wake rake measurements.

5.1 Density, pressures and velocity

The air density, ρ, is calculated from:

$$\rho = 1.225\left(\frac{288.15}{t+273.15}\right)\left(\frac{p_{atm}}{1013.3}\right) \qquad (5\text{-}1)$$

Where t [°c] is the tunnel temperature and p_{atm} [mBar] is the atmospheric pressure

Pitot tube velocities, v_{Pitot}, are calculated from:

$$v_{pitot} = 1.28\left(\sqrt{\left(p_{tot,pitot} - p_{stat,pitot}\right)\left(\frac{1013.3}{p_{atm}}\right)\left(\frac{t+273.15}{288.15}\right)}\right) \qquad (5\text{-}2)$$

Where $p_{tot,Pitot}$ [Pa] is the Pitot tube total pressure, $p_{stat,Pitot}$ [Pa] is the Pitot tube static pressure.

The tunnel reference dynamic pressure, $q_{\infty,ref}$, and static pressure, $p_{stat,ref}$, corresponding to the undisturbed free stream dynamic and static pressures at the test stand are found on basis of known correlation with a Pitot tube static and dynamic pressure, Table 4-2, Section 4.7. All three pitot tubes can be used and Pitot 1was chosen. It is located near the nozzle outlet upstream of the test section where it is not influenced by the airfoil section.

$q_{\infty,ref}$ is found from the determined speed up factor, ε_{Pitot}, between the Pitot tube and the test stand location of the airfoil section:

$$q_{\infty,ref} = \tfrac{1}{2}\rho\left(v_{pitot}\left(1+\varepsilon_{pitot}\right)\right)^2 \qquad (5\text{-}3)$$

$p_{stat,ref}$ is found from the determined static pressure differential, $\Delta p_{stat,dif}$, between the Pitot tube and the location of the airfoil section:

$$p_{stat,ref} = p_{stat,pitot} + \Delta p_{stat,dif} \qquad (5\text{-}4)$$

ε_{Pitot} and $\Delta p_{stat,dif}$ were determined in Section 4.7, Table 4-2.

5.2 Airfoil forces from pressure distribution

The airfoil pressure coefficient, $C_p(s)$, along the airfoil surface, s, is calculated from the relation:

$$C_p(s) = \frac{p(s) - p_{stat,ref}}{q_{\infty,ref}} \qquad (2\text{-}1)$$

Where $p(s)$ is the airfoil surface pressure measured around the airfoil section.

The normal force coefficient, C_N, and the tangential force coefficient, C_T, are found from integration of the surface pressure distribution. The total force is resolved in the normal and tangential to the chord directions respectively:

(2-2)

$$C_N = \frac{N}{q_{\infty,ref}\, c} = \frac{1}{c}\oint C_p(s)\vec{t}\cdot d\vec{s}$$

$$C_T = \frac{T}{q_{\infty,ref}\, c} = \frac{1}{c}\oint C_p(s)\vec{n}\cdot d\vec{s}$$

Where N is the total normal force per unit length, T is the total tangential force per unit length, $\vec{t}$ is a unit vector aligned to the chord, $\vec{n}$ is a unit vector perpendicular to the chord, $d\vec{s}$ is running along the airfoil surface, Figure 2-1.

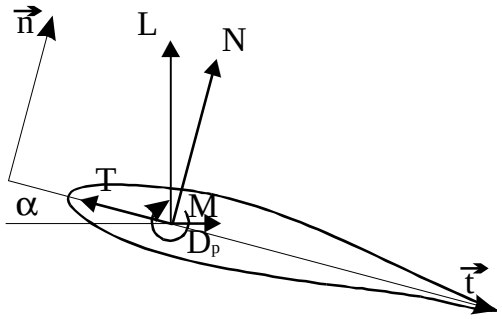

Figure 2-1 Sign convention for airfoil forces and unit vectors for the integration of airfoil pressure.

The airfoil lift per unit length, L, and pressure drag per unit length, D_p are found by resolving N and T normal and tangential to the oncoming flow respectively by use of the angle of attack, a:

$$L = \cos(a)N + \sin(a)T$$

(2-3)

$$D_p = -\cos(a)T + \sin(a)N$$

The lift coefficient, C_L, and pressure drag coefficient, C_{Dp}, are calculated:

$$C_L = \frac{L}{q_{\infty,ref}\, c} \qquad (2\text{-}4)$$

$$C_{Dp} = \frac{D_p}{q_{\infty,ref}\, c}$$

The airfoil moment coefficient, C_M, is found from integration of the contributions from normal and tangential pressure components:

$$C_M = \frac{M}{q_{\infty,ref}\, c^2} = \frac{1}{c^2}\left[\oint (\vec{r}\cdot\vec{t})(C_P(s)\vec{t}\cdot d\vec{s}) + \oint (\vec{r}\cdot\vec{n})(C_P(s)\vec{n}\cdot d\vec{s})\right] \qquad (2\text{-}5)$$

Where $\vec{r}$ is a vector from the point of moment to the vector along the airfoil surface.

5.3 Airfoil drag from wake rake

The airfoil total drag is the sum of contributions from skin friction and pressure drag. Since only pressure drag can be calculated from the airfoil pressure distribution, the total drag is calculated from a momentum balance between the momentum in the flow ahead of the airfoil section with the momentum in the flow behind the airfoil section. It is then assumed that the flow is 2d.

The total wake drag coefficient, C_{Dw}, is calculated from [7]:

$$C_{Dw} = \frac{2}{c}\int \sqrt{\frac{p_{tot}(y) - p_{stat}(y)}{q_{\infty,ref}}} \cdot \left(1 - \sqrt{\frac{p_{tot}(y) - p_{stat}(y)}{q_{\infty,ref}}}\right) dy \qquad (2\text{-}6)$$

Where $P_{tot}(y)$ is wake rake total pressure, $p_{stat}(y)$ is wake rake static pressure.

6 Results

This chapter reports results from measurements on the NACA 63-215 airfoil. The different measurement runs are described in more detail in Appendix A1. All shown results have been corrected for wind tunnel effects (Chapter 3) and are referenced to the wind tunnel Pitot 1 reference established in Chapter 4.

First, detailed pressure distributions are presented. Next polar curves are shown for C_L, C_D and C_M. Measurements are shown for leading edge roughness flow. Dynamic measurements are shown for the airfoil in pitching motion. Finally measurements at high angles of attack are investigated for multiple C_L levels at constant angle of attack, the so-called 'double stall' phenomenon.

Five different types of measurements are used:

1. Measurements at different angles of attack with 20 s time series at each angle. Angle of attack range from -6° to 30° with discrete steps of 2°. Sample frequency 5 Hz. See Appendix A1.1, measurement type, 'STEP'.
2. Measurements at different angles of attack with continuous change of angle of attack around 0.1 - 0.5 °/s. Angle of attack range from -6° to 30°. Sample frequency 50 Hz. See Appendix A1.1, measurement type 'CONT'.
3. Measurements at different angles of attack with time series length 180s at each angle. Angles of attack in light and deep stall. Sample frequency 100 Hz. See Appendix A1.1, measurement type 'STAT'.
4. Dynamic measurements with the airfoil section in pitching motion around different mean angles of attack with amplitudes between 2° and 3° and different reduced frequencies. Time series length 30s to 40s. Sample frequency 100 Hz. See Appendix A1.1, measurement type 'PITCH'.
5. As measurement 2, 'CONT', with the use of sand paper at the leading edge to simulate surface roughness.

The measurements were compared to measurements from FFA carried out on exactly the same airfoil section model at $Re = 1.7\times10^6$ in a closed wall wind tunnel [4] and NACA measurements at $Re = 3.0\times10^6$ from [1].

The measurements were also compared to calculations. The XFOIL code based on a panel method with a viscous boundary layer formulation was used with free transition modeling and in cases with leading edge roughness with transition fixed to the leading edge [16]. The EllipSys2D Navier-Stokes code was used for turbulent flow calculations with the k-ω turbulence model without transition prediction [12].

6.1 Pressure distributions

Figure 6.1 shows the measured C_P curves for different angles of attack. Each C_P curve was based on average values for a 20s time series. When the angle of attack was increased, the suction peak was gradually build up until angles of attack around

16^{o}. At higher angles of attack, the airfoil stalled and separation removed the suction peak and the suction side pressure became nearly uniform.

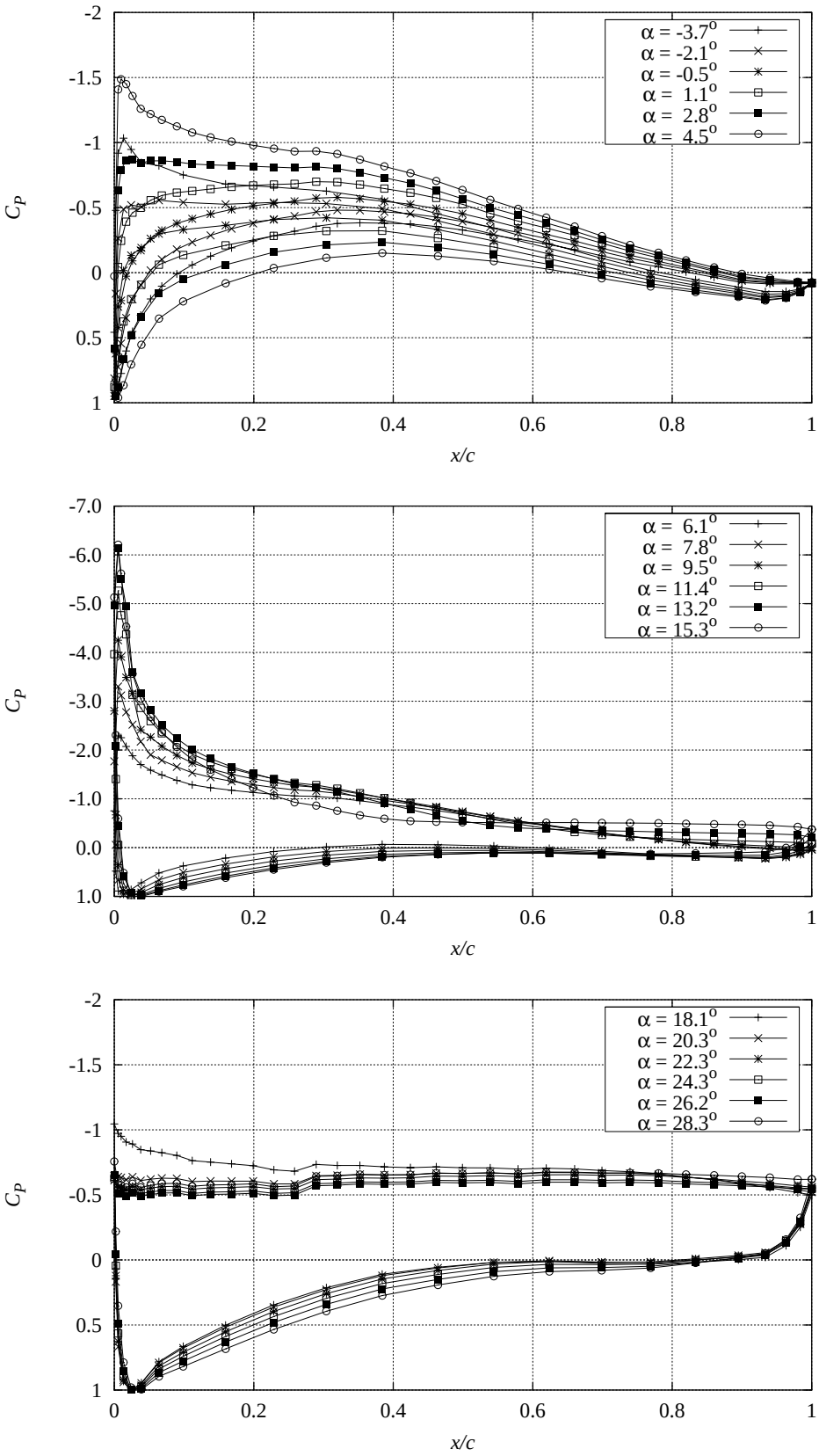

Figure 6-1 Measured C_P curves at different angles of attack (NA63215STEP290296V1).

Figure 6-2 shows a C_P curve at $\alpha = 7.8°$ with minimum and maximum values for a 20s time series. The standard deviation was small on the pressure side and slightly increased at the suction peak.

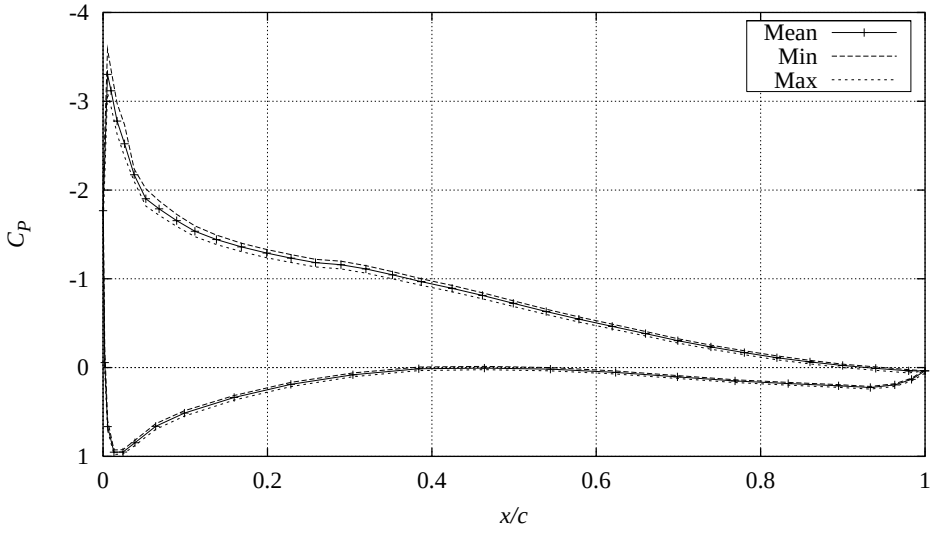

Figure 6-2 Measured C_P curve with minimum and maximum values, NACA 63-215, Re = 1.3×10^6, $\alpha = 7.8°$, (NA63215STEP290296V1).

Figure 6-3 shows the measured C_P curve at $\alpha = 7.8^o$ compared to an EllipSys2D turbulent flow calculation and an XFOIL free transition calculation. The agreement with both computations was good. The suction peak was well captured in the measurement and the stagnation pressure was located at the same position. Near the trailing edge there was a small discrepancy with lower pressures for the measurement compared to the calculations. This was caused by the deviation in the tested model compared to the theoretical coordinates, Section 2.3. This deviation will however not influence the calculation of aerodynamic loads.

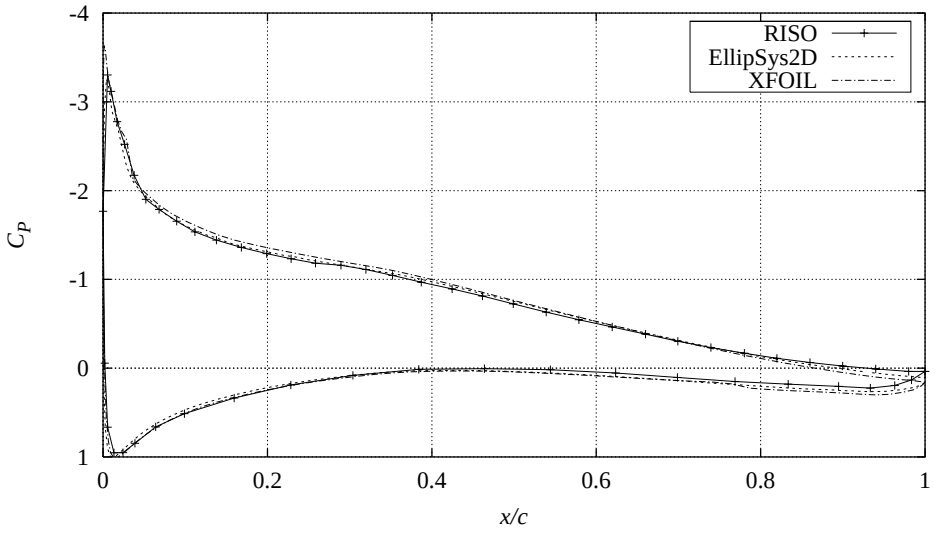

Figure 6-3 Measured C_P curve compared to EllipSys2D (turbulent flow) and XFOIL free transition calculations, NACA 63-215, Re = 1.3×10^6, $\alpha = 7.8^o$, (NA63215STEP290296V1).

The measured C_P curve $\alpha = 6.1^o$ is compared to a FFA measurement [4] and an XFOIL free transition calculation in Figure 6-4. The suction peak and the stagnation point were in good agreement. The shape of the C_P curve was in general captured quite well and the deviations were minor. At the trailing edge however, the XFOIL calculation resulted in higher pressures compared to the measurements as in Figure 6-3.

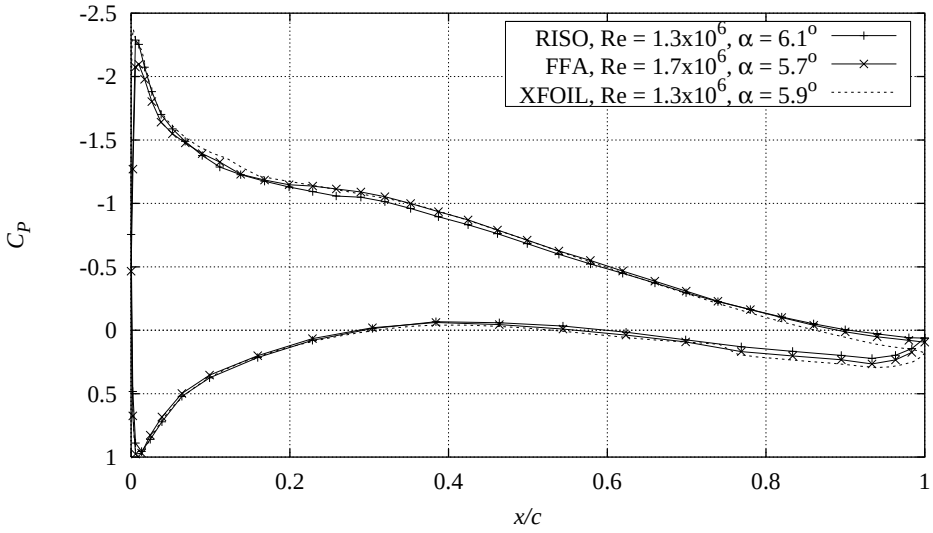

Figure 6-4 Measured C_P curve, Re = 1.3×10^6, at $\alpha = 6.1^o$ compared to FFA measurement, Re = 1.7×10^6, at $\alpha = 5.7^o$ [4] and XFOIL free transition calculation, Re = 1.3×10^6, at $\alpha = 5.9^o$ (NA63215STEP290296V1).

A corresponding comparison at $\alpha = 11.4^o$ shows the same tendencies, Figure 6-5, although the suction peak is overestimated by XFOIL. The FFA and the Risø measurements were in good agreement, whereas the XFOIL calculation showed higher pressures at the trailing edge.

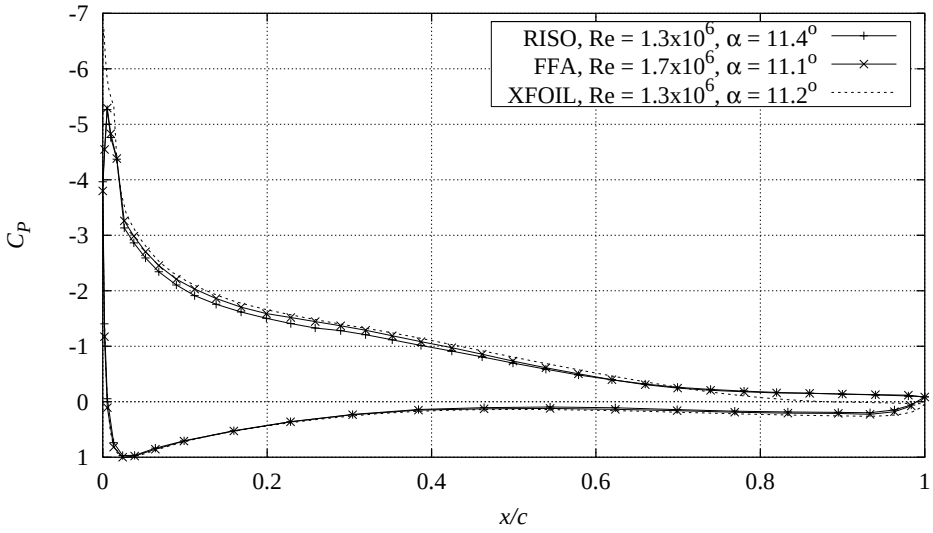

Figure 6-5 Measured C_P curve, Re = 1.3×10^6, at $\alpha = 11.4^o$ compared to FFA measurement, Re = 1.7×10^6, at $\alpha = 11.1^o$ [4] and XFOIL free transition calculation, Re = 1.3×10^6, at $\alpha = 11.2^o$ (NA63215STEP290296V1).

Figure 6-6 shows the measured C_P curve at $\alpha = 15.3^o$ compared to an FFA measurement and an XFOIL free transition calculation. The stagnation points were located similar and the pressure sides were in good agreement. On the suction side, separation has started from the trailing edge. On the trailing edge part, the agreement between the FFA and Risø measurements was good. The degree of separation was higher for the Risø measurement, compared with FFA. This could be caused by the higher turbulence intensity in the Risø measurement that would advance transition and separation.

Since the blocking effects are higher in the FFA closed wall tunnel and taking into consideration the difference in Reynolds number, it is possible that the acceleration of the flow reduced relatively the occurrence of separation in the FFA measurement compared to the Risø measurement.

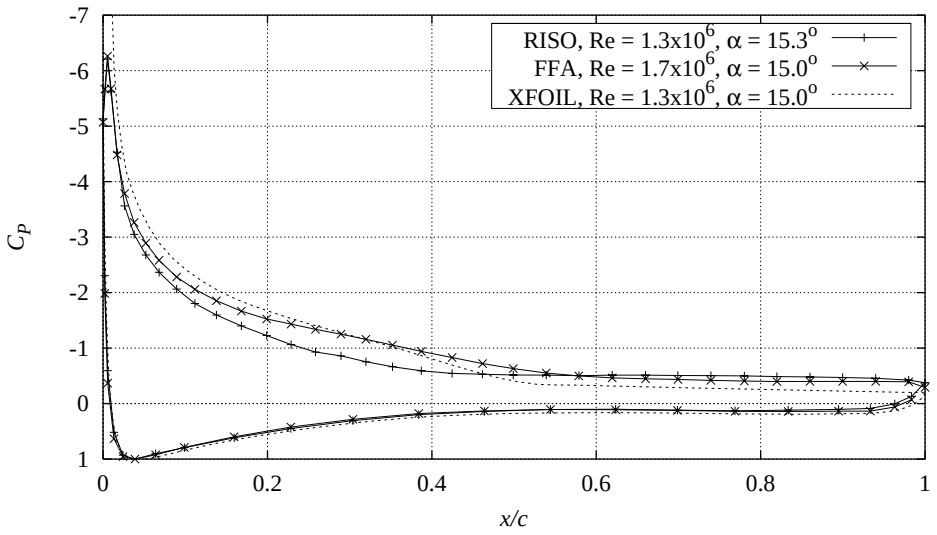

Figure 6-6 Measured C_P curve, Re = 1.3×10^6, at $\alpha = 15.3^o$ compared to FFA measurement, Re = 1.7×10^6, at $\alpha = 15.0^o$ [4] and XFOIL free transition calculation, Re = 1.3×10^6, at $\alpha = 15.0^o$ (NA63215STEP290296V1).

Figure 6-7 shows measured C_P at $\alpha = 18.1^o$ compared to FFA measurements. The agreement on the pressure side was fair, whereas the suction sides differed towards the trailing edge. The highly unsteady flow at this angle was clearly different in the two wind tunnels and the measured results were not comparable for high angles of attack.

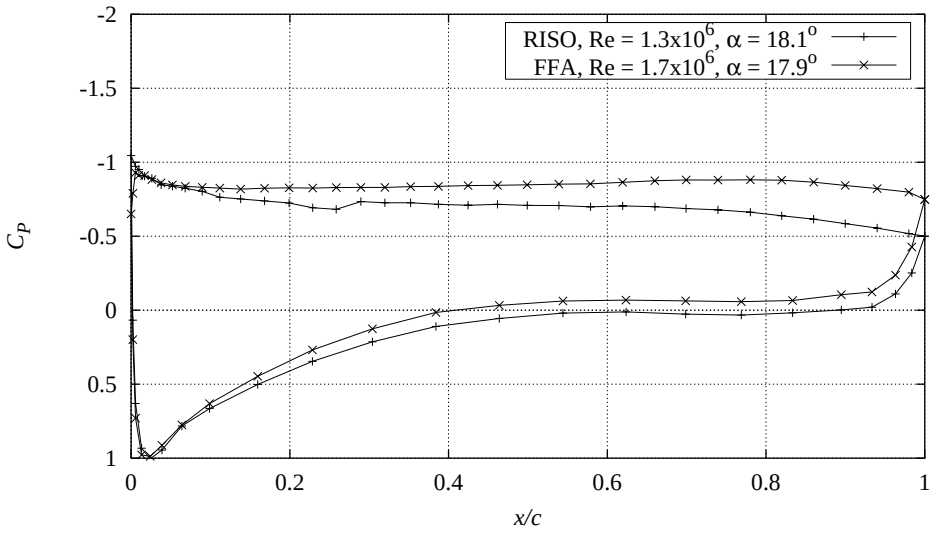

Figure 6-7 Measured C_P curve, Re = 1.3×10^6, at α = 18.1^o compared to FFA measurements, Re = 1.7×10^6, at α = 17.9^o [4] (NA63215STEP290296V1).

6.2 Polar results

This section presents the aerodynamic loads on the airfoil section that are calculated from the airfoil pressure and wake rake measurements. Wind tunnel boundary corrections were applied to all reported results.

Lift coefficient

The measured C_L curve with minimum and maximum values is shown in Figure 6-8. Each measurement points represents a 20s time series, sampled with 5 Hz. The standard deviation was in general very low except for the post stall region, where the flow was highly unsteady and 3d.

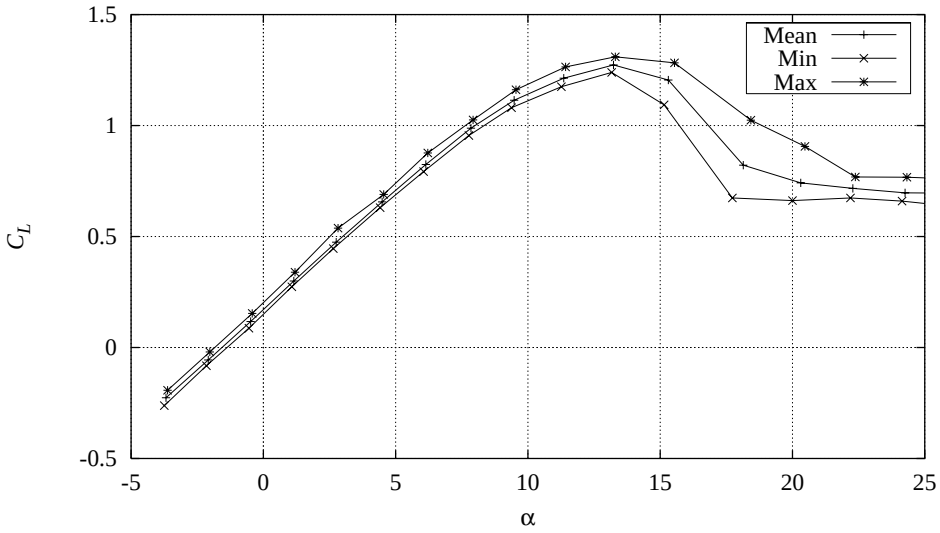

Figure 6-8 Measured C_L curve with minimum and maximum values for a 20 s time series (NA63215STEP290296V1).

The measured C_L curve is shown in Figure 6-9 compared to an XFOIL free transition calculation and an EllipSys2D turbulent flow calculation, both at $Re = 1.3\times10^6$.

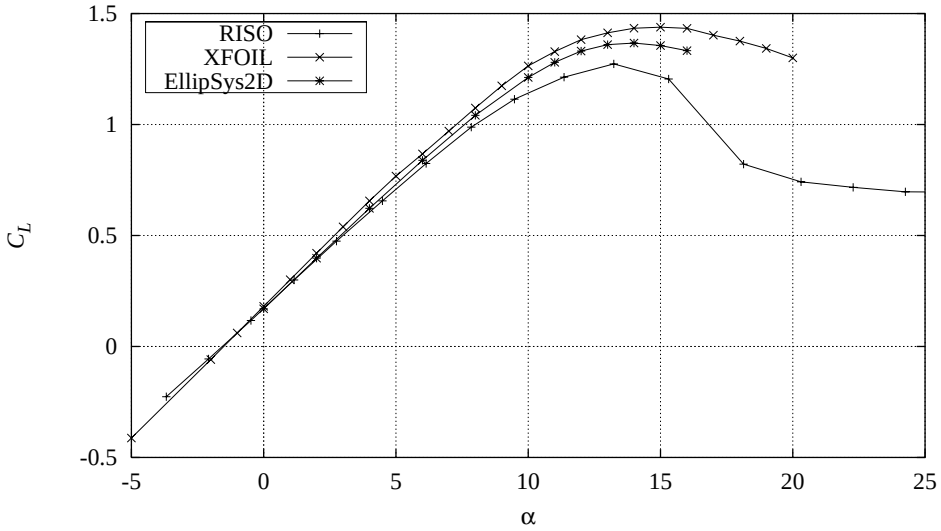

Figure 6-9 Measured C_L curve compared to XFOIL free transition calculation and EllipSys2D turbulent flow calculation at $Re = 1.3\times10^6$ (NA63215STEP290296V1).

There was in general good agreement. At low angles of attack, the three curves were nearly identical. The slope of the measured curve was slightly lower compared to the calculated curves. This was probably because the corrections for streamline curvature and down-wash were too small. The influence of down-wash through the clearance between the airfoil section and the endplates could be underestimated or the streamline curvature might not be perfectly comparable to the cascade flow that forms the basis for the applied correction. However, the agreement was satisfactory.

At higher angles of attack, the measured C_L curve did not agree well with the calculation. C_{Lmax} was measured too low and C_L was measured too low in the post stall region. This is however often seen when measurements are compared to calculations. Especially XFOIL calculations tend to show too high C_{Lmax} together with too steep C_L curve slope [16].

Figure 6-10 shows the measured C_L curve from Figure 6-9 compared to measurements from FFA [4] carried out on exactly the same airfoil section at $Re = 1.7\times10^6$ in a closed wall wind tunnel and NACA measurements from [1] at $Re = 3.0\times10^6$. The C_L curve slopes at low angles of attack were in good agreement. The NACA measurement was slightly offset to a different angle of zero lift. The slope of the FFA measurement was steeper than the Risø measurement. The agreement between Risø and FFA measurements was good until 15° and at C_{Lmax}. However, the post stall area was very different for the two measurements probably because of different 3d behavior of the wind tunnel types that were used.

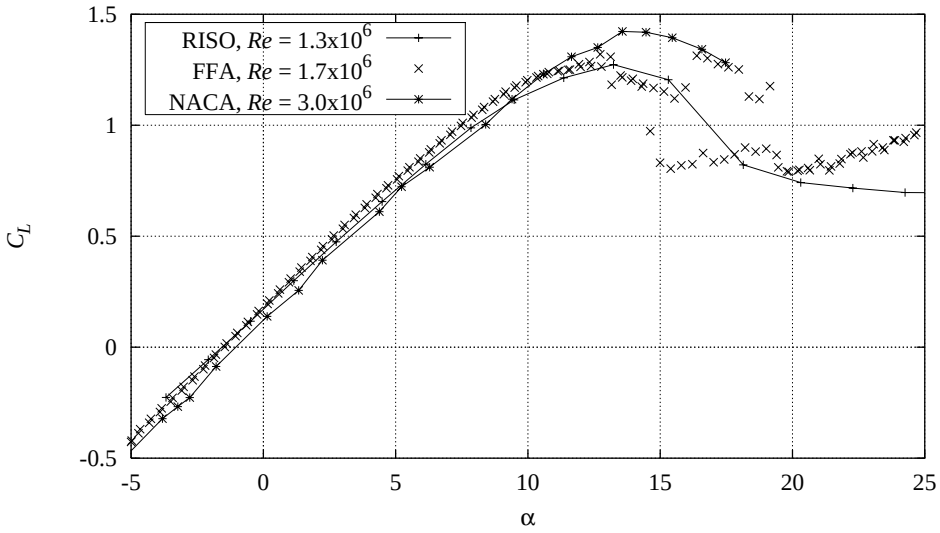

Figure 6-10 Measured C_L curve at Re = 1.3×10^6, compared to FFA measurements, Re = 1.7×10^6 [4] and NACA measurements, Re = 3.0×10^6 [1] (NA63215STEP290296V1).

The established wind tunnel reference and the applied wind tunnel boundary corrections turned out to give good results. Even though the FFA measurements appears to be even closer to the calculations, the agreement between Risø and FFA measurements was good, having in mind the uncertainties introduced by the open jet flow.

Drag coefficient

The measured C_D curves with mean, minimum and maximum values are shown in Figure 6-11, based on 20s time series, sampled with 5 Hz, at each angle of attack. At angles of attack below app. 13°, the drag was calculated from the wake rake. At higher angles of attack, when the drag from the pressure distribution increased because of separation, the drag was taken simply as the drag from the pressure distribution.

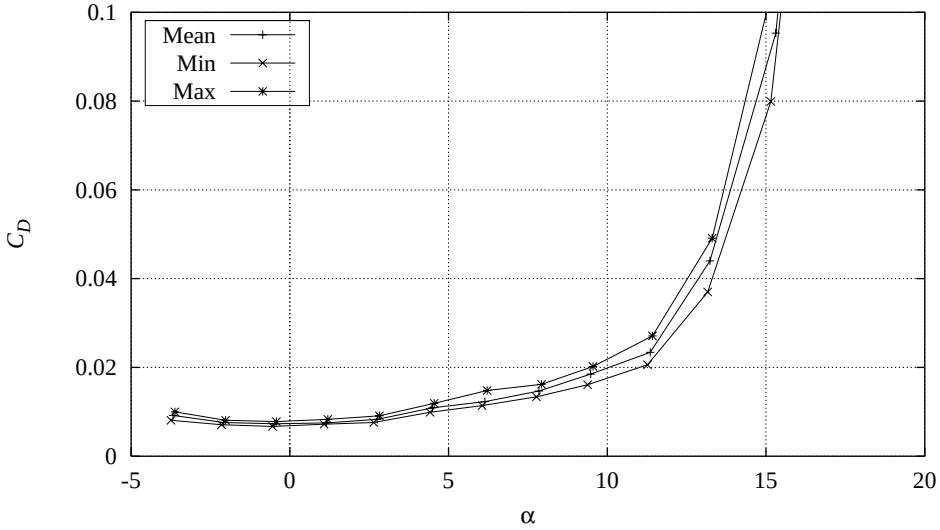

Figure 6-11 Measured C_D curve, Re = 1.3×10^6, with minimum and maximum values for 20s time series (NA63215STEP290296V1).

Compared to the C_L, C_D is more complex to determine with high accuracy because of the calibration of the wake rake and the disturbances from the endplates downstream of the airfoil section. Compared to the value of C_D, the standard deviation appears to be quite high.

The measured C_D curve is compared with XFOIL free transition calculations and EllipSys2D turbulent flow calculations in Figure 6-12. The shape of the C_D curve was captured well in the measurement compared to the XFOIL calculation. Around 5° there is a small jump in drag, which is also predicted by XFOIL at 6°. Normally, XFOIL predicts drag very well at low angles of attack [16]. However XFOIL maintains attached flow until a higher angle of attack and hence underestimates drag at higher angles of attack. This explains the discrepancy between measurements and XFOIL calculations at higher angles of attack. The higher skin friction from a fully turbulent boundary layer flow caused the rather high drag at low angles of attack predicted by EllipSys2D compared to measurements. EllipSys2D predicts the increase in drag after separation well compared to XFOIL.

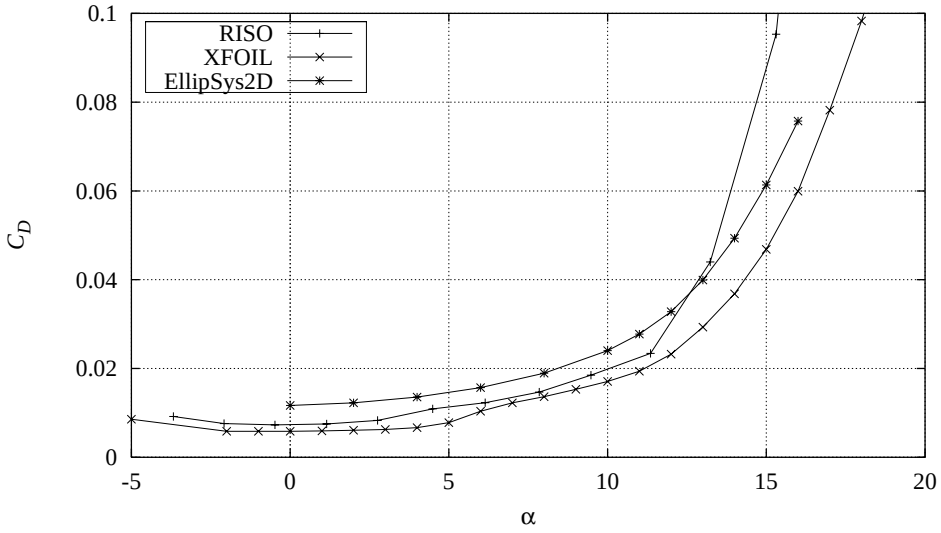

Figure 6-12 Measured C_D curve compared to XFOIL free transition calculation and EllipSys2D turbulent flow calculation at Re = 1.3×10^6, (NA63215STEP290296V1).

Figure 6-13 shows the measured C_D curve from Figure 6-12 compared to the FFA measurement [4] and the NACA measurement [1]. While the tendency of C_D was well captured, the measured C_D was slightly higher in absolute values compared to the NACA and FFA measurements. This offset was probably due to the higher turbulence in the tunnel, see chapter 4.

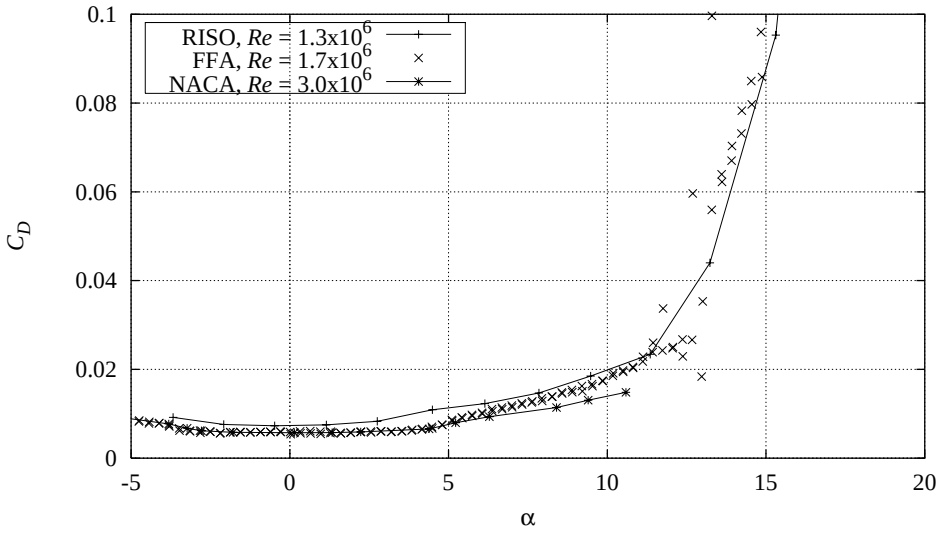

Figure 6-13 Measured C_D curve, Re = 1.3×10^6, compared to FFA measurements, Re = 1.3×10^6, [4] and NACA measurements, Re = 1.3×10^6, [1] (NA63215STEP290296V1).

Moment coefficient

The measured C_M curves with mean, minimum and maximum values are shown in Figure 6-14. Each measurement point was based on a 20 s time series, sampled with 5 Hz. The standard deviation was very low at low angles of attack whereas it increased significantly in the post stall area.

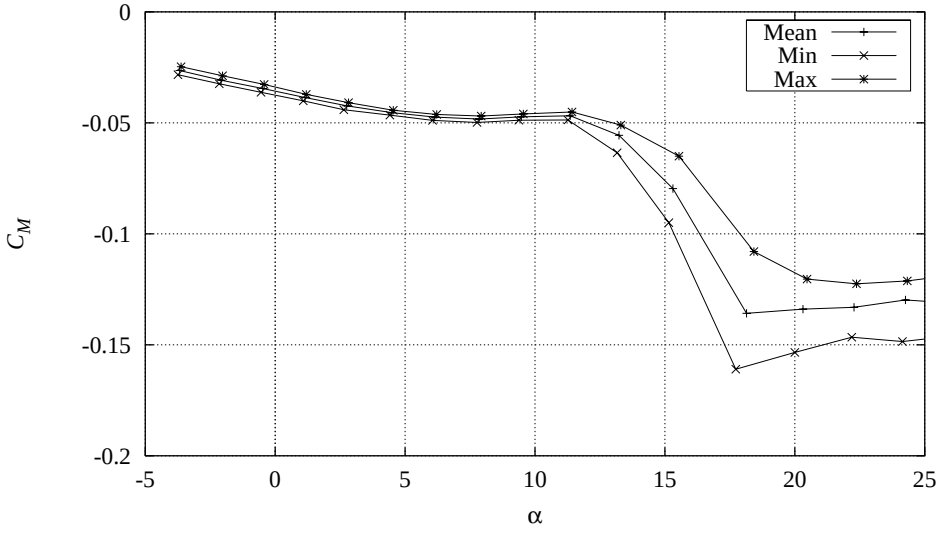

Figure 6-14 Measured C_M curve, Re = 1.3×10^6, with minimum and maximum values for 20s time series (NA63215STEP290296V1).

The measured C_M curve is shown in Figure 6-15 compared to the FFA measurement [4], NACA measurement [1] and an XFOIL free transition calculation. The Risø measurements were in good agreement with the NACA measurements and at low angles of attack the agreement was in general good. The FFA measurements compared well to the XFOIL calculations. The

deviations between the Risø measurement and the FFA measurement were due different influence from the wind tunnel.

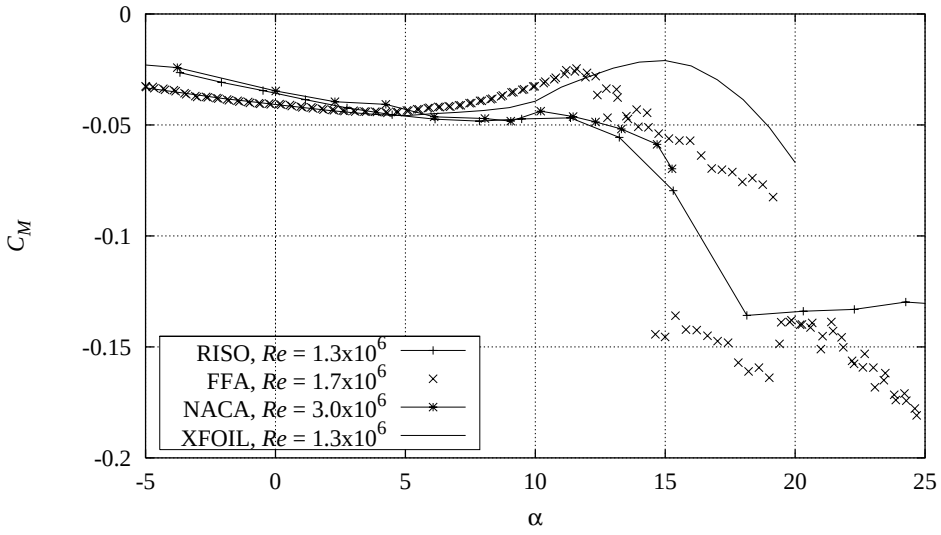

Figure 6-15 Measured C_M curve, Re = 1.3×10^6, compared to FFA measurements, Re = 1.7×10^6, [4], NACA measurements, Re = 3.0×10^6, [1] and XFOIL free transition calculation, Re = 1.3×10^6, (NA63215STEP290296V1).

6.3 Leading edge roughness

In natural conditions, bugs and dirt often soil wind turbine blades. The sensitivity of the wind turbine power production to this is important. By applying leading edge roughness (LER) to the airfoil section leading edge, soil depositing can be simulated to investigate the airfoil performance under this condition. The applied leading edge roughness was described in Section 2.6.

Pressure distributions

Figure 6-16 shows measured C_P at $\alpha = 11.0^o$ for leading edge roughness compared to smooth flow. Whereas the pressure side was nearly unaffected by LER, the suction side pressure distribution was different compared with the corresponding smooth flow condition. The suction side pressure at the leading edge part was higher resulting in lower C_L. The presence of LER influenced the velocity distribution close to the airfoil surface where velocity was reduced and the degree of separation was higher in the rough case. Following the velocity reduction, the suction peak was also reduced.

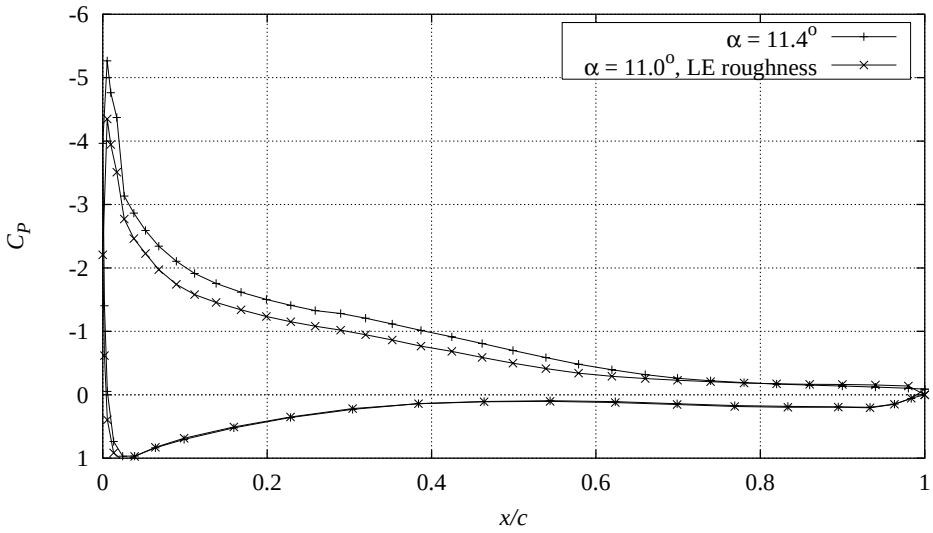

Figure 6-16 Measured C_P curve, Re = 1.3×10^6, at α = 11.4° compared to measured C_P curve at α = 11.0° with leading edge roughness (LE roughness) (NA63215STEP290296V1 and NA63215CONTV2S2).

Polar results

Figure 6-17 shows measured C_L curves with leading edge roughness compared to smooth measurement and a FFA measurement with NREL leading edge roughness at *Re* = 1.7×10^6 [4]. The Risø measurements were 1° average value bins obtained from measurements with a continuos change of the angle of attack at a rate of 0.1°/s to 0.5°/s.

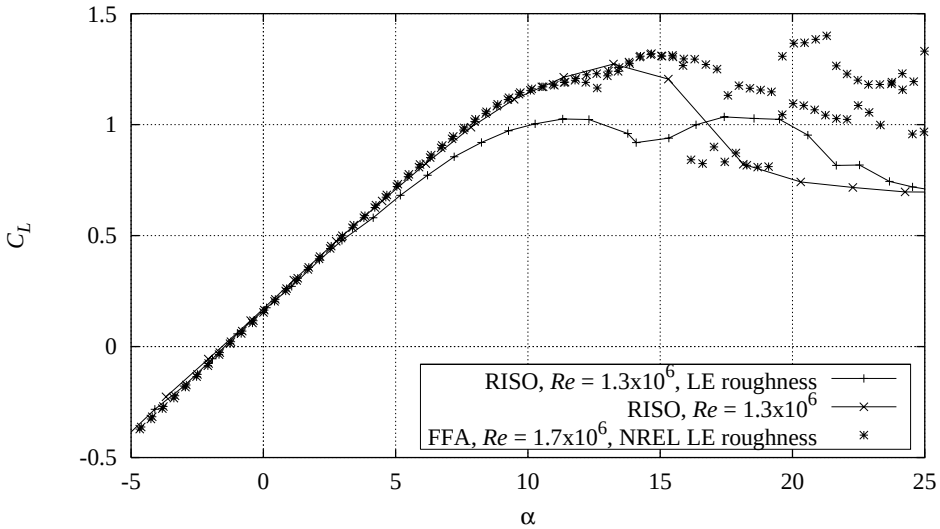

Figure 6-17 Measured C_L curve for smooth flow and with leading edge roughness, Re = 1.3×10^6, compared to FFA measurements with NREL roughness, Re = 1.7×10^6 [4] (NA63215CONT290296V1 and NA63215CONT221196V1).

The roughness applied in the Risø measurement appeared to affect the C_L curve more severely than the NREL roughness applied by FFA. At low angles of attack all measurements were in good agreement. Around 5°, the RISØ measurement showed trailing edge separation. This resulted in a lower C_{Lmax}

compared to the other measurements. In the post stall region there were large deviations.

The C_D curve with leading edge roughness corresponding to C_L in Figure 6-17 is shown in Figure 6-18. At low angles of attack below 0° there was good agreement between FFA and Risø LER measurements. C_D is higher for LER compared to smooth flow as expected. Before separation, C_D tended to increase for the Risø measurement compared to the FFA measurement, due to the more severe roughness. Separation occurred earlier for the Risø LER measurement compared the FFA measurement.

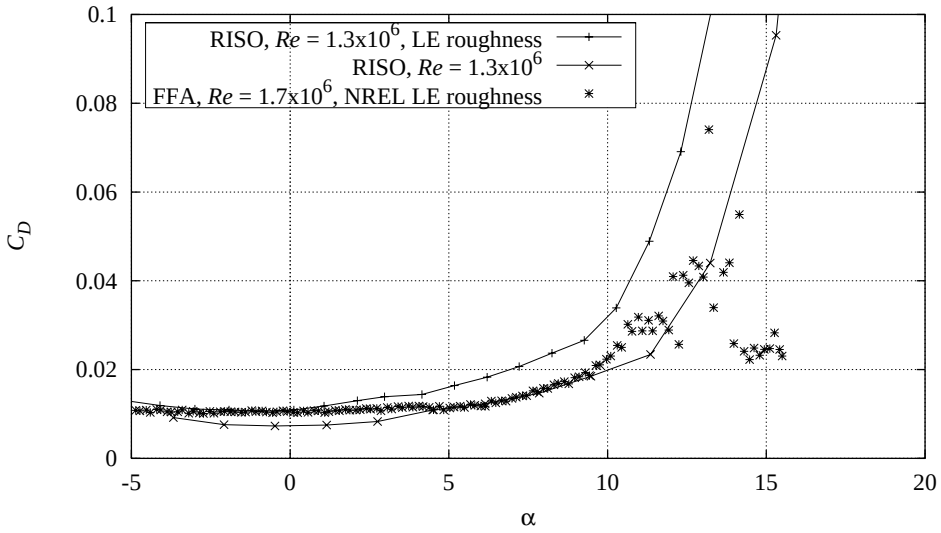

Figure 6-18 Measured C_D curve for smooth flow and with leading edge roughness, Re = 1.3×10^6, compared to FFA measurements with NREL roughness, Re = 1.7×10^6 [4] (NA63215CONT290296V1 and NA63215CONT221196V1).

Figure 6-19 shows the measured C_M curve for smooth and rough conditions corresponding to Figure 6-17. The leading edge roughness does not affect C_M at low angles of attack, whereas the drop in C_M at separation was shifted to a lower angle of attack due to the earlier separation of the flow. The difference between Risø measurements and FFA measurements corresponds to that of smooth flow.

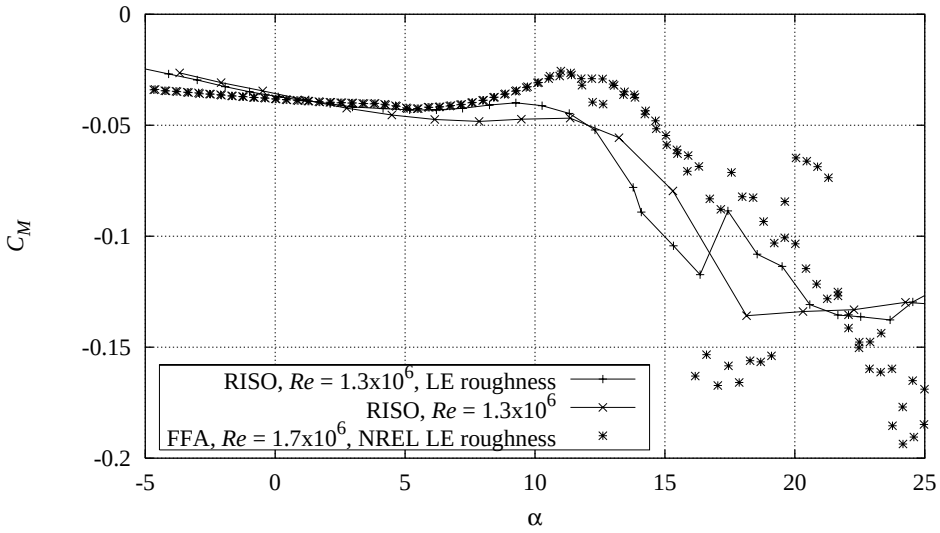

Figure 6-19 Measured C_M curve for smooth flow and with leading edge roughness, Re = 1.3×10^6, compared to FFA measurements with NREL roughness, Re = 1.7×10^6 [4] (NA63215CONT290296V1 and NA63215CONT221196V1).

6.4 Dynamic stall

The aerodynamic loads on the airfoil section were measured while the airfoil was in pitching motion. This comprises dynamic stall measurements, which are very important to the dynamics at high wind speeds for stall regulated wind turbines.

When the angle of attack is changed, the aerodynamic loading on the airfoil is altered and vortices are shed from the airfoil leading edge. Because of the interaction of the vortices with the flow and the travel time of these vortices along the airfoil surface and in the airfoil wake, there will be a time lag between changes in the angle of attack and changes in the aerodynamic loading. This time lag causes a hysteresis effect on the relation between the angle of attack and the aerodynamic loads and hysteresis loops appear for the aerodynamic forces. The size of the hysteresis loops varies with the type of airfoil flow, the amplitude of the pitching motion and the reduced frequency of the flow. When the airfoil suction side is partially or entirely separated, the loops become open compared to the loops at angles of attack with attached flow.

The pitching motion is related to the reduced frequency, *k*, which is defined as:

$$k = \frac{\omega c}{2V_\infty} \qquad (6\text{-}1)$$

Where $\omega = 2\pi f$ is the angular velocity of the pitching motion, f is the frequency, c is the airfoil chord and V_∞ is the free stream velocity.

Figure 6-20 shows a sample of a time series of the angle of attack with the airfoil in pitching motion at $k = 0.044$ corresponding to a frequency of 1.17 Hz. The amplitude was 2.5° with a mean angle of attack of 7.6°. Compared to a

pure harmonic motion there appeared to be some disturbances that come from spikes and electrical noise but also from vibrations of the test stand. The electric motor that runs the pitching mechanism had too low power resulting in difficulties in maintaining a smooth motion.

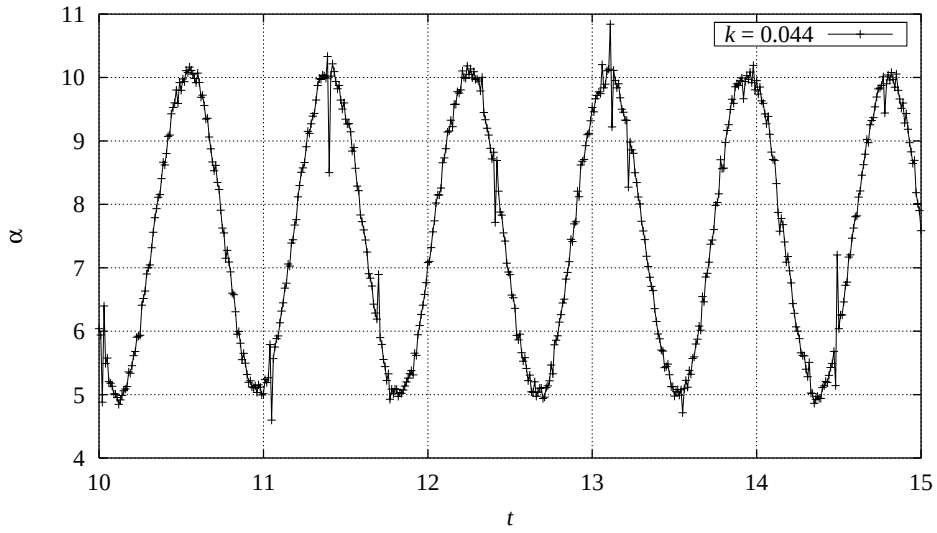

Figure 6-20 Raw data angle of attack time series (NA63215PITCH220296V1).

To improve the quality of the time series, we filtered the data by applying moving averages with a frame of 0.1s. The result is shown in Figure 6-21. This removed the spikes and made the curve smooth but it also reduced minimum and maximum values slightly.

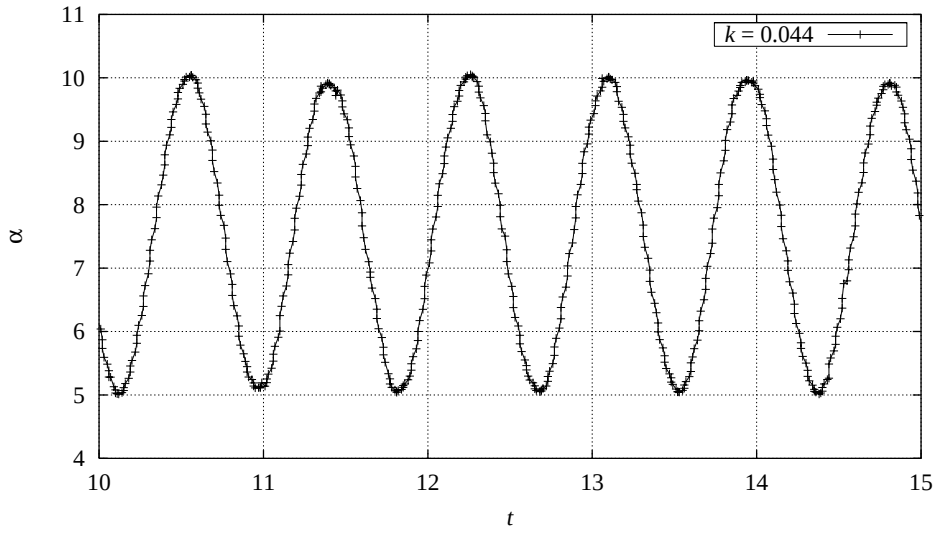

Figure 6-21 Angle of attack time series with 0.1s moving average (NA63215PITCH220296V1).

The PSD spectrums for both time series are shown in Figure 6-22. It can be seen that the dominating frequency was the pitching motion on 1.17 Hz, whereas no resonance appeared at higher frequencies. The moving average did not influence frequencies below 4 Hz, but did reduce noise at higher frequencies with more than one decade.

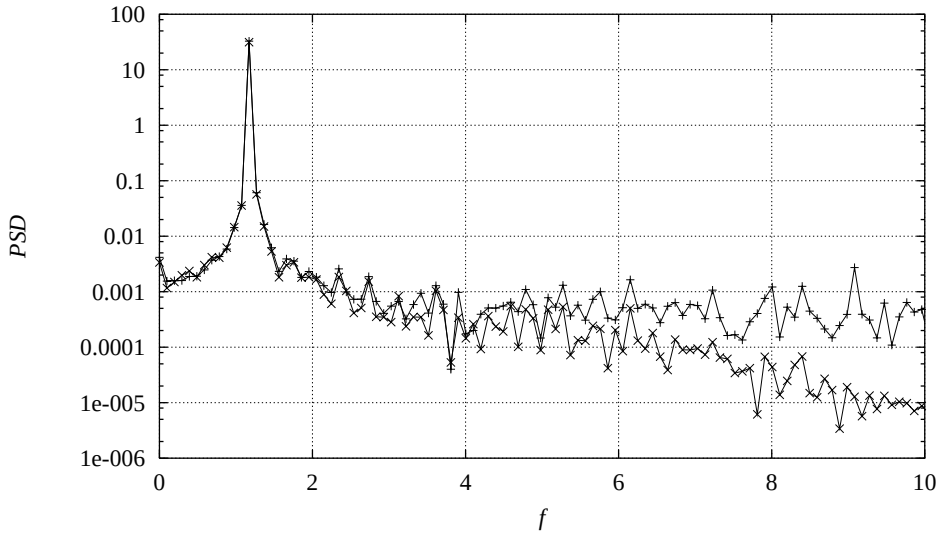

Figure 6-22 PSD of the angle of attack time series from Figure 6-20 and Figure 6-21 (NA63215PITCH220296V1).

Dynamic hysteresis loops

Figure 6-23 shows C_L versus angle of attack for the moving averaged time series shown in Figure 6-21. The tendency for the hysteresis loop was clearly seen, but the different loops were not identical because of small differences in the flow and measurement uncertainties.

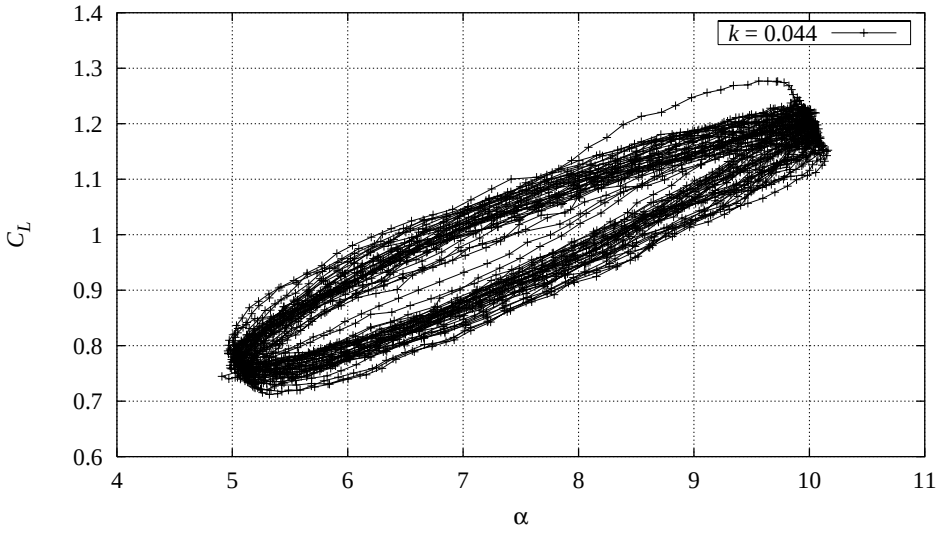

Figure 6-23 C_L hysteresis loops corresponding to the time series in Figure 6-21 (NA63215PITCH220296V1).

To obtain an averaged loop, the angles of attack were divided into 30 bins of a phase angle, which runs from 0 to 2π at each loop. This resulted in the average loop that can be seen in Figure 6-24. Both raw data and moving averaged data were sorted in bins and the comparison shows that the moving average does not change the loop except for minor differences in minimum and maximum angle of attack.

The direction of the hysteresis loops is important for the aerodynamic damping. The direction can be found by comparison of the change in the angle of attack with the phase angle. The direction in Figure 6-24 was counterclockwise.

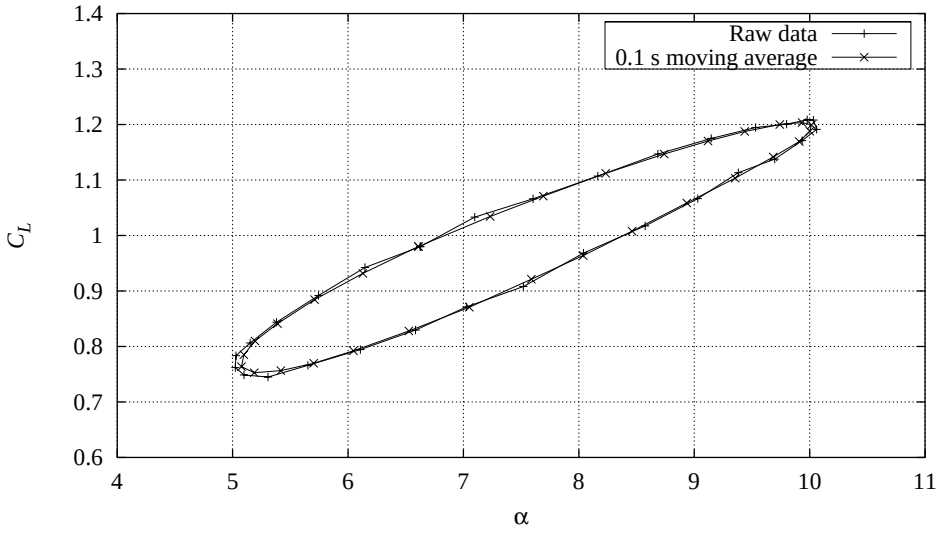

Figure 6-24 C_L hysteresis loop for raw data and moving averaged date sorted in 30 bins of a phase angle running from o to 2π at each pitching period (NA63215PITCH220296V1).

Reduced frequency *k* = 0.044

A series of seven different measurements was taken at k = 0.044, with amplitudes between 2.5° and 3.0° for different mean angles of attack covering both attached and separated flow.

The C_L, C_D and C_M hysteresis loops are shown in Figure 6-25, Figure 6-26 and Figure 6-27 respectively. C_D measurements were based on pressure drag only. Arrows indicate the directions of the loops. The steady curves are shown for comparison. For C_D and C_M there are small discrepancies between the level of the hysteresis loops and the steady mean curve caused by uncertainties from calibration of the measurement system.

The amplitude of the hysteresis loops varied between 2.5° and 3.0°. The raw data angle of attack amplitude was 3.0° but the wind tunnel boundary corrections, where α depend on C_L, caused a difference in amplitude.

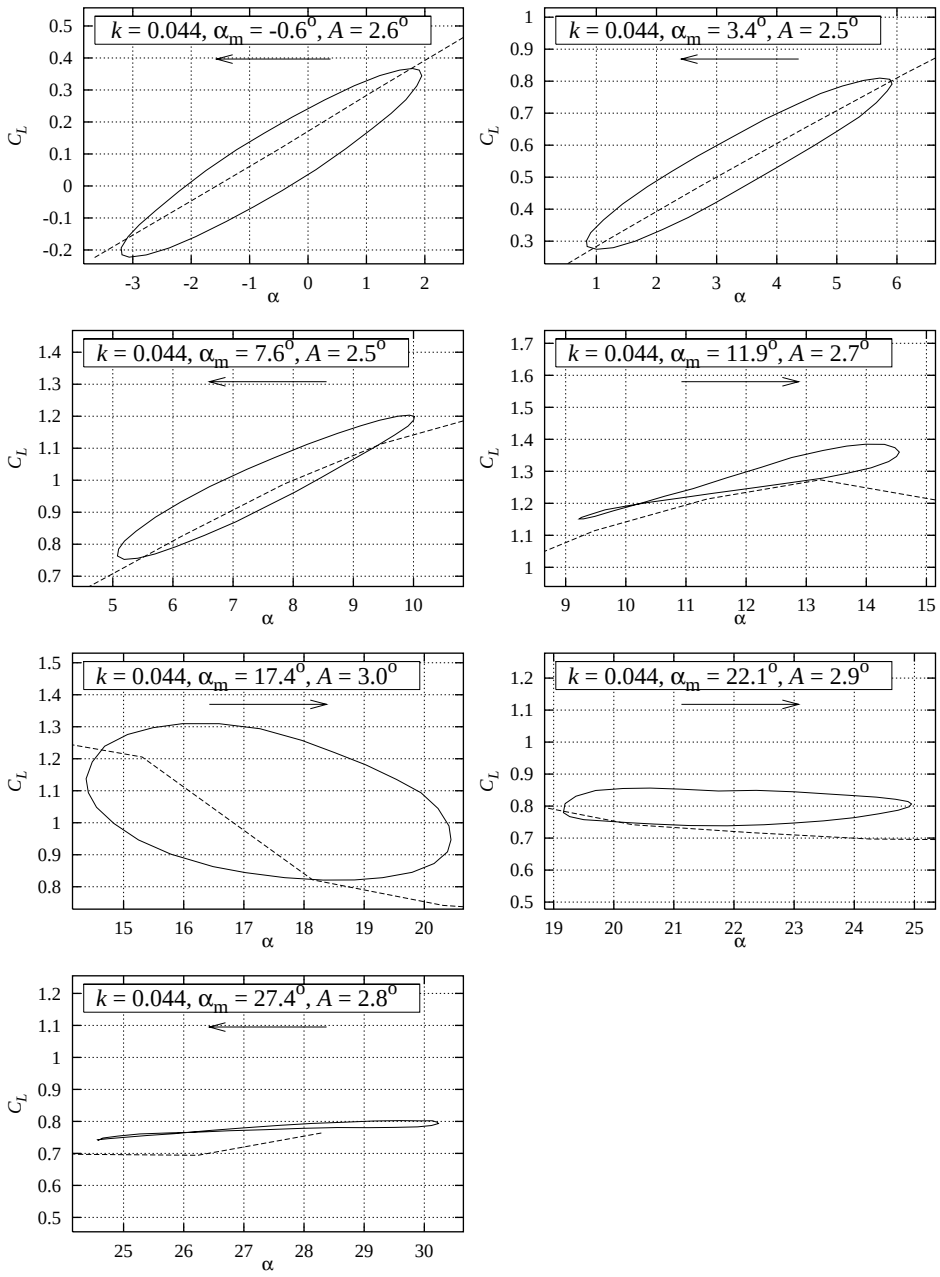

Figure 6-25 Measured C_L hysteresis loops for smooth flow at k = 0.044, A between 2.5° and 3.0°, Re = 1.3×10^6 (NA63215PITCH220296V1).

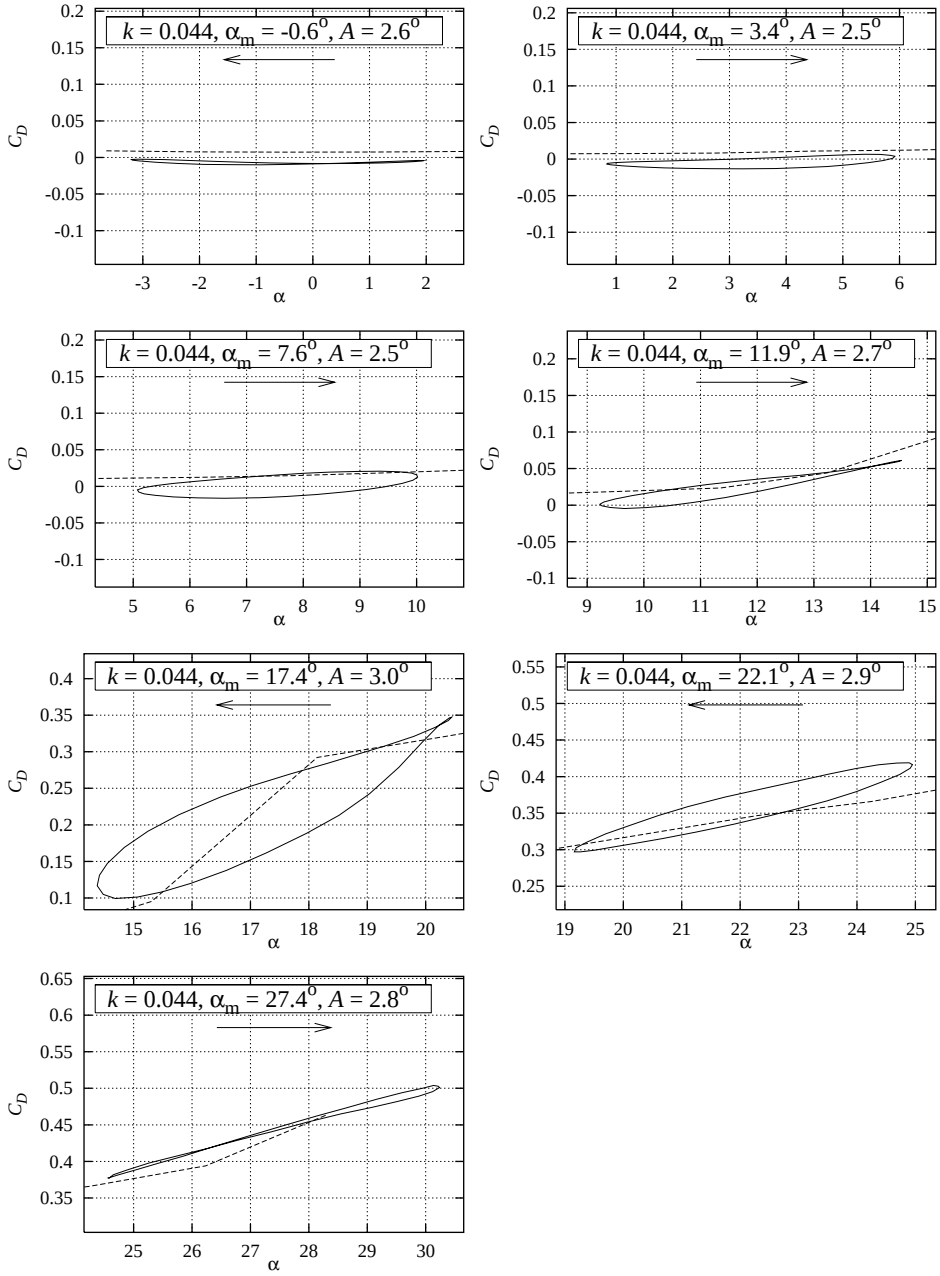

Figure 6-26 Measured C_D hysteresis loops for smooth flow at k = 0.044, A between 2.5° and 3.0°, Re = 1.3×10^6 (NA63215PITCH220296V1).

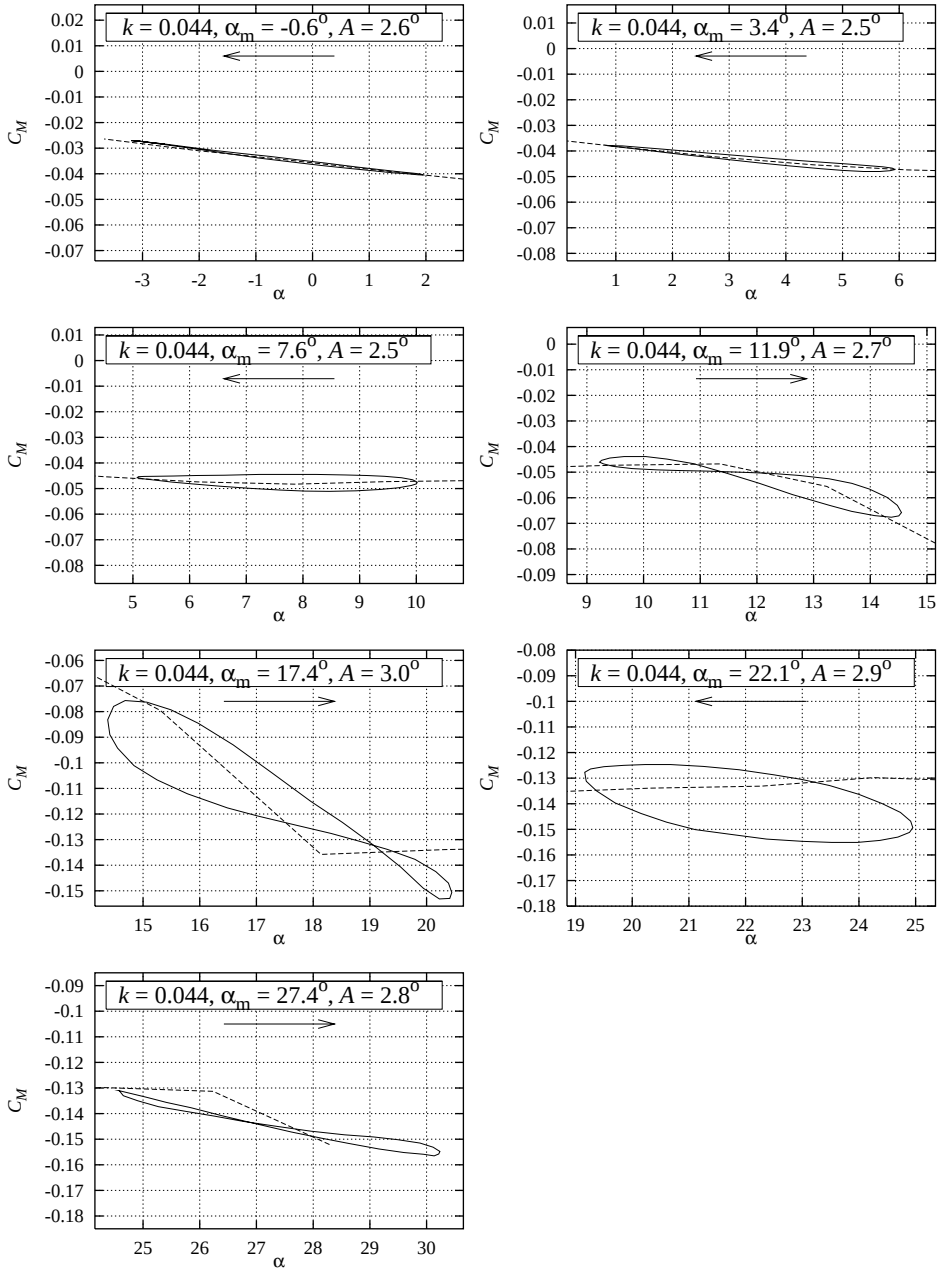

Figure 6-27 Measured C_M hysteresis loops for smooth flow at k = 0.044, A between 2.5° and 3.0°, Re = 1.3×10^6 (NA63215PITCH220296V1).

The C_L hysteresis loops are shown in Figure 6-28 together with the steady C_L curve. In general the slopes of the loops tended to follow the slope of the steady curve, except at stall where there were deviations.

The three loops at low angles of attack before C_{Lmax}, where the flow was attached, were counter clockwise. They were more narrow compared to the loops at stall. The loop around 12° was at the onset of trailing edge separation on the suction side of the airfoil. The direction of the loop changed from counter-clockwise to clockwise at 10°, where there was a crossover point. The beginning separation was seen to result in higher C_L than the average steady C_L. The loop around 17° in post stall was very open compared to the other loops. This was because of leading edge separation resulting in a large time lag and subsequently large deviations from the average C_L. The loop around 22° corresponded to deep stall condition with clockwise direction.

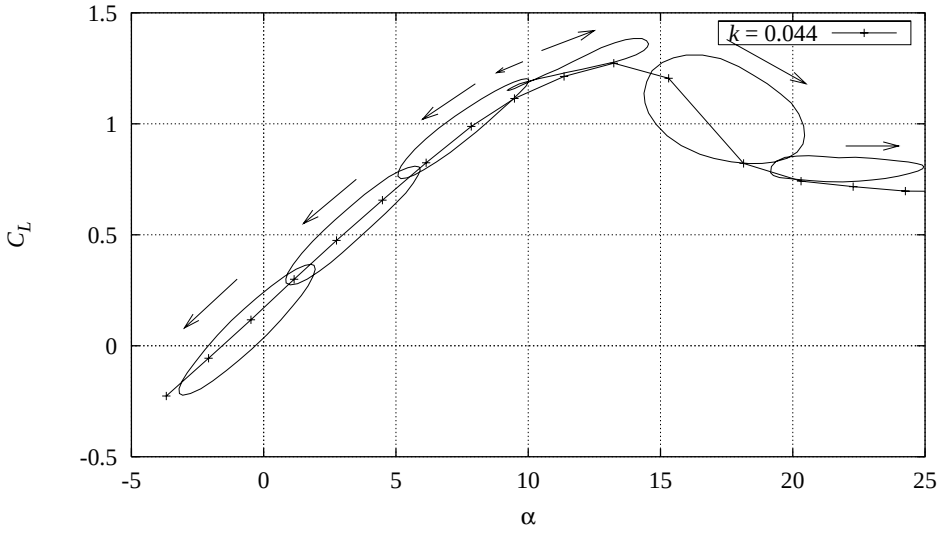

Figure 6-28 Measured C_L hysteresis loops at k=0.044 (NA63215PITCH220296V1).

Figure 6-29 shows C_D hysteresis loops based on pressure drag compared to the steady C_D curve from pressure drag. Since the wake rake measured the flow downstream of the airfoil there would be a time delay compared to the pressure measurements on the airfoil. Because of the unsteady loading, this delay made it impossible to use the wake rake.

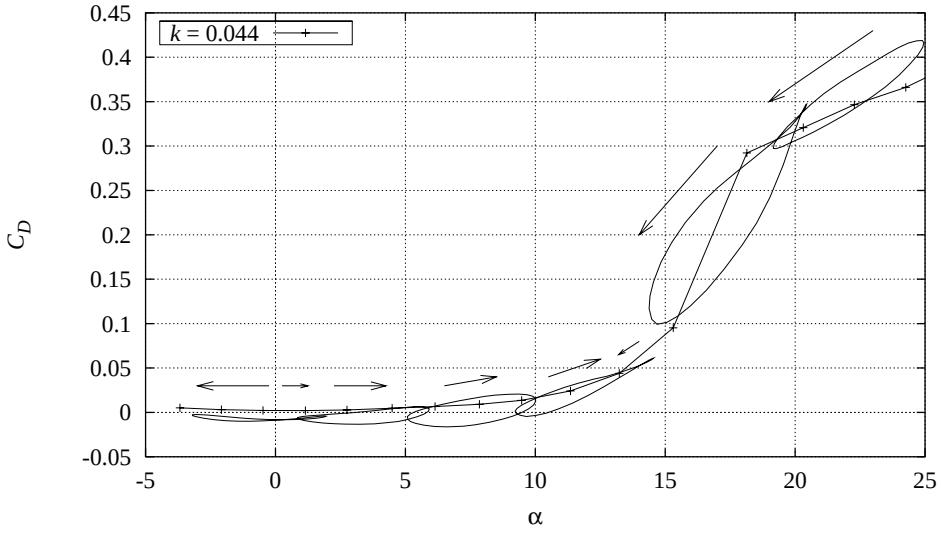

Figure 6-29 Measured C_D hysteresis loops at k=0.044 (NA63215PITCH220296V1).

There was a small deviation between mean C_D for the loops and the C_D mean curve caused by calibration uncertainties of the raw measurements. The tendencies from C_L regarding narrow and closed loops were also seen on C_D. However there were differences in the directions of the loops. The main part of the first loop was counterclockwise with a crossover point around 0°. Above 0°, the direction changed to clockwise. The next two loops were clockwise. The loop around 12^o was clockwise towards low angles of attack but counter-clockwise toward 15^o. The two loops in stall were both counter-clockwise.

The C_M hysteresis loops are shown in Figure 6-30. The loops were in general more closed and their slopes tended to follow the mean line curve well. At angles of attack below 12^o the directions were counterclockwise. The directions then changed to clockwise until 18^o, after which it again changes to counter-clockwise.

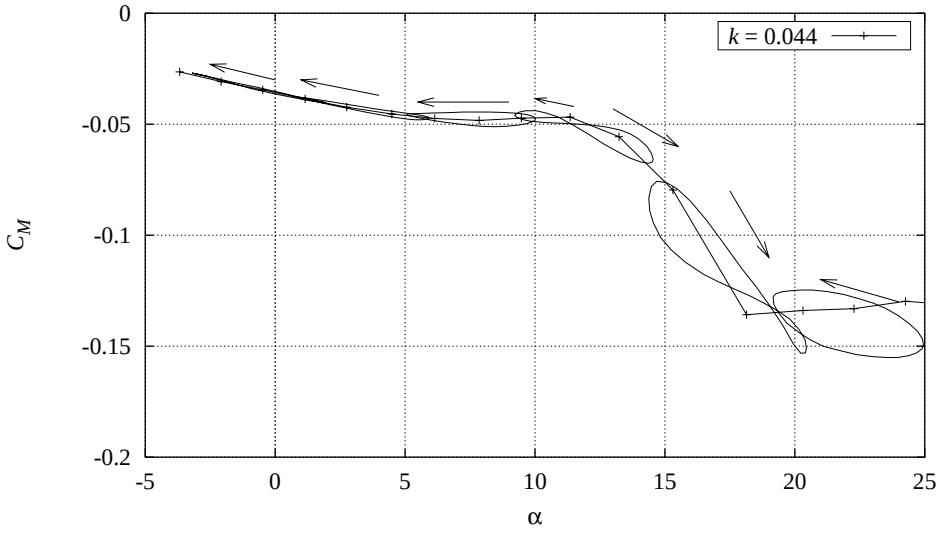

Figure 6-30 Measured C_M hysteresis loops at $A=6^o$, $k=0.044$ (NA63215PITCH220296V1).

Reduced frequency k = 0.022

A series of seven different measurements was taken at k = 0.022, with amplitudes between 2.5° and 3.3° for different mean angles of attack covering both attached and separated flow.

The individual C_L, C_D and C_M hysteresis loops are shown in Figure 6-31, Figure 6-32 and Figure 6-33. C_D measurements were based on pressure drag only. The mean value curves were shown for comparison.
Figure 6-34, Figure 6-35 and Figure 6-36 shows hysteresis loops for C_L, C_D and C_M respectively at k = 0.022.

The curves were in agreement with the curves for k = 0.044, however the loops were more narrow and the slopes of the loops at stall were reduced since the time lag between changes of the angle of attack and the airfoil loading was smaller.

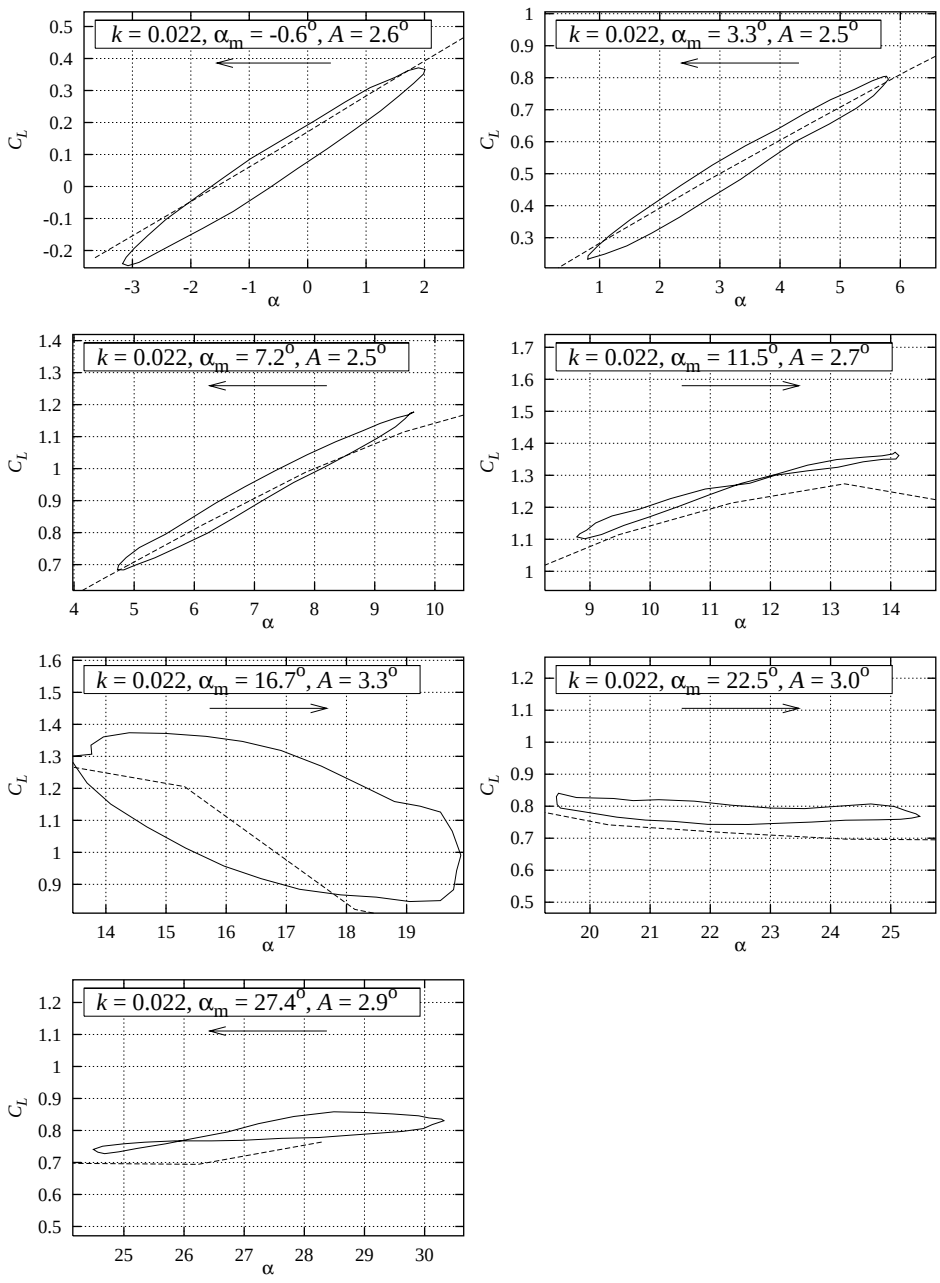

Figure 6-31 Measured C_L hysteresis loops for smooth flow at k = 0.022, A between 2.5° and 3.3°, Re = 1.3×10^6 (NA63215PITCH220296V2).

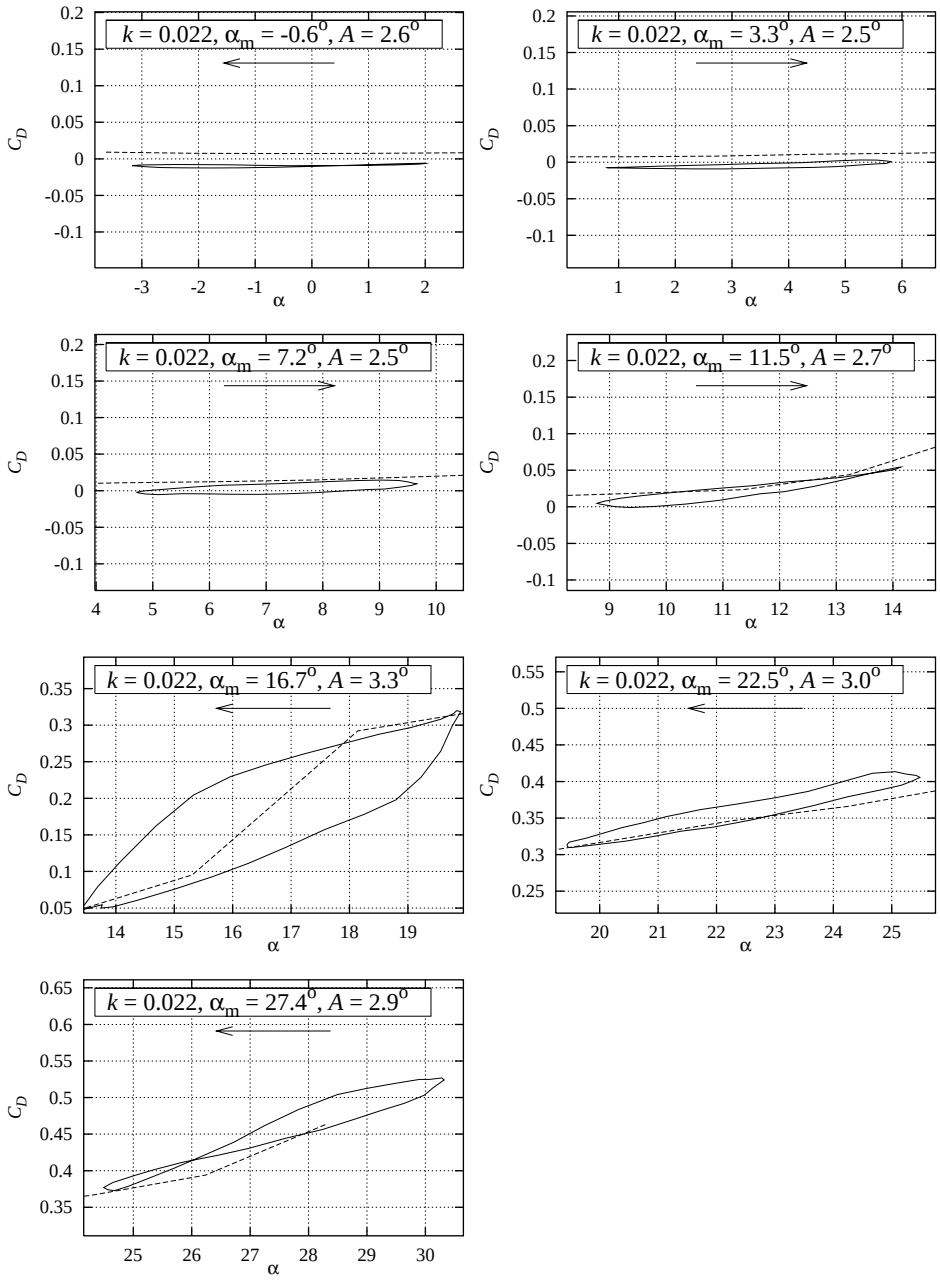

Figure 6-32 Measured C_D hysteresis loops for smooth flow at k = 0.022, A between 2.5° and 3.3°, Re = 1.3×10^6 (NA63215PITCH220296V2).

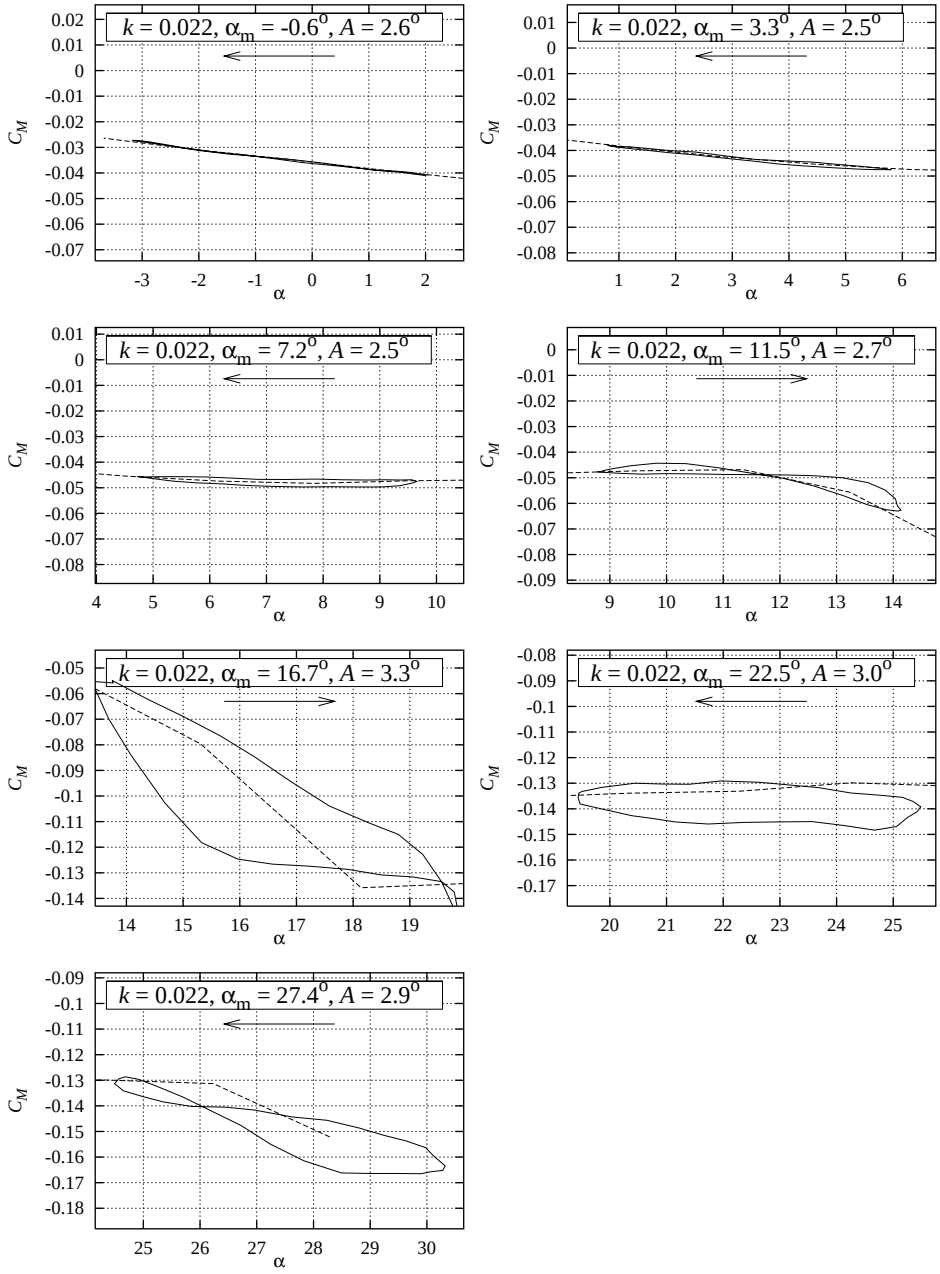

Figure 6-33 Measured C_M hysteresis loops for smooth flow at k = 0.022, A between 2.5° and 3.3°, Re = 1.3×10^6 (NA63215PITCH220296V2).

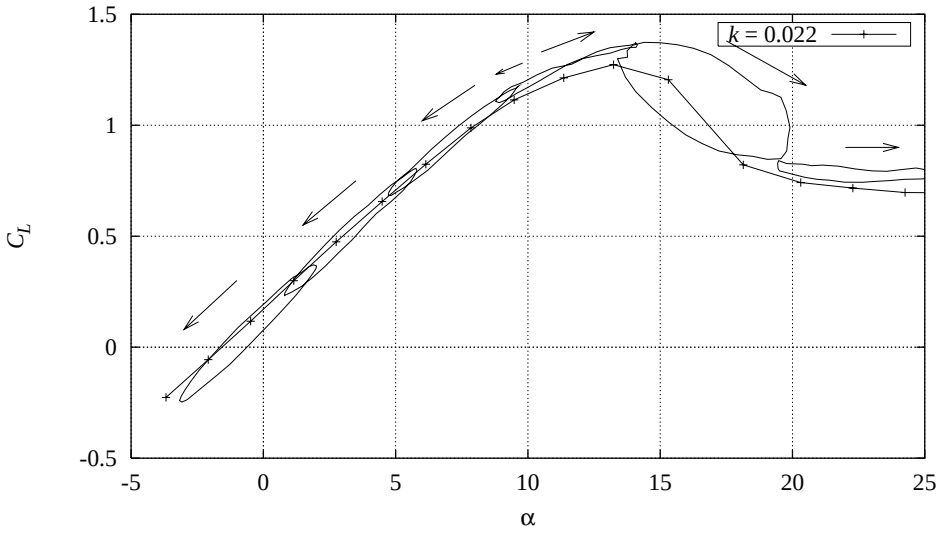

Figure 6-34 Measured C_L hysteresis loops at k=0.022 (NA63215PITCH220296V2).

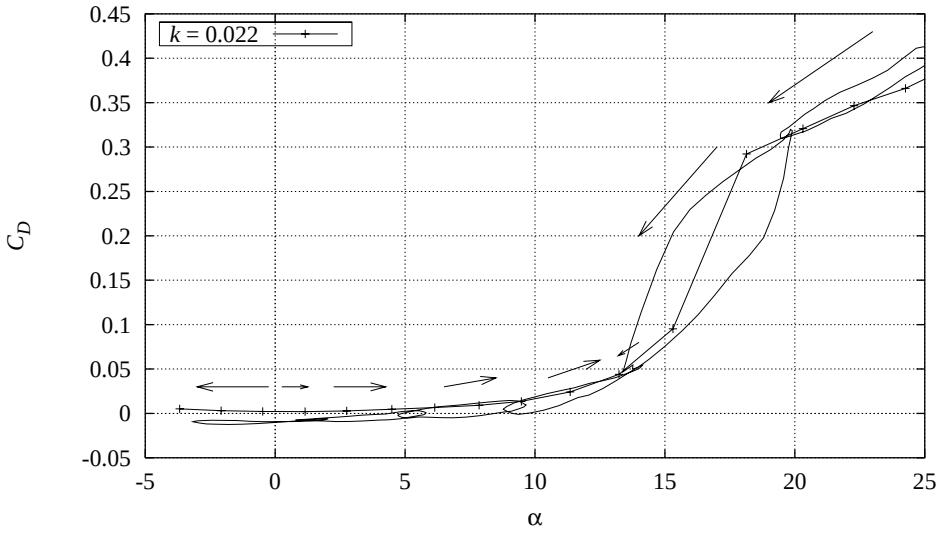

Figure 6-35 Measured C_D hysteresis loops at k = 0.022 (NA63215PITCH220296V2).

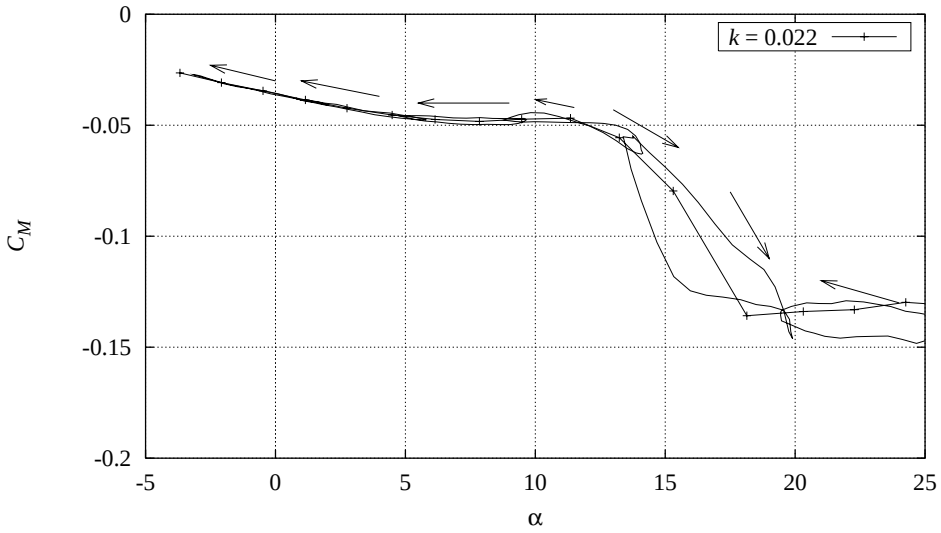

Figure 6-36 Measured C_M hysteresis loops at k = 0.022 (NA63215PITCH220296V2).

6.5 Double stall

This section contains investigations of time series during stall at high angles of attack. The aim is to determine the stability of the flow. In the references, [13] and [14] it is reported that the NACA 63-215 has different C_L levels at stall for identical inflow conditions. This is the so-called 'double stall' phenomenon [13]. The purpose with this section is to reveal the difference between the flow states at these levels and eventually identify the trigger for the different levels.

Measurements were performed at different angles of attack in stall. Initially, there were no signs of 'double stall'. Few measurements were taken where the clearance between the airfoil section and the endplates were sealed with tape, since this further improves the 2d behavior of the flow. One measurement then showed signs of 'double stall'. Figure 6-37 shows the time series of C_L for the NACA 63-215 airfoil at approximately $\alpha = 15.3^o$. This corresponds to an uncorrected α on 18.0^o. The sample frequency was 100 Hz, so 18000 frames correspond to 180 s. It can be seen, that initially the C_L was around 0.9 - 1.0 at the low lift level. At approximately 1250 frames, C_L suddenly increased to the high lift level at 1.2 - 1.3. For a long period, C_L remained at this high with level a few short stays on an intermediate level at 1.1 - 1.2. After around 12800 frames C_L suddenly changed to the intermediate lift level. In total 3 different stall levels appeared with clear difference in C_L.

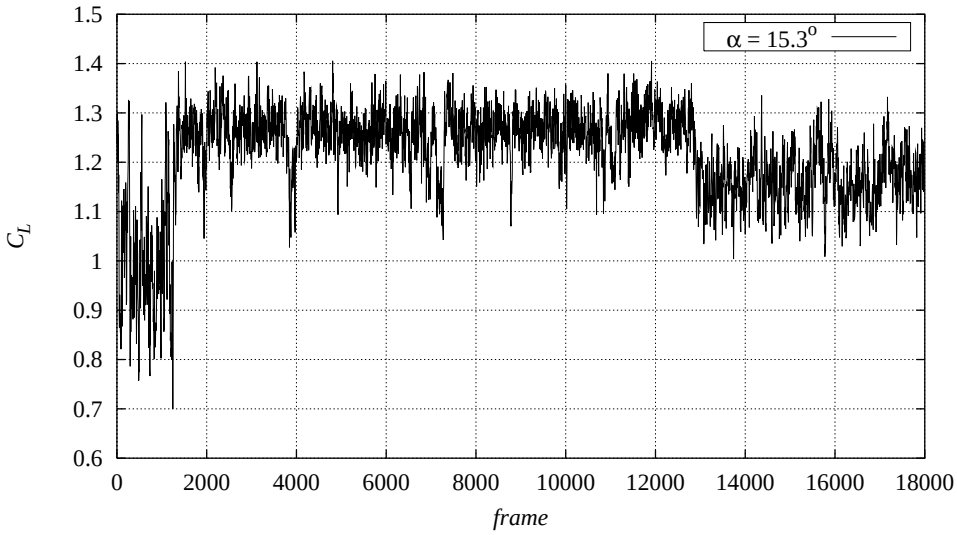

Figure 6-37 Measured C_L time series at α = 15.3° (18° uncorrected). 100 frames correspond to 1 second (NA63215STAT221196V1).

The corresponding C_D curve is shown in Figure 6-38. At the low lift level, C_D was around 0.2 - 0.25 with a high standard deviation. At the high lift level, C_D was reduced to 0.08 - 0.1 with much smaller standard deviation. Finally, C_D appeared to be at 0.1 at the intermediate lift level.

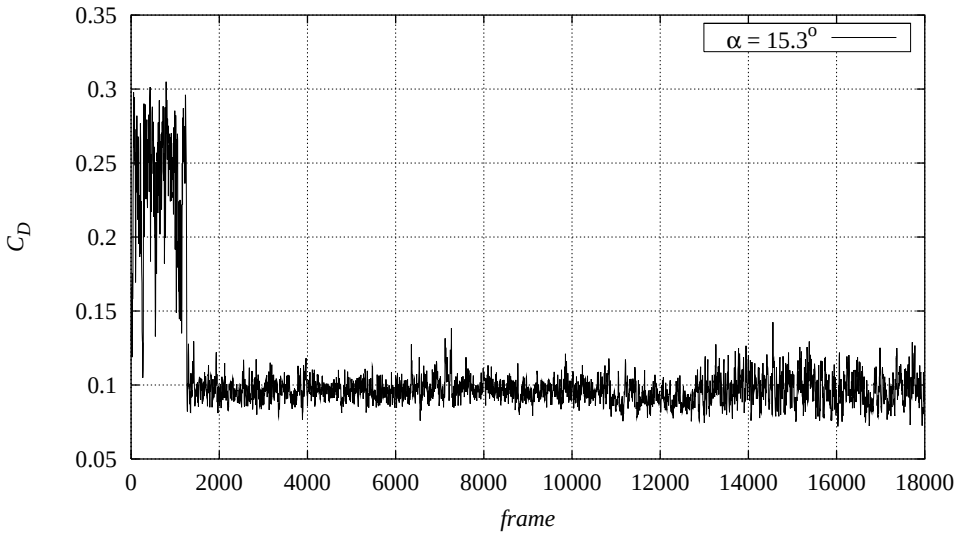

Figure 6-38 Measured C_D time series at α = 15.3° (18° uncorrected). 100 frames correspond to 1 second (NA63215STAT221196V1).

Figure 6-39 shows C_M for the same time series. At the low lift level, C_M was around -0.12 - 0.14. At the high lift level, C_M was increased to around -0.075. At the intermediate lift level, C_M was around -0.08 but with increased standard deviation compared to the high level.

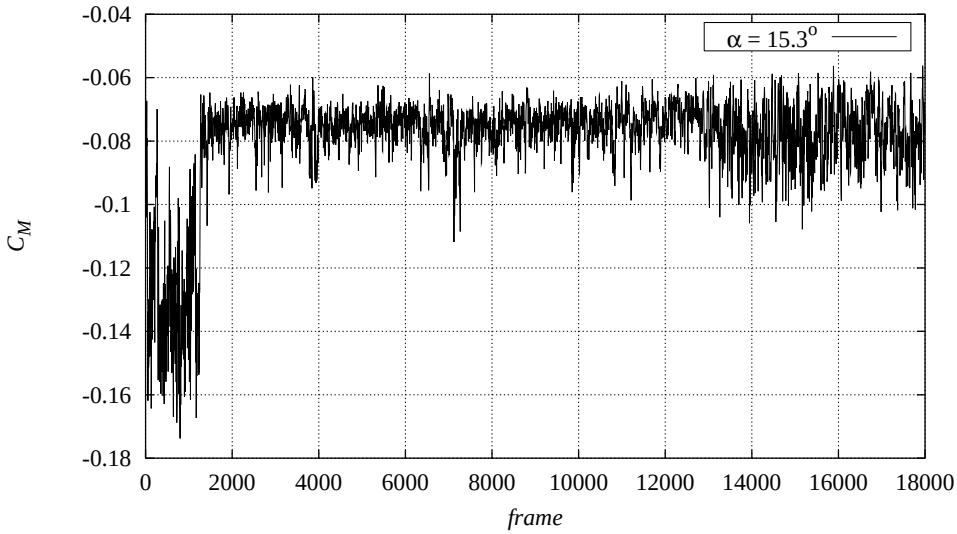

Figure 6-39 Measured C_M time series at α = 15.3° (18° uncorrected). 100 frames correspond to 1 second (NA63215STAT221196V1).

Figure 6-40 shows time averaged C_P curves for the different C_L levels. The low level had only a small suction peak, after which the flow was separated at 15 - 20% chord. The stagnation point was moved slightly toward the leading edge compared to the higher lift levels. The pressure difference on the trailing edge part of the airfoil was bigger compared to the other levels, however the lack of suction pressure resulted in reduced C_L.

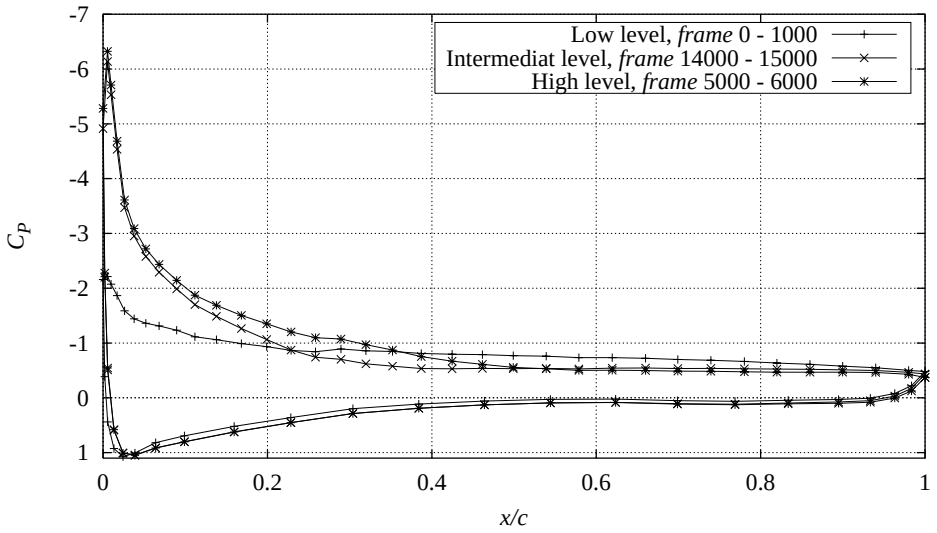

Figure 6-40 Measured C_P curves for the three different stall levels, time averaged from different parts of the time series from Figure 6-37 (NA63215STAT221196V1).

The other two lift levels had a pronounced suction peak and the separation point was located at 30 - 50% of the chord. The pressure side flow appeared to remain unaffected from these changes. The stagnation point was moved downstream compared to the low lift level. The degree of separation was lower in the cas of the high lift level. The circulation around the airfoil was in general increased. The suction side pressure was lower for the high level compared to the intermediate level and this resulted in the increased C_L for the high level.

A comparison of the three different lift levels shows that the low lift level seemed to be very different from the intermediate and the high lift levels. The latter appeared to have similarities. The low lift level had higher standard deviation compared to the other lift levels.

Three different areas of the time series in Figure 6-37 are further investigated in the following.

Area 1

This section covers the transition from the low lift level to the high lift level around frame 1250. Figure 6-41 shows a section of the C_L time series. C_L was increased from 0.7 to 1.28 in just 0.2 s.

The corresponding pressure distributions are shown in Figure 6-42. The time difference between each pressure distribution was 0.05 s. In the beginning, the flow was separated from the leading edge. The flow was then gradually building up a suction peak until the high level was reached and the flow was attached to approximately 40% chord. The pressure side coefficient was slightly decreased at the high lift level compared to the low lift level.

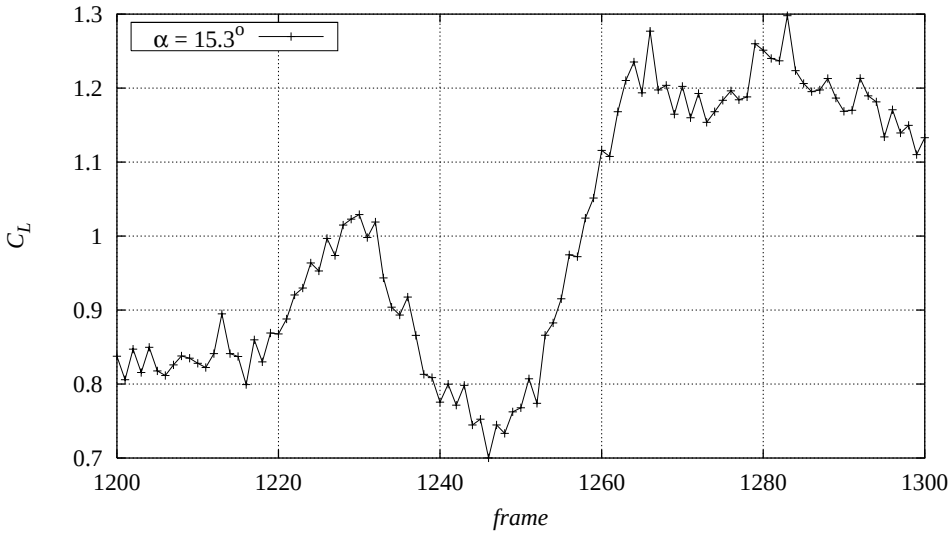

Figure 6-41 Part of the time series in Figure 6-37 that shows the change in C_L at the transition from level 1 to level 3 (NA63215STAT221196V1).

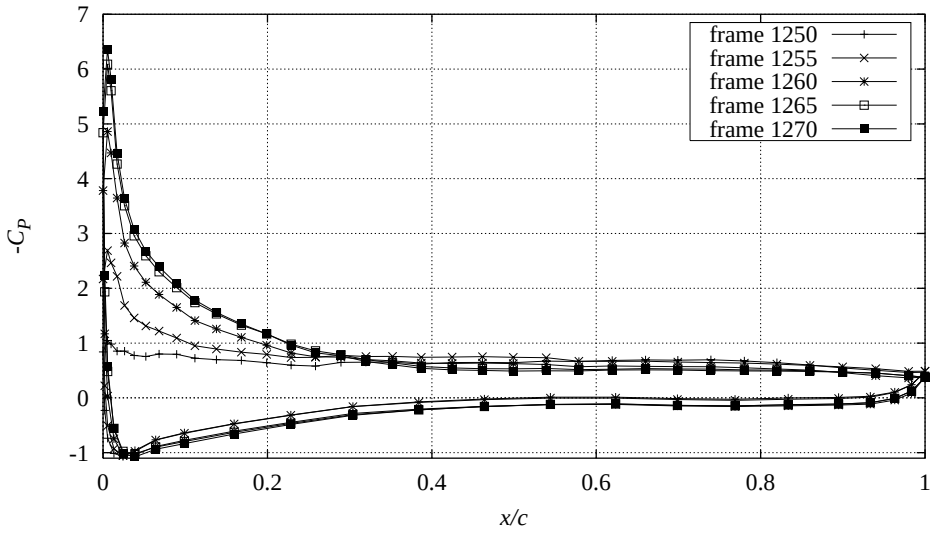

Figure 6-42 Selected C_P curves at transition from level 1 to level 3 (NA63215STAT221196V1).

Area 2

This section covers the transition from the high lift level to the intermediate lift level around frame 7120. Figure 6-43 shows a section of the C_L time series. C_L is seen to decrease from 1.33 to 1.07 in 0.18 s.

Figure 6-44 shows the corresponding pressure distribution. The time difference between each pressure distribution was 0.05 s. In the beginning, the flow was at the high lift level with a pronounced suction peak and attached flow to around 40%. The separation point was gradually moved towards the leading edge until 25% of the chord when the intermediate lift level was reached. The area contained in the suction peak was reduced and C_L was hereby reduced. However the minimum pressure was maintained. The pressure side was almost unchanged except for minor differences at the stagnation point and at the trailing edge.

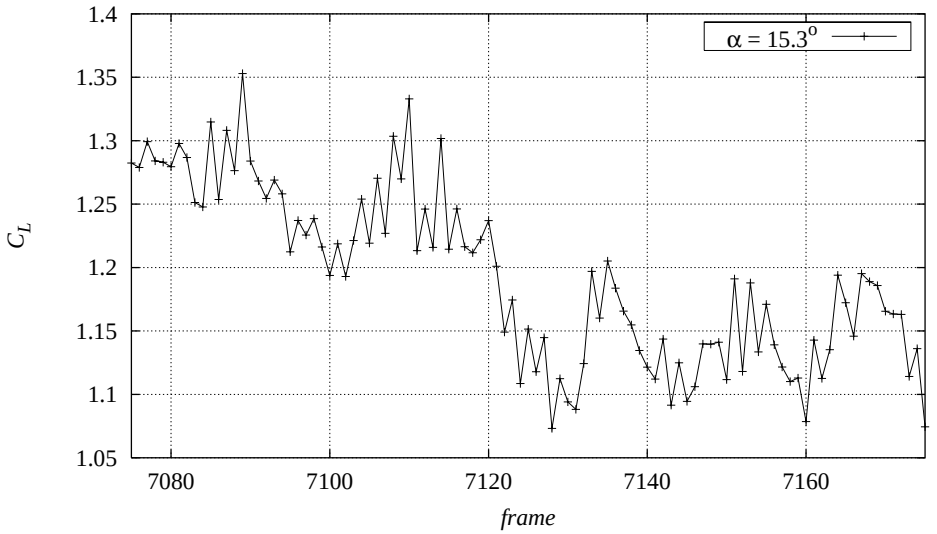

Figure 6-43 Part of time series in Figure 6-37 that shows the change in C_L at the transition from level 3 to level 2 (NA63215STAT221196V1).

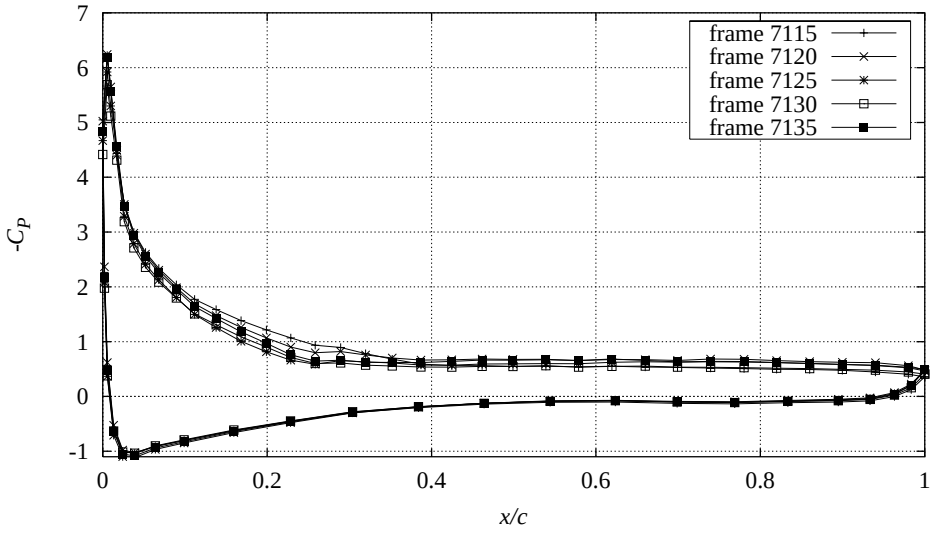

Figure 6-44 Selected C_P curves at transition from level 3 to level 2 (NA63215STAT221196V1).

Area 3

This section covers the transition from the intermediate lift level to the high lift level around frame 7280. Figure 6-45 shows a section of the C_L time series. C_L is seen to increase from 1.0 to 1.37 in 0.35 s.

Figure 6-46 shows the corresponding pressure distribution. The time difference between each pressure distribution was 0.05 s. In the beginning, the flow was at the intermediate lift level with a high suction peak and with separation at 25%. The separation point was then gradually moved towards the trailing edge until 50% chord where the maximum lift level was reached. The area below the suction peak was increased and C_L was increased. The pressure side remained unchanged.

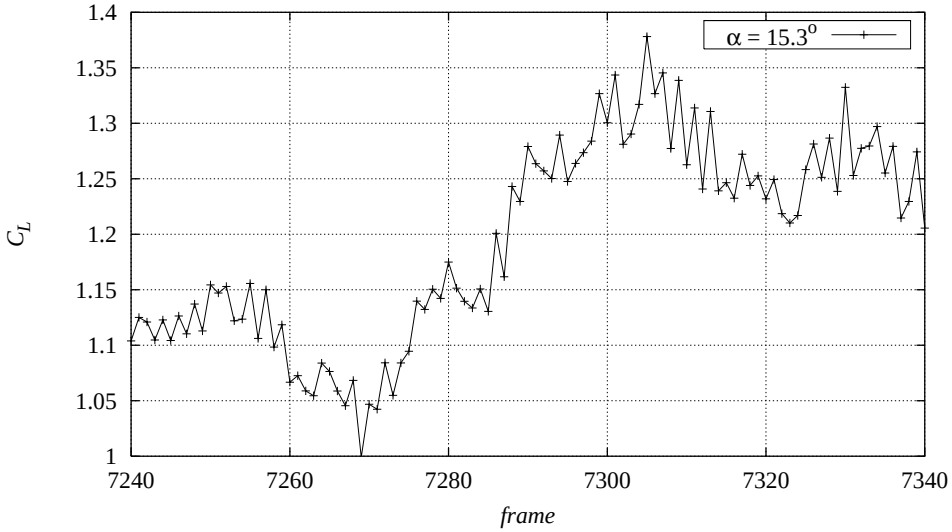

Figure 6-45 Part of time series in Figure 6-37 that shows the change in C_L at the transition from level 2 to level 3 (NA63215STAT221196V1).

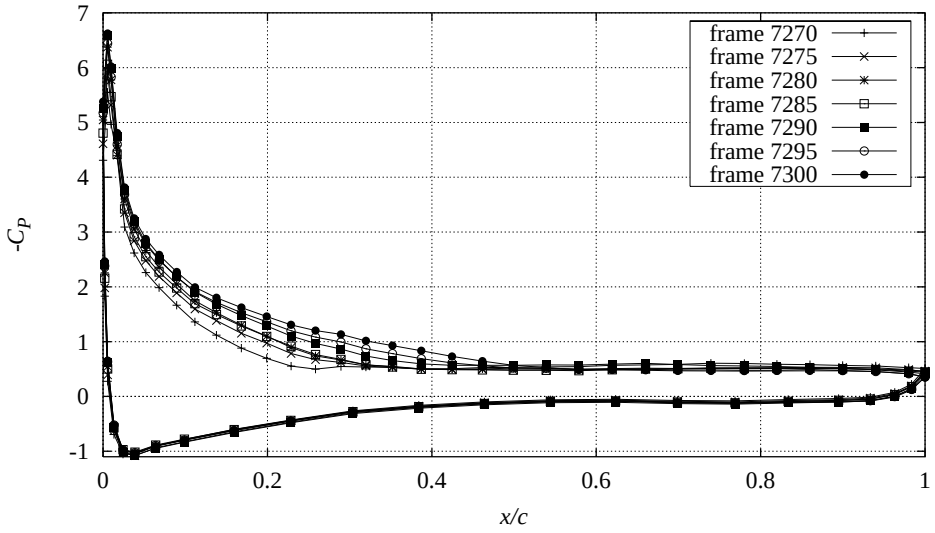

Figure 6-46 Selected C_P curves at transition from level 2 to level 3 (NA63215STAT221196V1).

7 Conclusions

This report concerns development and validation of a 2d testing facility for flows around 2d airfoil sections. The VELUX wind tunnel of the closed return type with an open jet test section was used. A test stand was developed to make possible these measurements. The stand was designed for airfoil sections with a chord length up to 0.6 m and a span of 1.9 m, mounted between endplates. Reynolds Numbers until 1.5 million could be achieved for a maximum inlet flow velocity of 40 m/s. Stationary inflow as well as dynamic inflow measurements were possible with the airfoil in pitching motion.

The HyScan 2000 pressure measurement system was used to measure the pressure distribution around the airfoil section and to measure the variation of static and total pressure in the airfoil wake with a wake rake. Upstream Pitot tubes were used to determine reference values for free stream static and total pressure.

A literature study of this type of wind tunnel flow resulted in application of wind tunnel corrections for streamline curvature and down-wash. It was however complicated to find proper corrections because of the presence of the floor close to the jet and because of the limited size of the endplates. The corrections could not be combined since such a theory was not found in the literature and we chose only to apply the streamline curvature correction since this is most important.

Measurements of the flow quality showed a non-uniform velocity profile at the inlet. The flow was accelerated in the center of the jet between the inlet and the test stand so that the velocity profile was nearly uniform at the test stand. The speed-up was 6.9%. There was a pressure loss on approximately 15 Pa/m. The turbulence intensity at the inlet was 1%, which is rather high, compared to low turbulent wind tunnels but low compared to natural conditions. The overall quality of the wind tunnel flow was found acceptable and corrections for speed-up and pressure loss were established.

The NACA 63-215 airfoil was measured. The results were compared to measurements from FFA, Sweden, on exactly the same airfoil section, to NACA measurements and to numerical predictions from XFOIL and EllipSys2D. The agreement was good. The maximum lift coefficient was captured well and the lift coefficient curve slope was nearly as steep as the FFA measurement. Minimum drag was slightly too high but the shape of the drag coefficient curve and the rise to high drag at separation were captured well. The maximum lift coefficient was determined to 1.3.

Measurements of dynamic inflow with the airfoil in pitching motion were used to find hysteresis loops of the aerodynamic coefficients. The reduced frequencies, 0.022 and 0.044, were measured at different mean angles of attack with amplitudes between 2.5° and 3.3°. The directions and the slopes of the obtained loops agreed well with theory.

Measurements with steady inflow at high angles of attack were used to investigate the ‘double stall’ phenomenon. Long duration time series were measured at high angles of attack where the inflow remained unchanged. Three distinct levels could be determined for the lift coefficient with corresponding differences in drag and moment coefficients. The pressure distributions were compared for the different levels and the flow was found to be very different with different points of separation. Samples of time series were used to show the change in lift coefficient when the flow shifted between the different levels.

This report documents the development of the testing method involving:

- An evaluation of the flow quality in the wind tunnel.
- Establishment of wind tunnel boundary corrections.
- Measurements of the NACA 63-215 airfoil with comparison to measurements by FFA on exactly the same airfoil section and comparisons to numerical predictions.
- Measurements of hysteresis loops from dynamic inflow.
- Measurements of double stall.

References

[1] Abbot, I.H. and von Doenhoff, A. E., 1959, Theory of wing sections, Including a summary of airfoil data, Dover Publications Inc., N.Y.

[2] Somers, D.M. and Tangler, J.L., 1995, Wind-Tunnel Test Of The S814 Thick Root Airfoil, *Proc. ASME Wind Energy 95*, Houston, Texas, USA.

[3] Timmer, W.A. and van Rooy, R.P.J.O.M, 1993, Wind Tunnel Results for a 25% Thick Wind Turbine Blade Airfoil, *Proc. EUWEC 93*, Lübeck-Travemünde, Germany, 1993.

[4] Björk, A., 1996, A Guide to Data Files From Wind Tunnel Test Of A NACA 63-215 Airfoil at FFA, Report FFAP-V-018, 1996.

[5] Björk, A., 1996, 2-D Wind Tunnel test of 15% and 18% LM2 Airfoils and the 21% FFA-W3-211 Airfoil. Report FFAP-A-1017, 1996

[6] Hoadley, D., Madsen, H.A. and Bouras, B., 1993, Aerofoil Section Design and Assessment, Final Rep. Contract JOUR 0079, The Commission of the European Communities, DGXII, 1993.

[7] Rae Jr., W.H., Pope, A., 1984, Low-Speed Wind Tunnel Testing, SE, John Wiley & Sons, ISBN 0-471-87402-7.

[8] Garner, H.C., Rogers, E.W.E., Acum, W.E.A. and Maskell, E.C., 1966, Subsonic Wind Tunnel Wall Corrections, NATO, AGARD.

[9] Brooks, T.F. and Marcolini, M.A., 1984, Airfoil Trailing Edge Flow Measurements and Comparison with Theory Incorporating Open Wind Tunnel Corrections, AIAA-84-2266, AIAA/NASA 9th Aeroacoustic Conference.

[10] Unpublished measurements of the VELUX Wind Tunnel Flow.

[11] Madsen, H.A., 1993, Measurement and Calculation of the velocity field in the 4x4 m Novelco Wind Tunnel, (In Danish), Note, Risø National Laboratory, Denmark.

[12] Sørensen, N.N., General Purpose Flow Solver Applied to Flow over Hills, Risø-R-827(EN), Risø National Laboratory, June 1995.

[13] Madsen, H.A., Bak, C., Fuglsang, P. and Rasmussen, F., The Phenomenon of Double Stall. *Proc. EWEC'97*, Dublin, Ireland, 1997.

[14] Antoniou, I., Madsen, H.A. and Rasmussen, F., 1995, Wind Tunnel Measurements on a LM 8.2 m Blade, Risø-I-800(EN), Risø National Laboratory, Denmark.

[15] Mangler, W, 1938, The Lift Distribution of Wings with End Plates, NACA NACA Technical Memorandum No. 856, Washington, April 1938.

[16] Madsen, H.A., Filippone, A, 1995, Implementation and Test of the XFOIL Code for Airfoil Analysis and Design, Risø-R-644(EN), Risø National Laboratory, Denmark.

A1 Measurement survey

This appendix describes the performed measurements in detail to support the understanding of the discussed measurements in the report and for use in subsequent exploitation. First the different measurement types are described and the naming convention for the data files is explained. The format of the data files is given. Finally, each performed measurement is listed and described.

A1.1 Measurement types

There are four different basic types of measurements of the airfoil flow as shown in Table A1-1.

Table A1-1 Overview of the different types of measurements that have been performed.

Name	**Short description**	**Purpose**
STEP	• Discrete measurements at different angles of attack. • Angle of attack range: -6° to 30°. • Interval between different angles: 1° to 4°. • Time series length: 20 s. • Sampling frequency: 5 Hz.	The lift, drag and moment polar versus angle of attack.
CONT	• Continuos measurements at different angles of attack. • Angle of attack range: -6° to 30°. • Rate of change of angle of attack: 0.1°/s to 0.5°/s (manually changed). • Time series length app: 250 s. • Sampling frequency: 50 Hz.	The lift, drag and moment polar versus angle of attack. (shorter measurement time compared to 'STEP')
STAT	• Stationary measurements at different angles of attack. • Time series length: 20s to 180s. • Sampling frequency: 100 Hz.	Time series of airfoil flow at different angles of attack, usually in stall.
PITCH	• Dynamic measurements at different mean angles of attack with the airfoil in pitching motion. • Pitching amplitude: 3° to 6° • Reduced frequency: to 0.12 • Time series length: 30s to 40s. • Sampling frequency: 100 Hz.	Time series of unsteady airfoil flow from pitching motion for determination of hysteresis loops for lift, drag and moment at different pitching frequencies and amplitudes.

Table A1-2 shows the different parameters that determine the sampling frequency, *f*, and the time series length, *T*.

The sampling frequency, *f*, is obtained from:

$$f = T_f \cdot n_{av} \qquad \textit{(A1-1)}$$

The length of the time series, *T*, is obtained from:

$$T = T_f \cdot n_{av} \cdot n_f \qquad \textit{(A1-2)}$$

Table A1-2 Explanation of parameters that determine sample frequency and time series length.

Parameter	**Symbol**	**Description**
Frames per file	n_f	The number of frames that are written to file for each measurement.
Time between scan of pressure channels	T_s	The time between scan of each of the pressure transducers.
Time between frames	T_f	The time between scan of frames.
Number of frame averages	n_{av}	The number of frames that are used to average before the average frame is written to file.

A1.2 Data file naming convention

The different data files are named by:

- The name of the airfoil.
- The measurement type keyword from Table A1-1.
- The date of measurement, data, DD, month, MM, year, YY, 'DDMMYY'.
- A version number, VNN, where NN is the version number.
- The filename extension. For time averaged data, '.DAT', and for time series, 'NNN', where NNN is the time series number.

An example is shown in Table A1-3.

Table A1-3 Example of naming convention of data files

NA63215	STEP	290296	V1	.DAT

A1.3 Data file format

The format of the data files is described in Table A1-4. Each measurement frame/average is written subsequently in rows.

Table A1-4 The content of the columns in the data files.

Col.	Symbol	Sensor	Unit	Description
1	α_c	aoac	°	Corrected angle of attack
2	C_L	cl	-	Lift coefficient (pressure)
3	C_{Dc}	cdc	-	Corrected drag coefficient (wake rake + pressure)
4	C_{Mc}	cmc	-	Corrected moment coefficient (pressure)
5	C_{Dpc}	cdpc	-	Corrected drag coefficient (pressure)
6	C_{Dw}	cdw		Drag coefficient (wake rake)
7	α	aoa	°	Raw angle of attack
8	C_D	cd	-	Raw drag coefficient (wake rake + pressure)
9	C_{Dp}	cdp		Raw drag coefficient (pressure)
10	C_M	cm	-	Raw moment coefficient (pressure)
11	Re	re		Free stream Reynolds Number
12	q_{ref}	qref	Pa	Free stream dynamic pressure
13	$p_{stat,ref}$	ps,ref	Pa	Free stream static pressure
14	T	t	°	Tunnel temperature
15	p_{atm}	patm	mBar	Atmospheric pressure
16-71	C_P	cp(x)		Pressure coefficients corresponding to the coordinates in top row
72-74	$p_{stat,Pitot}$	ps,Pitot()	Pa	Pitot tube static pressures
75-77	$p_{tot,Pitot}$	pt,Pitot()	Pa	Pitot tube total pressures
78-82	$p_{stat,wake}$	ps,wake	Pa	Wake rake static pressures corresponding to the coordinates in top row
83-136	$p_{tot,wake}$	pt,wake	Pa	Wake rake total pressures corresponding to the coordinates in top row

A1.4 Performed measurements

Table A1-5 contains a list of the performed measurements.

Table A1-5 Performed measurements

Data file	Description and remarks
NA63215STEP290296V1.DAT	20s average values at 37 angles between -6° and 30°
NA63215STEP290296V1.000-036	20s time series at 5 Hz for each angle of attack
NA63215STEP221196V1.DAT	20s average values at 18 angles between -6° and 30°
NA63215STEP221196V1.000-017	20s time series at 5 Hz for each angle of attack
NA63215CONT290296V1.DAT	Time series at 50 Hz with continuos change of angle of attack between -6° and 30° (manually changed)
NA63215CONT221196V1.DAT	Time series at 50 Hz with continuos change of angle of attack between -6° and 30° (manually changed) • Sand paper at the leading edge to simulate leading edge roughness
NA63215STAT290296V1.000-035	20s time series at 5 Hz for each angle of attack
NA63215STAT221196V1.000,001,003,005	180s time series at 100 Hz for each angle of attack • The angles of attack were in stall • The clearance between the airfoil span and the endplates was sealed with tape to further enhance 2d flow
NA63215STAT221196V2.006	180s time series at 100 Hz for each angle of attack • The angles of attack were in stall • The clearance between the airfoil span and the endplates was sealed with tape to further enhance 2d flow • Sand paper at the leading edge to simulate leading edge roughness

Data file	Description and remarks
NA63215PITCH290296V1.000-006	30 s time series at 100 Hz for each mean angle of attack • Amplitude between 5° to 6° • Reduced frequency, k = 0.044
NA63215PITCH290296V2.007-013	40 s time series at 100 Hz for each mean angle of attack • Amplitude between 5° to 6° • Reduced frequency, k = 0.022